Characterization of the Mechanical and Microstructural Properties of Thin Non-Orientated Electrical Steel Sheets

by

Tamuno-Ibim Tolofari

A thesis

presented to the University of Waterloo

in fulfilment of the

thesis requirement for the degree of

Master of Applied Science

in

Mechanical and Mechatronics Engineering

Waterloo, Ontario, Canada, 2023

Author's Declaration

This thesis consists of material all of which I authored or co-authored: see Statement of Contributions included in the thesis. This is a true copy of the thesis, including any required final revisions, as accepted by my examiners.

I understand that my thesis may be made electronically available to the public.

Statement of Contributions

Tamuno-Ibim Tolofari is the sole author of this thesis written under the supervision of Dr. Hamid Jahed Motlagh. Furthermore, the results presented in chapters 4 to 9 of this thesis have also been used in journal papers of which the candidate is a primary or secondary author. The other individuals involved and their associated contributions to the current research are detailed below.

Dr. Seyed Behzad Behravesh provided training and supervision on the experimental work involving the tensile and fatigue testing of specimens.

Dr. Dulal Saha provided training and supervision on sample preparation, optical microscopy, scanning electron microscopy and identifying the fracture mechanisms. He also conducted the work involving the microstructural and SEM fractography analysis presented in Chapters 4 to 8.

Abstract

With the rise and growth of electric vehicles, enhancing the design and implementation of electric engines in transportation vehicles is essential. Electric motors are an essential part of this enhancement. The material from which the stator and rotor cores of electric motors are made out of are required to be highly permeable with low magnetic losses and magnetostriction. Non-Oriented Electrical steel is a cost-effective choice of material that meets these requirements. In this thesis, three grades of non-oriented electrical steel sheets namely: 27PNX1350F, 25SW1250 and 20SW1200 with sheet thicknesses of 0.27mm, 0.25mm and 0.20mm respectively were categorized mechanically and microstructurally at room and an elevated temperature of 150°C.

The initial microstructure of the non-oriented electrical steel sheets was first categorized to confirm its chemical composition, present phases and texture. Then, quasi-static tensile tests at both temperatures were run after which the data was analyzed and the tensile properties were extracted and modeled. Then, fractured surfaces of the samples were examined under a scanning electron microscope to investigate the failure mechanisms under the tensile loading condition. After the complete characterization of the tensile properties, cyclic tests at both temperatures were run after which the data was analyzed and the fatigue properties were

extracted and modeled. The failure mechanisms under cyclic loading were also investigated using scanning electron microscopy.

The sheets were confirmed to contain 3% silicon content with ferritic iron present. The steel sheets were also confirmed to have a body centered cubic crystal structure as well as a random grain orientation and texture. The tensile properties at room temperature and 150°C were calculated as well as modeled using the Ramberg-Osgood equation. The obtained elastic modulus for all three grades of non-oriented electrical steel sheets were found to be below the typically expected properties of structural steel but well within the range of electrical steels found in literature. The tensile properties along the rolling direction, transverse direction and 45° orientation were studied and similar results were obtained for the rolling and transverse directions while the results along the 45° orientation were noticeably different. The fracture surface revealed a mixture of ductile and brittle failure fracture mechanisms. A comparison between the three grades of non-oriented steel sheets and a comparison between the tensile properties at room temperature and 150°C was presented. It was found that the three grades of non-oriented electrical steel sheets had comparable tensile properties and there was no conclusive evidence that the sheet thickness had any effect on the tensile properties. It was also found that the increase in temperature had an adverse effect on the tensile properties of the steel sheets which was more significant in the yield strength and elongation.

The fatigue properties at room temperature and 150°C were also examined as well as modeled using the Basquin equation. In addition, design curves with reliability and confidence levels of 90% were obtained using the Owen's tolerance method. The fracture surface revealed a mixture of cyclic deformation and brittle failure fracture mechanisms. A comparison between the fatigue properties of the three grades was presented. Comparable lives at the similar

stress amplitudes were observed and with this observation, the conclusion that the sheet thickness did not have an effect on the fatigue life was reached. The effect of mean stress, temperature and cutting method on the fatigue life of non-oriented steel sheets were also investigated and presented. Similar to the tensile properties, increasing the temperature also had an adverse effect on the fatigue life by yielding lower lives at the same stress amplitudes at the elevated temperature. Extra tests performed at different load ratios showed that increasing the mean stress did not significantly affect the life at the same stress amplitudes but lowered the expected endurance strength of the material. Finally, the fatigue life of specimens cut with water-jet and CNC machining were compared. It was found that water-jet cutting deteriorates the edge roughness of the specimens which in turn adversely affects the fatigue life significantly.

Acknowledgements

For the chance to work on this project and for his tremendous assistance and direction at each stage of my study, I would like to convey my profound gratitude to my supervisor, Dr. Hamid Jahed.

I also want to express my gratitude to Dr. Behzad Behravesh and Dr. Dulal Saha for contributing their outstanding scientific expertise and technical know-how in the areas of conducting experiments, sample preparation, microscopy, and fractography.

The research performed in this thesis was financially supported by the Natural Sciences and Engineering Research Council of Canada (NSERC) Alliance with contributions from Stellantis under grant number ALLRP 556432 - 20.

Finally and most significantly, I want to thank my wonderful parents, Mr. Emmanuel Tolofari and Mrs. Ibelema Tolofari, for raising me with such a strong sense of duty and curiosity. They provided constant assistance, without which this effort would not have been possible.

Table of Contents

List of Figures

List of Tables

Chapter 1

Introduction

With its rising market, recent years have seen a surging growth in the development of electric and hybrid vehicles [1–3] to control the emission of green house gases. An active emission reduction strategy which removes the emissions of traditional internal combustion engines all together is the electrification of vehicles for which electric motors are an essential component. For fully electric vehicles, electric motors provide the full propulsion force required while for hybrid electric vehicles they may act as an integrated starter and generator to provide additional torque to the powertrain [2, 3]. At the core of the electric motors are permanent magnets rooted inside the rotors and as such, these rotors are required to be highly permeable with low magnetic losses and magnetostriction. To meet these material requirements, the high cost sintered rare-earth neodymium- iron-boron (NdFeB) alloys were a common choice [3, 4]. However, since their discovery at the start of the 20th Century, laminated thin non-oriented silicon steel sheets (also called non-oriented electrical steel sheets) have been the preferred material choice because of they meet the material requirements while remaining cost-effective [3, 4].

In general, electrical steels sheets contain between 0.5% to 6.5% silicon content. While increasing the silicon content improves the magnetic and electrical properties of electrical steels, it reduces their ductility. Commercially, the most widely available and used electrical steels contain about 3.25% silicon as higher silicon content makes the material too brittle for cold rolling [5]. Based on the orientation of their grain structure, electrical steels are categorized into two groups: non-oriented and grain-oriented electrical steels. Non-oriented electrical steels have a randomized grain structure with silicon content ranging between 0.5% to 3%. Due to their randomized grain structure, this category of electrical steels has uniform properties in all directions and does not need to undergo secondary recrystallization to develop their properties [5]. They also have low energy losses at high frequencies which allows them to be utilized in a variety of applications such as in motors, stators, and transformers [5]. The second category of electrical steels contain between 3% to 6.5% silicon and are called grain-oriented electrical steels. This category of electrical steels undergo secondary recrystallization which results in an improved grain structure in a preferred direction which most often is the rolling direction of the sheet. Grain-oriented electrical steels have a highly organized crystal structure and are extremely permeable with low magnetic losses [5]. The trade-off for the improved grain structure of these electrical steels is the relative reduction in applicability because the magnetic properties are uniform in all directions. Grain-oriented electrical steels are mainly utilized in the non-rotating parts of transformers.

Non-oriented electrical steels may be manufactured as fully processed or semi-processed where the end-user does the final annealing according to the application of the steels while grain-oriented electrical steels are always manufactured as fully processed. Several processes

are involved in the manufacturing of electrical steels [6, 7]. The first process is casting. In addition to the iron-silicon alloy, different elements may be added to the alloy to enhance or induce specific properties in the electrical steel sheets. Furthermore, the electrical steel sheets are reheated and hot rolled to dissolve most of the second phase precipitates. Then, cold rolling generates the primary recrystallization and reduces the thickness of the electrical steels sheet [7]. For grain-oriented electrical steel sheets, a final annealing process is done to selectively grow and orient the crystals to a preferred magnetization direction [4, 7]. A schematic of the manufacturing process used by an electrical steel manufacturing company [6] has been shown in Figure 1.1. In addition to these main processes, other processes such as insulation coating, decarburization and temper rolling are used to modify the final properties of the steel sheets. For cutting the electrical steel sheets to the specified shape, different methods may be used; mechanical cutting or punching is the most widely utilized method for this purpose due to its low cost [4]. Although after punching the edges become degraded which affects the microstructural, magnetic and mechanical properties, simply polishing the edges after the punching process has been shown to significantly improve these properties. [2, 8, 9].

Despite the abundance of literature on the electrical and magnetic properties of non-oriented electrical steels, studies on the mechanical properties are scarce an even more so in fatigue. A crucial aspect of durability designs is the availability of mechanical property data of material grades. However, national and international standards only specify and guarantee the magnetic properties. As a result, manufacturers of electrical steel typically only state the tensile properties. Furthermore, since the composition is not standardized either, the mechanical properties of the grades of steel differ between manufacturers [3]. Suppliers of

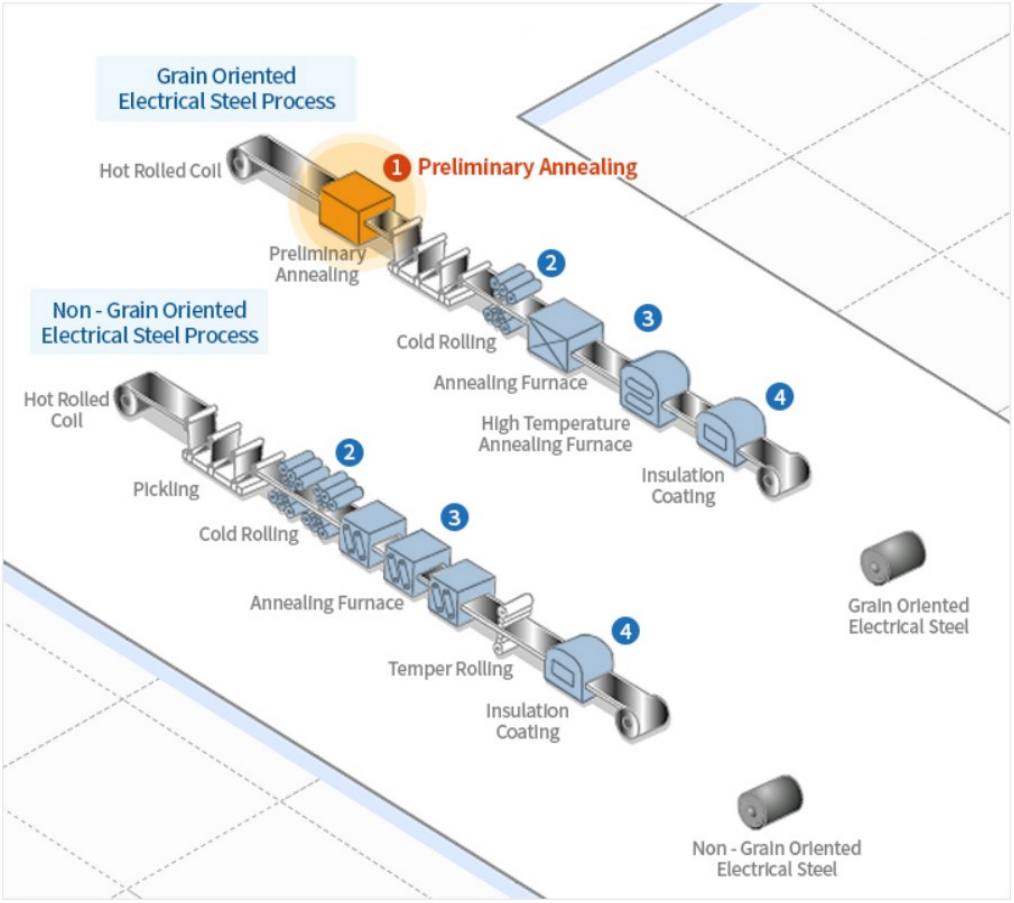

Figure 1.1: *Manufacturing Process of Electrical Steel [6]*

these steels carefully control magnetic properties and to a lesser extent tensile properties and this poses a challenge during the structural and durability assessment of electrical motors where electrical steel is applied [2]. Considering its applications, the motors are subjected to different stresses such as tensile stresses induced by centrifugal forces during high speed rotation and from permanent magnet inserts (see Figure 1.2) [2,3], circumferential or tangential inertia loads as the rotor accelerates and decelerates and areas with high stress concentration (see Figure 1.2) [3]. Furthermore, alternating stress occurs between full stop, maximum RPM and intermediate speed changes [2]. Moreover, the high working temperature caused by the electric motor operation requires that fatigue performance of

electrical steels be investigated at this temperature. Very limited studies have examined the effect of temperature (only up to 100°C) on the fatigue behavior [3]. This is why the mechanical characterization of thin electrical steel sheets at different temperatures is necessary and of interest.

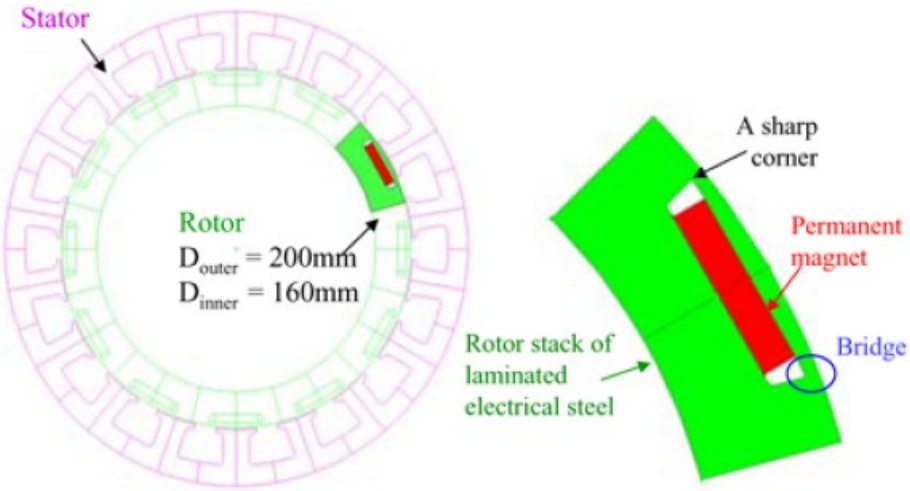

Figure 1.2: *An example of an internal permanent magnet rotor design [3]*

1.1 Research Objectives

The overall goal of this project is to characterize the mechanical behavior of non-oriented electrical steel sheets used in electric vehicles (EV) to establish a link between material microstructure and its mechanical performance. This project aims to deliver a very needed library of properties as well as in-depth understanding of the microstructural and mechanical behavior of non-oriented electrical steels, which is an essential knowledge base for computer aided engineering (CAE) of EV power train and will enable optimum durability design of electric engines. To achieve the goals of this project, the following objectives of this thesis

are outlined, described and pursued.

- **Microstructural properties of non-oriented electrical steel sheets**

  Microstructural examinations will be conducted on three grades of non-oriented electrical steel sheets to develop a knowledge base to correlate with the mechanical properties of the material.

- **Quasi-static tensile properties of non-oriented electrical steel sheets**

  Quasi-static tensile tests will be performed on three grades of non-oriented electrical steel sheets at room temperature and an elevated temperature of 150°C along the rolling direction, transverse direction and at a 45° orientation to fully categorize the tensile properties as well as a extracting the tensile model parameters to model the tensile behaviour at both room temperature and 150°C. The range of temperatures was chose to to represent the working temperature of electric motors [10]. Finally, the effect of temperature on the tensile properties will be investigated.

- **Cyclic properties of non-oriented electrical steel sheets**

  Cyclic tests will be performed on three grades of non-oriented electrical steel at room temperature and on one grade at an elevated temperature of 150°C along the rolling direction. Fatigue parameters for modeling the behaviour under cyclic loading at both temperatures will be extracted and a complete statistical analysis based on a 90% reliability and 90% confidence level (R90C90) will be performed on the obtained test results to obtain the fatigue design curves and parameters. Finally, the effect of temperature on the fatigue life will be investigated.

- **Identifying tensile and fatigue failure mechanisms**

Following the tensile and fatigue testing of the sheets, the fractured surfaces will be analyzed using scanning electron microscopy technique to identify the deformation and failure mechanisms under the respective loading conditions.

1.2 Thesis Overview

This thesis consists of four major parts: literature review; mechanical characterization of non-oriented electrical steel sheets at room temperature; mechanical characterization of non-oriented electrical steel sheets at an elevated temperature of 150°C and a study on the effects of mean stress and cutting method on the fatigue life of non-oriented electrical steel sheets. An in-depth look into the chapters is given below.

Chapter 2 gives review on the available literature pertaining to non-oriented electrical steel. The literature review includes a description of the studied grain morphology and distribution, texture, phases and precipitates present as well as their effect on the mechanical properties. The available literature on the tensile and fatigue properties were also reviewed including the fractography of the fractured surfaces to identify the fracture mechanisms as well as the effect of some manufacturing methods on the residual stresses, edge microstructure and micro-hardness.

Chapter 3 gives an overview of the methodology used in the microstructural and mechanical characterization of the non-oriented electrical steel sheets. It includes the specimen extraction method and the experimental details of the tests that were performed.

Chapter 4 presents and discusses the microstructure of the grades of electrical steel being investigated. The results of this chapter include the chemical composition, grain morphology and distribution, phases and precipitates present, grain orientation and texture.

Chapter 5 presents the results of the quasi-static tensile tests performed on three grades of electrical steel at room temperature. It presents and discusses the tensile properties well as the parameters for modelling the tensile behaviour of the electrical steel sheets at room temperature. The fracture surfaces from the tensile tests at room temperature as well as the identified fracture mechanisms are also presented in this chapter.

Chapter 6 presents the results of the quasi-static tensile tests performed on three grades of electrical steel at an elevated temperature of 150°C. It presents and discusses the tensile properties well as the parameters for modelling the tensile behaviour of the electrical steel sheets at 150°C. which leads to a discussion on the effect of temperature on the tensile properties. Finally, the fracture surfaces from the tensile tests at 150°C as well as the identified fracture mechanisms are also presented in this chapter.

Chapter 7 presents the results of the cyclic tests performed on the three grades of electrical steel at room temperature. It presents and discusses the fatigue properties well as the parameters for modelling the fatigue behaviour of the electrical steel sheets at room temperature. A design curve with a reliability and confidence level of 90% is presented as well. The fracture surfaces from the cyclic tests at room temperature as well as the identified

fracture mechanisms are also presented in this chapter.

Chapter 8 presents the results of the cyclic tests performed on the one of the grades of electrical steel at an elevated temperature of 150°. It presents and discusses the fatigue properties well as the parameters for modelling the fatigue behaviour of the electrical steel sheets at 150°C. A design curve with a reliability and confidence level of 90% is presented as well as well as a look into the effect of temperature on the fatigue properties. Finally, the fracture surfaces from the cyclic tests at 150°C as well as the identified fracture mechanisms are also presented in this chapter.

Chapter 9 presents a study on the effects of the cutting method and mean stress on the fatigue life of non-oriented electrical steel. Fatigue specimens were extracted using two different methods and were tested under cyclic loading. Furthermore, limited tests were performed at three different load ratios to investigate the effect of mean stress on the fatigue life. The results of these investigations are presented in this chapter.

Finally, chapter 10 gives a summary of the work presented in this thesis from chapters 3-8 as well as the contributions made by this research and recommendations for the direction of future work in this area.

Chapter 2

Background and Literature Review

2.1 Electric Motors

An electric motor is a device consisting of a stator (stationary component) and a rotor (rotating component) that works under the principle of electromagnetic induction and converts electrical energy to mechanical energy (usually torque) through the interaction of magnetic fields generated by an electric current [11, 12]. Electric motors are utilized in a variety of applications ranging from simple household items such as electric toothbrushes to providing the starter force in electric vehicles. In the basest form, there are two main kinds of electric motors: direct current (DC) motors which are further divided into brushed and brushless DC motors and alternating current (AC) motors which are further divided into synchronous and asynchronous (induction) AC motors [12]). Electric vehicles in Europe and North America generally use induction motors (see Figure 2.1) which are more reliable than brushed DC motors, less expensive than brushless DC motors [13] and operates by applying a three phase AC current to the stator which then generates a rotating magnetic field that in turn causes a

magnetic field in the rotor by electromagnetic induction. The interaction of these magnetic fields generates an electromagnetic force according to Lorentz law [14] which causes the rotor to rotate which can then be converted into different types of motion through the use of gears. In these motors, the core of the stators and rotors are made up of stacked thin sheets of a highly permeable material that have been laminated together (see Figure 2.2).

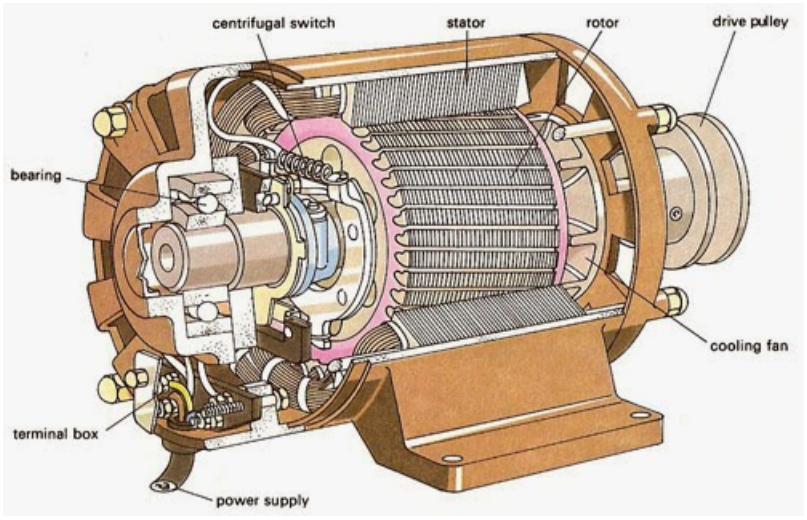

Figure 2.1: *Induction Motor [15]*

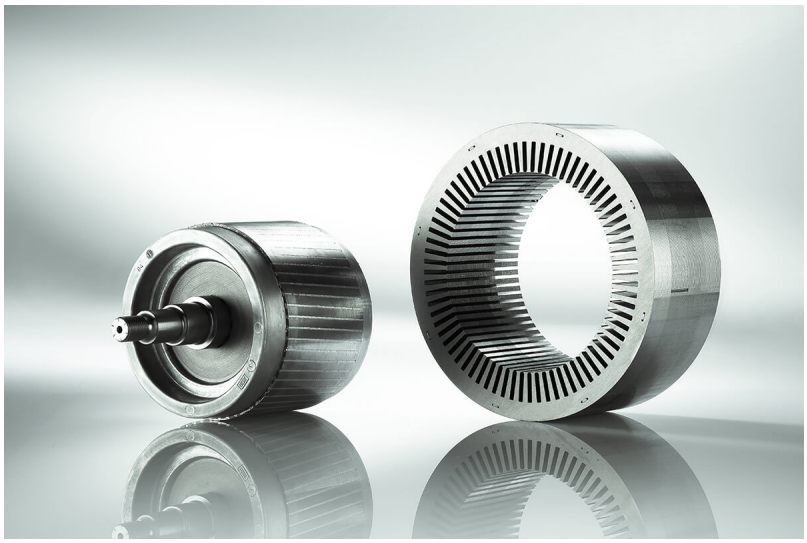

Figure 2.2: *Image showing the laminated steel core of a rotor (left) and a stator (right) [16]*

The material used as the core of stators and rotors need to have specific properties [5, 17]. These properties are listed include:

1. **High permeability** to ensure the material has an increased capacity to support magnetic fields [4, 5, 17].

2. **Low magnetostriction** to ensure the material has a low tendency to expand or contract in a magnetic field [4, 5, 17].

3. **High electrical resistivity** to minimize the core loss by reducing the eddy current component [5, 17].

4. **Low hysteresis** loss to ensure the minimal energy is wasted in the form of heat from an alternating magnetizing force [5, 17].

Electrical steel is a cost-effective material that meets these requirements [3, 4]. An example is shown in Figure 2.3 which gives a comparison of a typical hysteresis curve comparison between electrical steel and mild steel and just from a visual inspection, the hysteresis loss, which is proportional to the area of the respective loop, of electrical steel is clearly much lower than that of mild steel. Meeting these requirements as well as being low-cost makes electrical steel very desirable [4, 18]. More specifically, non-oriented electrical steels are utilized in the stators and rotors of electric vehicle motors because of their randomized grain structure that allows uniform magnetic properties irrespective of the sheet orientation. The microstructure of non-oriented electrical steel sheets is discussed in the following section.

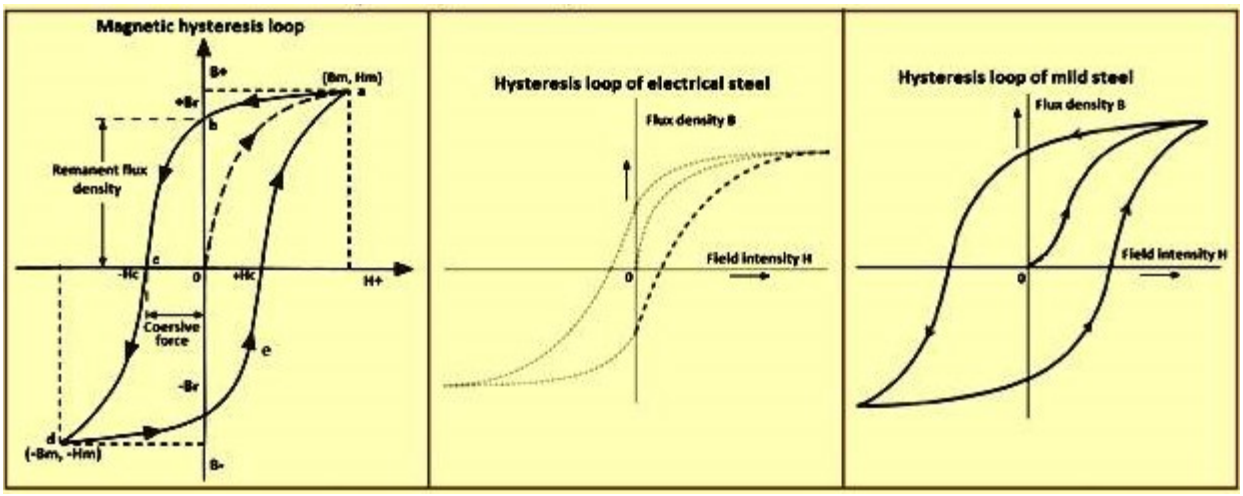

Figure 2.3: *Magnetic Hysteresis Loop of Electrical Steel and Mild Steel [18]*

2.2 Electrical Steel Microstructure

In thin sheets of non-oriented electrical steel, the size of the grains are often on the same order of magnitude as the sheet thickness (shown in Figure 2.4) and as such, only a few grains are present across the sheet thickness [19]. The presence of few and large grains implies a reduction in grain boundaries which affect the bulk material properties such as the strength, ductility and texture development [20]. From the Hall-Petch relation [21], the strength of steel is expected to decrease with increasing grain size [22].This was observed in tests performed by Lakkonavar et al. [2] and Gao et al. [3] who recorded the elastic modulus of non-oriented electrical steel at 170GPa along the rolling direction which is lower than the generally accepted 195GPa-210GPa range of structural steels [3]. Furthermore, since the deformation response of a material is dependent on the number, size, distribution, and orientation of grains [20], the presence of few and large grains across the thickness will lead to deformation anisotropy.

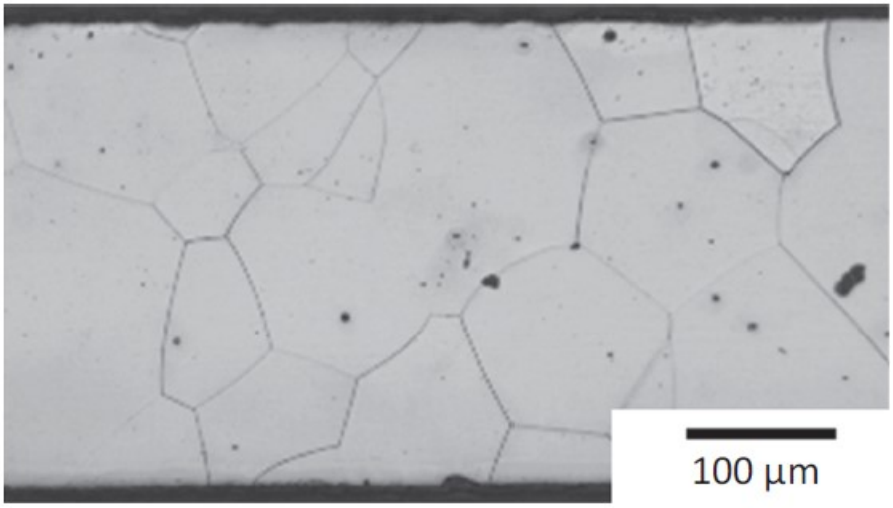

Figure 2.4: *Micrograph of Electrical Steel along the thickness direction [19]*

According to the Fe-Si binary phase diagram [23] shown in Figure 2.5, non-oriented electrical steels containing between 2.5% to 5% silicon content contain ferritic iron at all temperatures up to their melting point which would give the alloy a body centered cubic crystal structure (BCC) within the same temperature range. Out of the three well known slip systems ({110}<111>, {112}<111>, {123}<111>) for BCC materials, non-oriented electrical steels only exhibit the {110}<111> slip [24] which would reduce the paths for dislocation movement and results in less ways to accommodate for plastic deformation through dislocation slip. Regarding the magnetic applications, the crystallographic texture is the most important factor that controls the magnetic permeability and core loss of non-oriented electrical steels with the cube texture, {001}<100>, being the ideal and most desired texture for this category of electric steels since it allows for the magnetization direction to be parallel to the plane of the steel sheet [4, 5, 25]. However, the difficulty in producing this texture commercially is added to by the fact that the main recrystallization direction of non-oriented electrical steel sheets is the <111> direction which coincidentally is the most difficult direction

to magnetize as it is the furthest from the ideal <001> direction [4]. Presently, texture improvement is achieved by reducing the volume fraction of the grains oriented in the <111> direction while increasing the volume fraction of the grains oriented in the <001> direction [4]. To control the texture development in these steel alloys, precipitates and inclusions such as aluminium nitride, manganese sulphide, and phosphorus are used [4, 26].

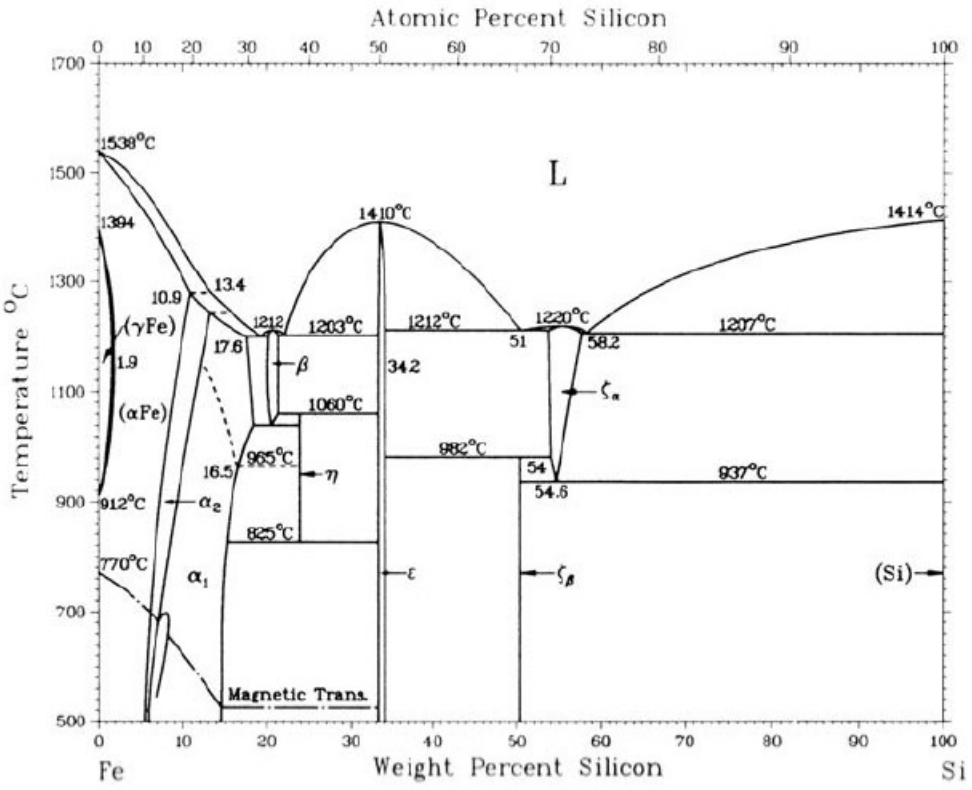

Figure 2.5: *Fe-Si Binary Phase Diagram [23]*

Other precipitates such as copper and manganese have also been shown to strengthen the material through solid solution and precipitate strengthening by impeding the motion of dislocations [20, 26–28]. Lee et al. [26], found and showed in Figure 2.6 that non-oriented electrical steels with phosphorus added had a higher fraction of grains with the desired {001}<100> texture and a lower {111}<112> texture. Furthermore, they [26] also showed

in Figures 2.7 that the grain size decreased with the addition of phosphorus due to the restriction of grain growth during recrystallization by the segregation of phosphorus at the grain boundaries.

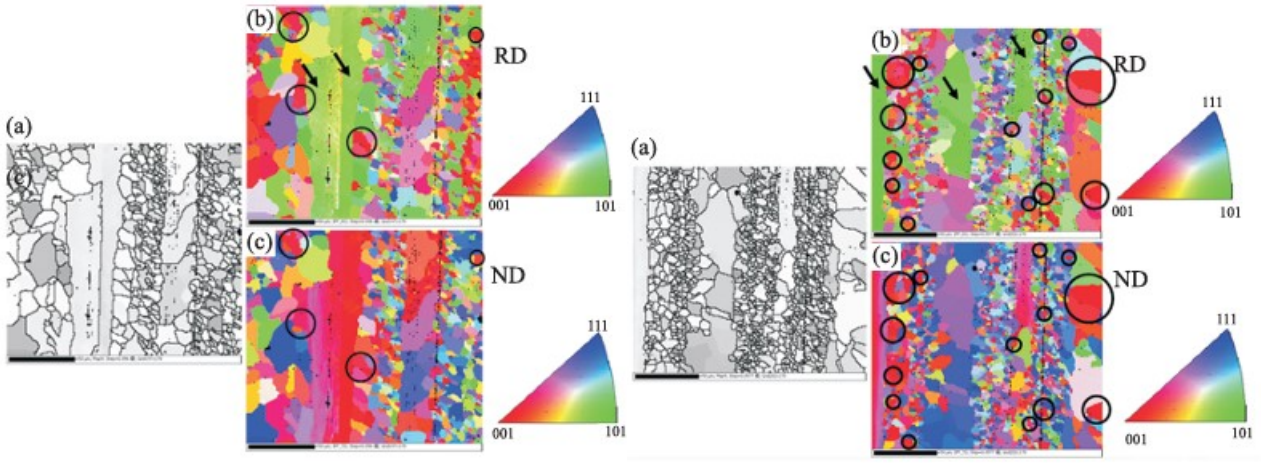

(a) (b)

Figure 2.6: *Orientation map image of Non-Oriented Electrical Steel (a) without Phosphorus (b) with Phosphorus added [26]*

A similar effect on grain size was recorded for Manganese by Schulte et al. [28] shown in Figure 2.8 although the development of the grains were also affected by its addition as shown in Figure 2.9. More specifically, the grain growth rate slowed as annealing time increased [28]. These precipitates and inclusions are however temperature dependent [4]. Figure 2.10 shows the stability plot of precipitates in non-oriented electrical steel.

The orientation of grains are further affected by the manufacturing method. Punching or stamping which is one of the popular methods by which the material is cut because of its ease and low cost, seems to have a detrimental effect on the orientation of the grains as well as introducing residual stresses near the punched edge of the non-oriented electrical

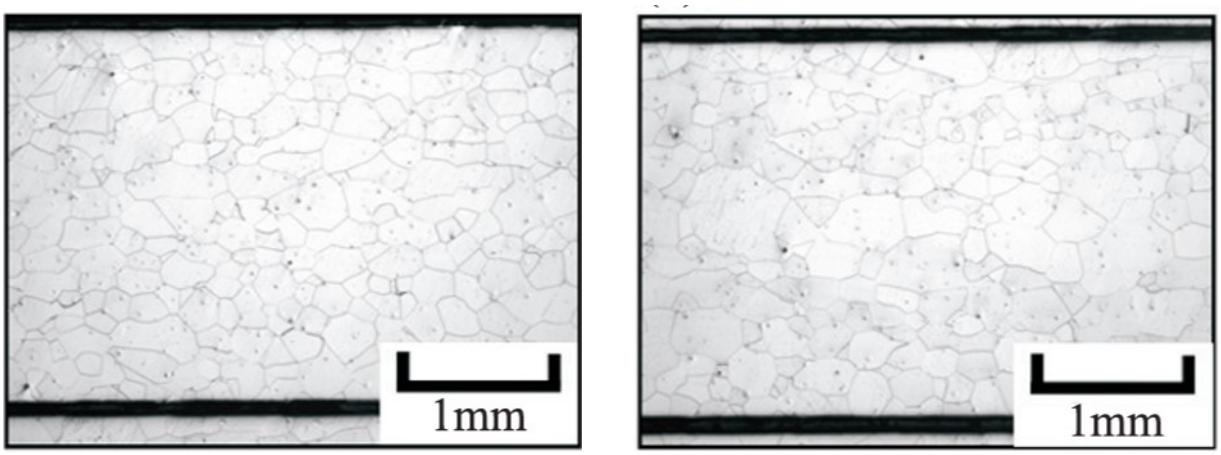

(a) (b)

Figure 2.7: *Orientation map image of Non-Oriented Electrical Steel (a) without Phosphorus (b) with Phosphorus added [26]*

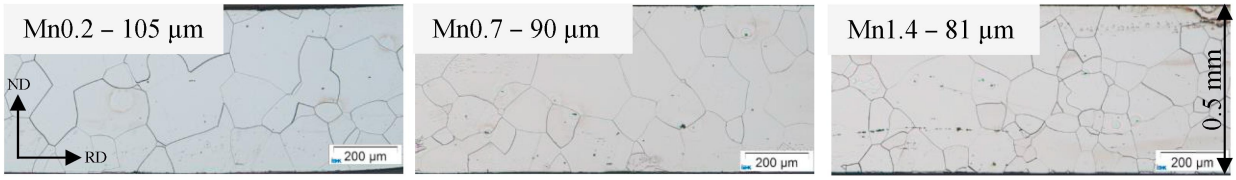

Figure 2.8: *Microstructure of different concentrations of Mn after final annealing at 1000 °C for 120s [28]*

steel sheets [2, 3, 9, 19]. In Figure 2.11a, the distorted grains of the punched edge can be seen clearly and this distortion has been observed to extend about 100µm from the edge into the sample [8, 9]. Through the use of the Electron Back Scatter Diffraction (EBSD) technique, Wu et al. [9] revealed in Figure 2.11b that majority of the crystals at the sheared edge orient towards the least favourable <111> direction. In addition to this, they [9] also investigated the effect of punching on microhardness and small angle grain boundary using the Vickers HV0.1 method and EBSD respectively. The results presented in Figure 2.12a

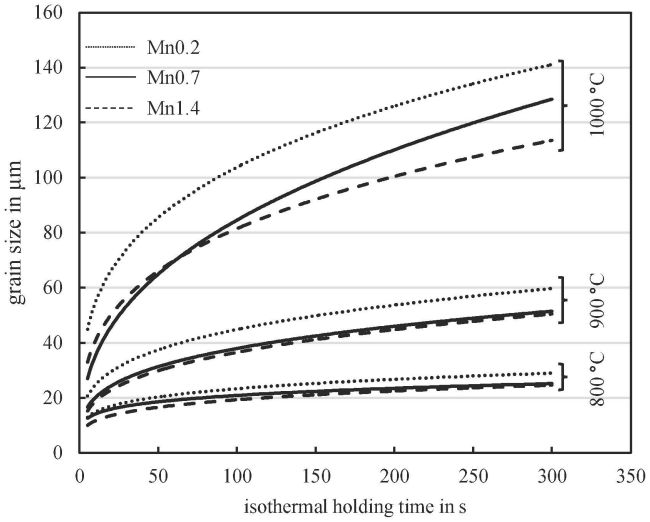

Figure 2.9: *Grain growth during heat treatment at 800°C, 900°C and 1000°C [28]*

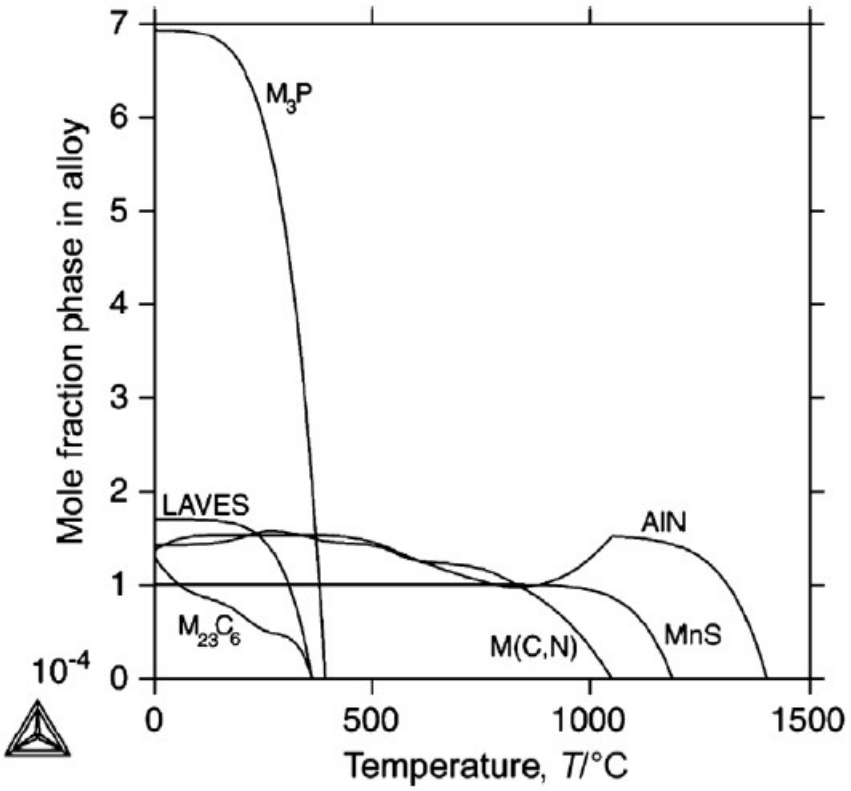

Figure 2.10: *Stability Plot of Precipitates in Non-Oriented Electrical Steel with Temperature [4]*

show a dramatic reduction in the hardness as the distance from the punched edge increases. The increase in hardness at the punched edge is a consequence of the work hardening from the dislocation accumulation at the cell walls caused by the punching process [9]. Figure 2.12b shows that the fraction of small angle grain boundaries in the sheared edge is larger than that in the centre of the specimen. The dislocations formed from the punching process pile up to form a dislocation cell and after an extent evolve to form a small angle grain boundary [9]. These deformation pile ups impede plastic deformation and lead to the effect of work hardening. Finally, although relievable to a good extent by a simple annealing process, the presence of compressive residual stresses (Figure 2.13) at the punched edge is another effect the punching process [8].

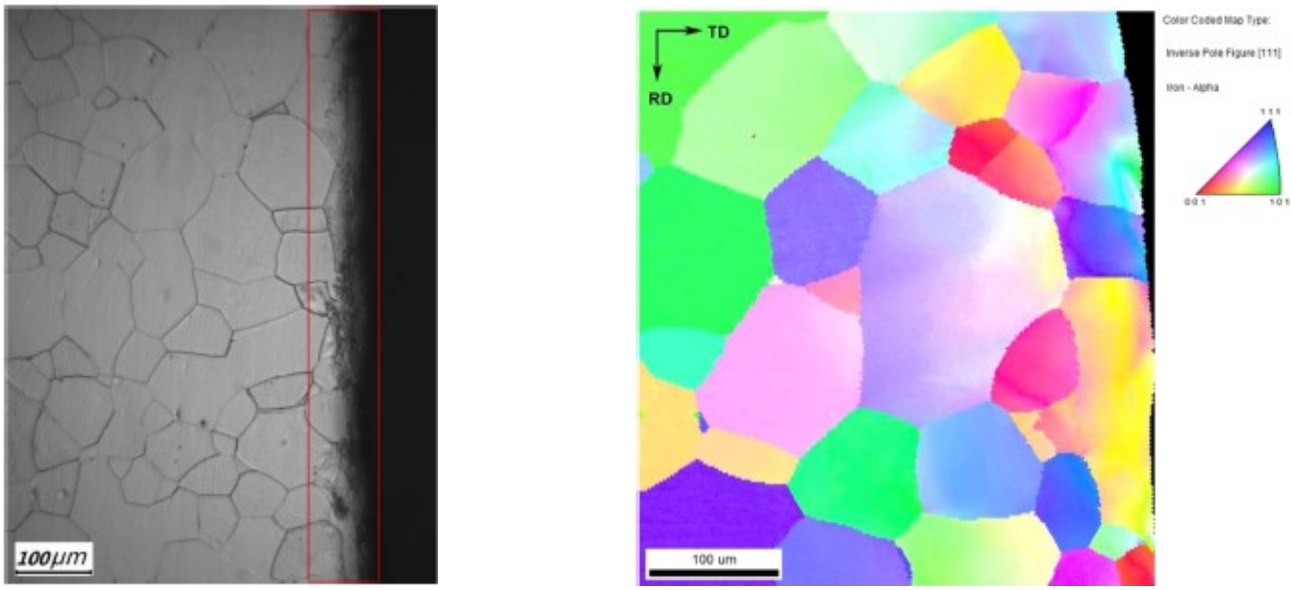

(a) (b)

Figure 2.11: *Microstructure and EBSD image of (a) distorted grains along the punched edge (b) orientation of grains at punched edge respectively [9]*

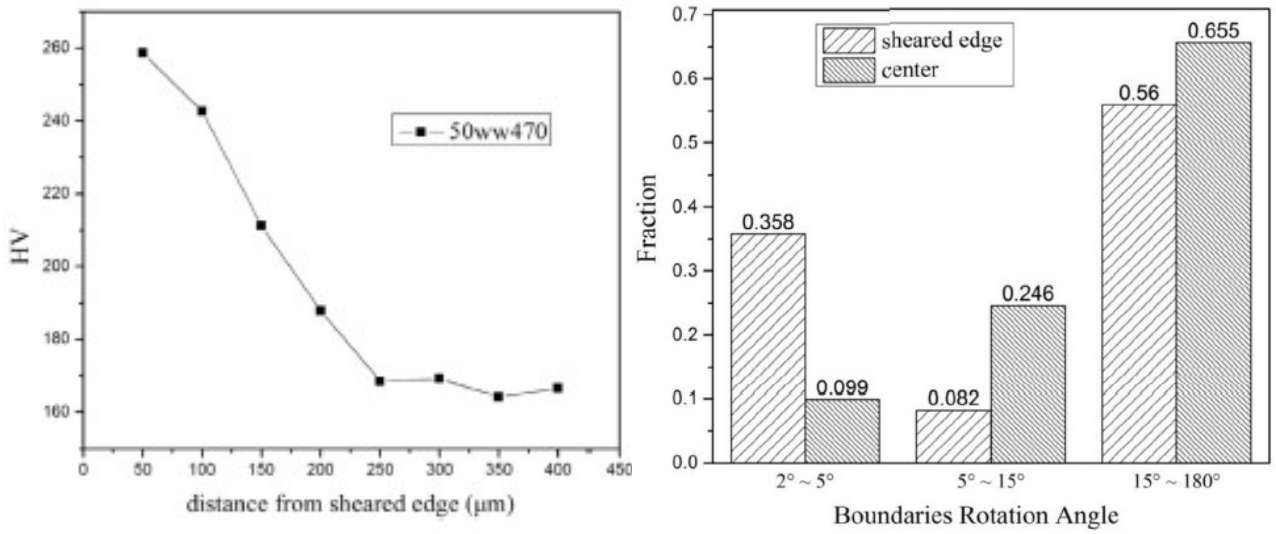

(a) (b)

Figure 2.12: *Plot Showing (a) Microhardness from Sheared Edge (b) Fraction grain boundary angles at Centre vs Punched Edge [9]*

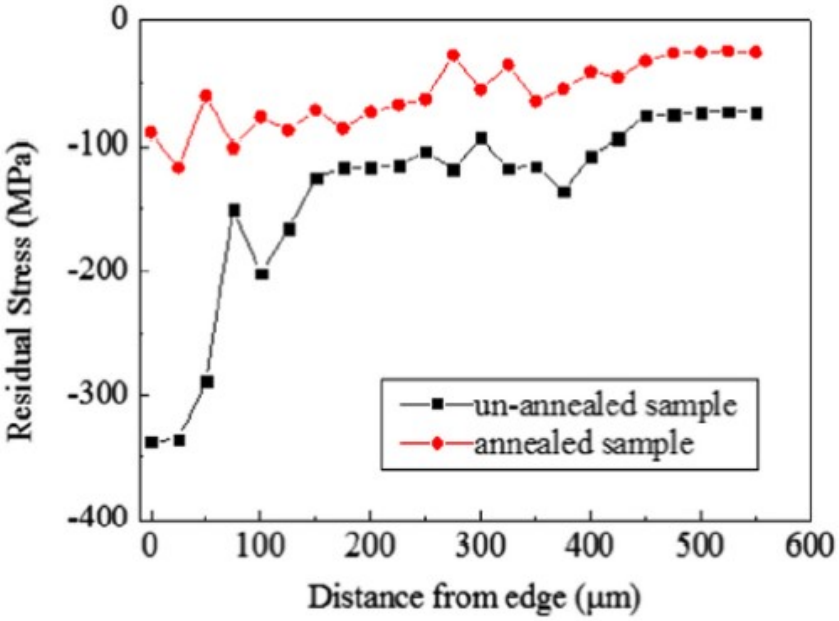

Figure 2.13: *Residual stress distribution in samples before and after annealing [8]*

2.3 Quasi-static Behaviour

2.3.1 *Quasi-Static Tensile Testing*

Quasi-static tensile testing is one of the various mechanical testing methods used to measure a material's strength and other properties of interest such as the elastic modulus, ductility, poisson's ratio and relationship between the stress and strain under a tensile load [29–32]. This test involves slowly pulling a sample specimen of a material with a uniaxial force until it breaks [29, 32]. The specimen may be smooth or have pre-existing defects such as notches or cracks machined into it and its geometry may be cylindrical or flat (see Figure 2.14). The specimen geometries, testing methods and procedures are outlined in standards given by the American Society for Testing and Materials (ASTM) [29, 33] and appeared in many recent publications from the Fatigue Analysis and Design Laboratory (FATSLab) at the University of Waterloo [30, 34–36].

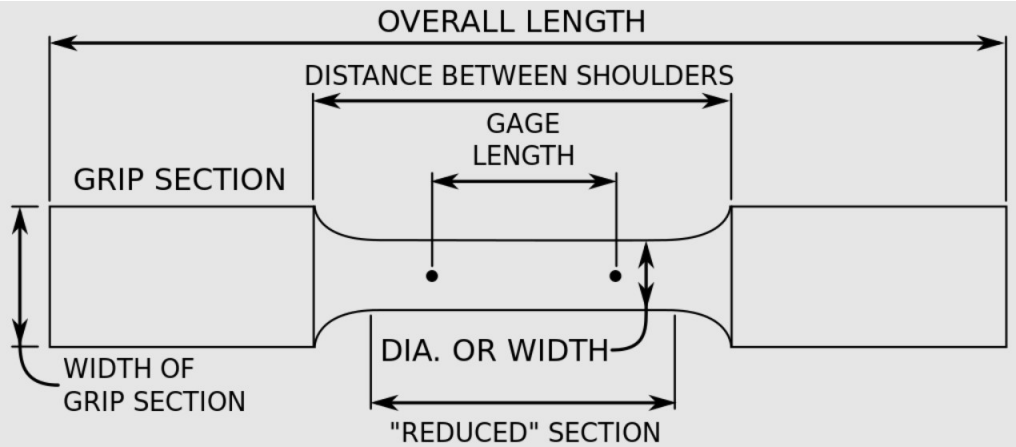

Figure 2.14: *Flat specimen for tensile testing of metals [37]*

The tensile test is conducted in such a manner that the specimen is deformed at a constant speed and as such, the uniaxial force (P) required to achieve this displacement rate varies as

the test proceeds [29,33]. This force can then be divided by the initial area (A_i) to obtain the engineering stress ($\sigma = \frac{P}{A_i}$) [29,38,39]. The displacement of the specimen is measured within the gauge length and from this displacement, the engineering strain ($\epsilon = \frac{\delta L}{L_i}$) is calculated by dividing the change in length within the gauge section (δL) by the initial length of the gauge section (L_i) [29, 38, 39]. The plot of engineering stress (σ) vs engineering strain (ϵ) gives a graphical representation of the relationship between stress and strain for the duration of the tensile test. It is often useful in certain situations to work with the instantaneous values of stress and strain, referred to as the true stress and true strain [29]. These parameters utilize the finite change in the cross-sectional area and length within the gauge section of the specimens to measure the true stress ($\sigma_T = \frac{P}{A}$) and true strain ($\epsilon_T = \int_{L_i}^{L} \frac{\delta L}{L}$) [29]. For small strains, the engineering and true stress-strain curves are identical and up to the engineering ultimate strength are related by the equations given in Equations 2.1 and 2.2 [29, 39]. A schematic of the stress-strain curve is presented in Figure 2.15 with the solid line representing the engineering stress-strain curve and the dotted line representing the true stress-strain curve.

$$\sigma_T = \sigma(1 + \epsilon) \tag{2.1}$$

$$\epsilon_T = ln(1 + \epsilon) \tag{2.2}$$

Various properties can be derived from the engineering stress-strain curve (see Figure 2.15). These properties are described below:

1. **Elastic Modulus**: The elastic or Young's modulus (E) is a measure of a materials

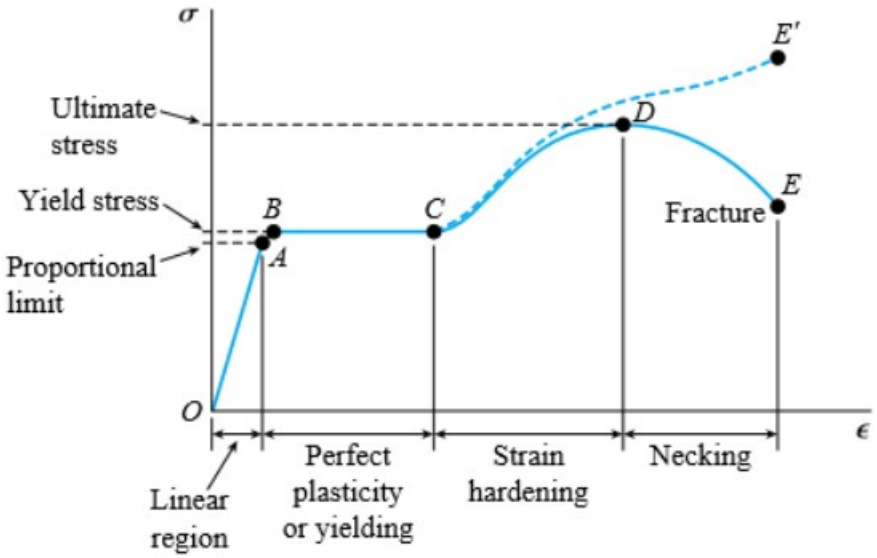

Figure 2.15: *Stress-Strain Curve Schematic [40]*

ability to resist elastic deformation. It is calculated as the slope of the linear region of the engineering stress-strain curve [29, 39]. Within this linear region, the stress and strain are related linearly by Hooke's law ($\sigma = E\epsilon$) with the elastic modulus being the constant of proportionality [29].

2. **Proportional Limit**: This is defined as the point where the relationship between the stress and strain is no longer linear [29]

3. **Yield Strength**: The yield strength although often separate from the proportional limit, they are equivalent for most metals [29]. The yield strength is defined as the stress where plastic or inelastic deformation begins to occur and the material begins to harden with increasing strain (strain hardening) [29,39]. It is determined by the offset method where a straight line parallel to the linear region is offset by an arbitrary strain amount and where this line intersects the curve is termed the offset yield strength [29, 39]. For

metals, the accepted and widely used offset is a 0.0002 or 0.2% amount of strain (see Figure 2.16) [29, 39].

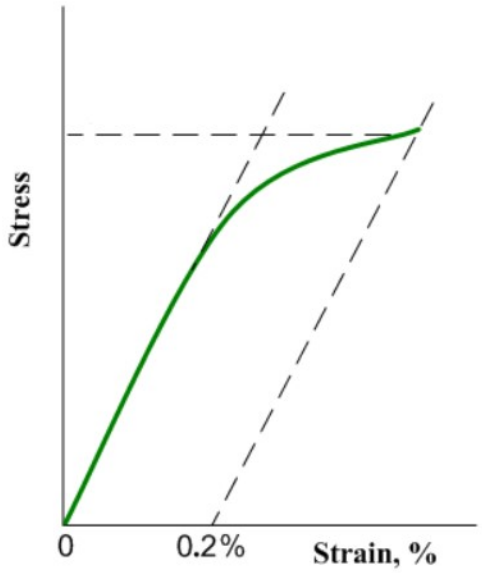

Figure 2.16: *0.2% Offset Yield Strength Schematic [41]*

4. **Engineering Ultimate Strength**: Also simply called the ultimate strength, this is the largest value of stress recorded on the engineering stress-strain curve [29, 38, 39]. After this stress value has been reached the material begins to soften with increasing strain (strain softening) and the phenomenon known as necking which is a local reduction in the cross-sectional area begins to occur [29, 39].

5. **Engineering Fracture Stress and Strain**: This is the engineering stress and strain value at which the material breaks [29]. The fracture strain (also known as the elongation at fracture) is a measure of the materials ductility [29,39]. Another measure of a materials ductility is the percent reduction in area which is defined by the change in cross-sectional area between the initial (A_i) and fractured specimen (A_f) divided by

the initial cross-sectional area ($\frac{A_i - A_f}{A_i} * 100\%$) [29, 39].

While the linear portion of the stress-strain curve is modeled using Hooke's law of elasticity ($\epsilon_e = \frac{\sigma_T}{E}$) [42], the plastic region, specifically the region of strain hardening, is modeled using Ramberg-Osgood's power law: $\epsilon_p = (\frac{\sigma_T}{H})^{\frac{1}{n}}$ [42] where H and n are Ramberg-Osgood parameters named the strength coefficient and the strain hardening exponent respectively (in this form, the Ramberg-Osgood parameters are the same as the Holloman parameters [43]). These parameters are derived by fitting the experimental data to the power law and finding the slope and intercept of the resulting curve in a log-log plot [42]. The Ramberg-Osgood equation then models the true or engineering stress-strain curve up to the ultimate strength and is given in Equation 2.3

$$\epsilon = \frac{\sigma}{E} + (\frac{\sigma}{H})^{(\frac{1}{n})} \tag{2.3}$$

2.3.2 *Tensile Properties of Non-Oriented ELectrical Steel Sheets*

While the Young's modulus for non-oriented electrical steel sheets are relatively constant among different authors [2,3], the variation for yield strength is much wider in the literature. Although both authors performed tensile tests on similar compositions of electrical steel which differed only in thickness (0.25mm and 0.27mm, respectively) and cutting method, Gao et al. [3] recorded the average yield strength at about 342MPa and 362MPa in the rolling and transverse direction, respectively while Lakkonavar et al. [2] recorded the yield strength as 417MPa in the rolling direction.

From the tensile tests on specimens cut from a 0.3mm thick non-oriented electrical steel sheet with 3.3 wt% silicon content by high precision spark erosion, Bode et al. [19] showed that

although the tested specimens had substantial elongation, the stress-strain curve (Figure 2.17) showed little to no strain-softening regime after the ultimate tensile strength which means the samples fractured shortly after reaching the ultimate tensile strength and did not display global necking. The absence of a strain softening regime was attributed to the size and limited number of grains across the thickness [19]. Depending on the edge finish, non-oriented electrical steels typically show elongations between 17% to 21% [2, 3].

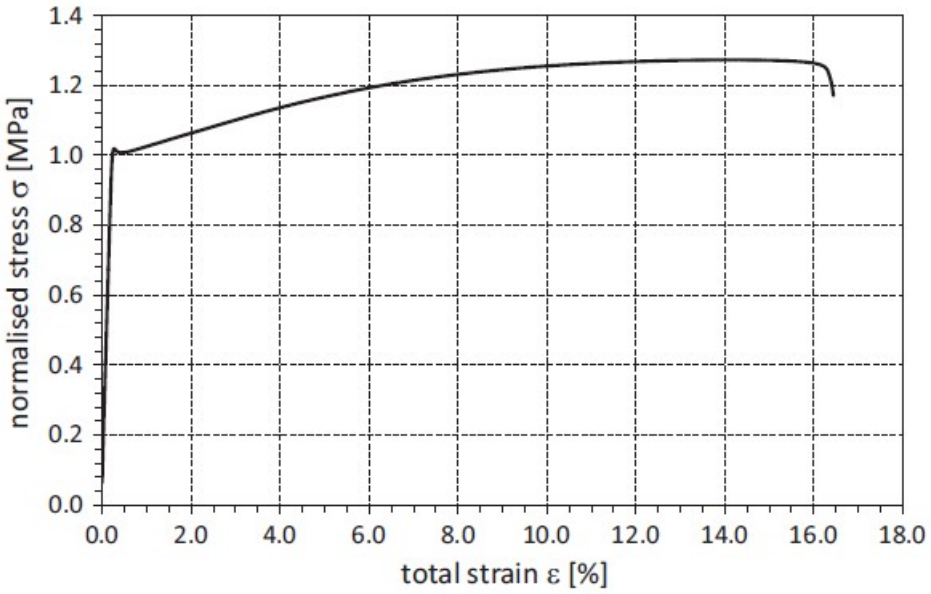

Figure 2.17: *Stress-Strain Curve normalized by the Yield Strength [19]*

The failure mode in the tensile tested specimens was concluded to be in the ductile-brittle transition mode [19]. While the majority of the fracture surface displayed brittle fracture evidenced by cleavage facets covering most of the fracture surface shown in Figure 2.18a, local necking was also observed in some areas shown in Figure 2.18b. Furthermore, the strain field during the tensile test was observed by Bode et al. [19] to be a distribution of strain bands across the gauge length of the specimens instead of a localized region of strain

accumulation. Figure 2.19 shows the strain distribution at the ultimate tensile strength captured using digital image correlation [19].

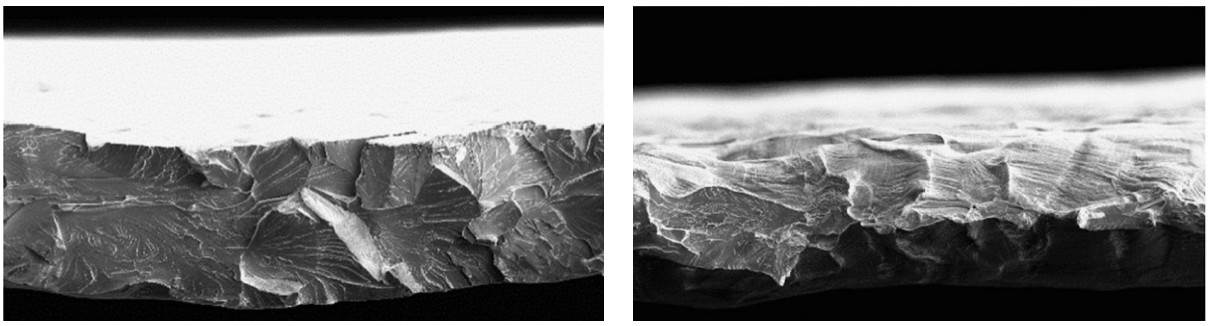

(a) (b)

Figure 2.18: *SEM image showing (a) area of local necking [8]; (b) cleavage Facets [19]*

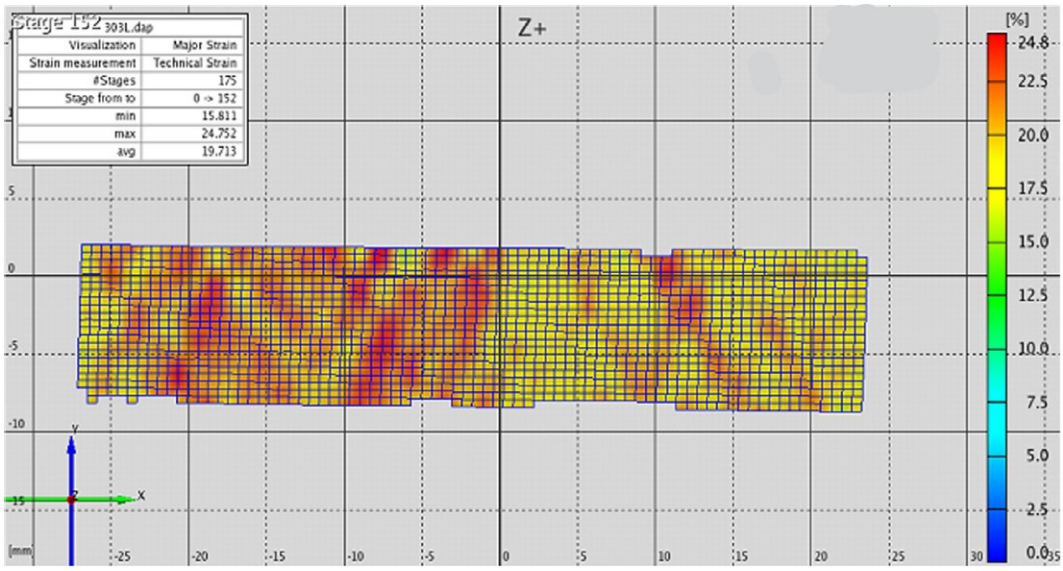

Figure 2.19: *Plastic strain distribution at the Ultimate Tensile Strength [19]*

As stated earlier, precipitates like copper and manganese have been shown to strengthen the material through grain boundary and dislocation strengthening by impeding the motion of dislocations, solid solution, and precipitate strengthening [20, 26–28]. Figure 2.20a shows the effect of aging non-oriented electrical steel with copper on the yield strength, tensile

strength and percent elongation while Figure 2.20b shows the effect of Manganese content on the same mechanical properties. From Figure 2.20a the yield and tensile strength both peaked in value after about 25 minutes of aging and then reduced with increasing aging time; this was attributed to over-aging while the percent elongation continuously decreased with the aging time with an even steeper slope after 45 minutes of aging. The strengthening effect of the copper precipitates was estimated to be about 207MPa [27]. For the manganese precipitates, the strengths peaked at about 0.6wt% Mn while the percent elongation increased with increasing manganese content although the rate of increase decreased [28]

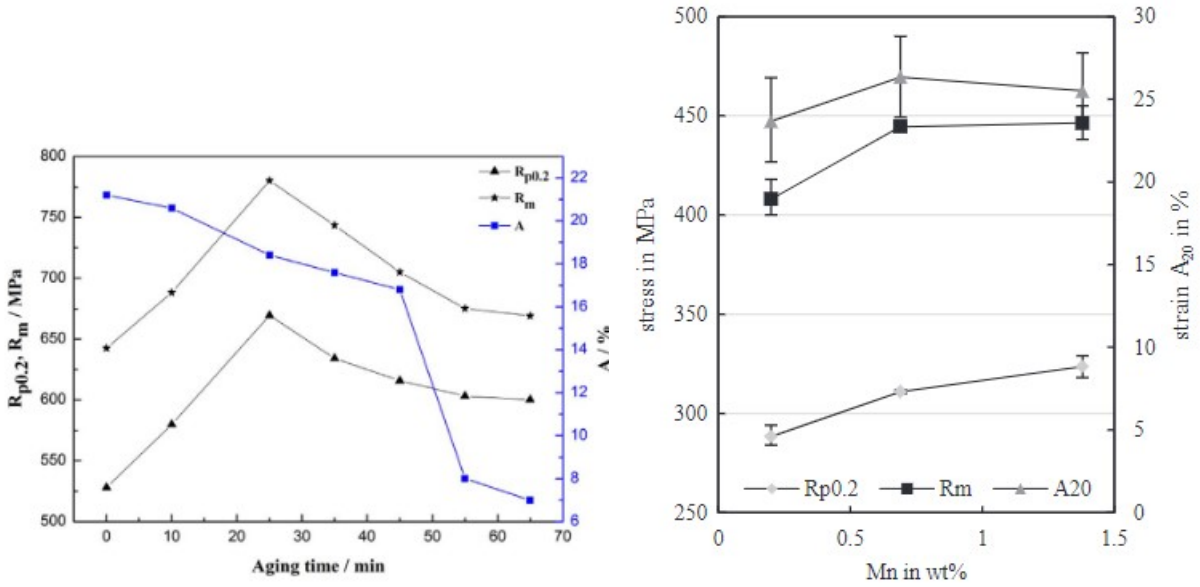

(a) Copper Precipitate Strengthening [27] (b) Manganese Precipitate Strengthening [28]

Figure 2.20: *Effect of Copper and Manganese Precipitates on the Mechanical Properties of Non-Oriented Electrical Steel [27, 28]*

2.4 Fatigue Behaviour

2.4.1 *Fatigue Testing*

Mechanical components are often subjected to repeated loads which lead to microscopic damages in the material [29]. Over time, these microscopic damages accumulate and develop into a crack, which when a critical crack length has been reached, may lead to the sudden failure of the component even at stresses well below the expected strength of the material [29,44]. Fatigue is therefore the progressive, localised weakening of a material when subjected to repeated cyclic loads and fatigue tests measure the resistance of materials to damage, strength loss and the fatigue life under such loads [44–46]. The fatigue life refers to the number of cycles (N_F) or reversals ($2N_f$) to a pre-determined crack length when the specimen is under cyclic loading [47]. There are three major approaches to conducting fatigue tests which are the stress-based approach, strain-based approach and the fracture mechanics approach which specifically treats growing cracks by the methods of fracture mechanics [29, 46, 48]. The stress and strain based approaches are discussed is more detail below.

1. **Stress-based Approach**: Also called the stress-life (S-N) approach, this method analyzes the nominal stresses in the affected region of the mechanical component [29]. The S-N approach is often used in design applications where the applied stress is expected to be primarily within the elastic range of the material [29, 49, 50]. This approach is more reliable in high cycle fatigue (HCF) where $10^3 < N_f < 10^6$ cycles [49]. The cyclic stresses in this approach are described using the maximum stress (σ_{max}), the minimum stress (σ_{min}), the stress amplitude ($\sigma_a = \frac{\sigma_{max} - \sigma_{min}}{2}$), the mean stress

($\sigma_m = \frac{\sigma_{max}+\sigma_{min}}{2}$) and the load ratio (R=$\frac{\sigma_{max}}{\sigma_{min}}$) [47, 50]. Several load waveforms are used to repeatedly apply the fatigue stress to the specimen. While triangular and square waveforms are also utilized, the loading wave's typical shape is sinusoidal [45] (see Figure 2.21). Although the stress amplitude may be varied, practical applications and many fatigue tests on materials involve cycling between a constant stress amplitude level [29, 46, 47] as shown in Figure 2.21.

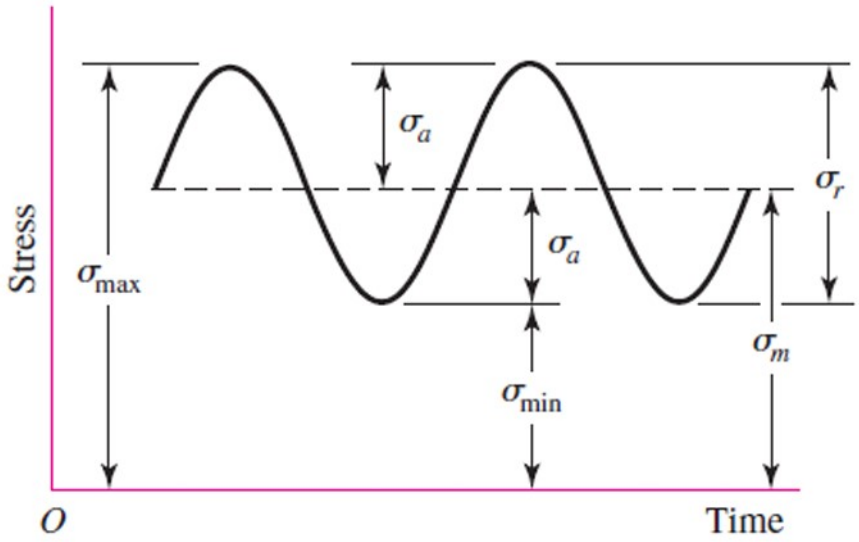

Figure 2.21: *Typical Sinusoidal Waveform describing fatigue testing parameters [50]*

Under this approach, plotting the stress amplitude with the corresponding fatigue life obtained from testing, yields the S-N curve which is a visual representation of the materials behaviour under cyclic loading [29, 46]. Depending on the load ratio chosen, the fatigue tests performed using the S-N approach may be performed with our without mean stress present. When the tests are performed with mean stress present (R≠-1), mean stress correction methods must be applied to account for it as the effects of mean stress on fatigue life has been sufficiently studied [29, 46, 48–52].

There are several models used to correct for the mean stress such as the Walker, the Smith Watson Topper method, Goodman and Morrow correction models [53]. Once a mean stress correction method has been applied, an equivalent fully reversed (R=-1) S-N curve can be obtained which can be modeled using the Basquin model [29, 46] given in Equation 2.4 that fits the curve to a straight line in a log-log plot [29]. The specimen geometry, testing methods and procedures for the stress-based approach to fatigue testing are outlined in the standards ASTM E466 [54].

$$\sigma_a = \sigma_f^{'}(2N_f)^b \tag{2.4}$$

where $\sigma_f^{'}$ and b are the material parameters.

2. **Strain-based Approach**: Also called the strain-life (E-N) approach, this method involves a more detailed analysis of the localized yielding that may occur at stress raisers during cyclic loading [29,46]. This method is often applied for low cycle fatigue where $N_f < 10^3$ cycles and significant plastic deformation is present but may also be applied in the high cycle fatigue regime which makes it more comprehensive than the stress-based approach [29, 46, 55]. This approach is described by the strain amplitude (ϵ_a) and plotting the strain amplitude with the corresponding stress amplitudes yields a cyclic stress-strain curve which is quite different from the stress-strain curve obtained by quasi-static tensile testing [29, 46, 51]. Under cyclic loading, the material may display either cyclic hardening or softening, a phenomenon termed the Bauschinger effect [29, 46, 56, 57]. Thus, one single reversal of inelastic strain can change the stress-strain behavior of metals. Cyclic hardening indicates an increased resistance to deformation while cyclic softening indicates a decreased resistance to deformation under

cyclic loading [29,46,56]. These changes in deformation behaviour are more pronounced at the beginning of cyclic loading before the material stabilizes with continued cyclic loading [29, 46]. Plotting the strain amplitude against the corresponding fatigue life yields the E-N curve which can be modeled using the Coffin-Manson equation [29,46,48] given in Equation 2.5. Like the S-N approach, when the E-N test is run with mean stress present, modified versions of the models presented previously are applied to correct for its effects [29, 46, 48]. The specimen geometry, testing methods and procedures for the strain-based approach to fatigue testing are outlined in the standards ASTM E606 [58]

$$\epsilon_a = \frac{\sigma_f^{'}}{E}(2N_f)^b + \epsilon_f^{'}(2N_f)^c \tag{2.5}$$

where $\sigma_f^{'}, \epsilon_f^{'}$, b and c are the material parameters.

An approach similar to the strain-life method based on strain energy has also received great attention [59–64]. The driving force of fatigue in this approach is the product of stress and strain tensors, i.e. strain energy density [62–64]

2.4.2 *Fatigue Properties of Non-Oriented Electrical Steel Sheets*

The fatigue life of non-oriented electrical steel has been reported by Lakkonavar et al. [2] and Bode et al. [19]. Both authors investigated the effect polishing has on the fatigue life when compared to punched specimens [2, 19]. While Bode et al. [19] performed cyclic tests on specimens with polished edges originally cut using high precision spark erosion as well as specimens cut from an existing rotor sheet normally obtained by punching, Lakkonavar et al. [2] performed cyclic tests on punched specimens with a select group having polished edges. Both authors concluded that polishing significantly increased the fatigue life of the

specimens especially in the high cycle regime ($> 10^5$ cycles) [2, 19]. Figure. 2.22 shows the stress life curve of the tests performed by Lakkonavar et al. [2]. Fortese et al. [65] also reported that the high cycle fatigue behaviour of thin non-oriented electrical sheet is strongly affected by the extraction method and that simply polishing the specimens can improve the fatigue life by as much as 30% over as-punched specimens.

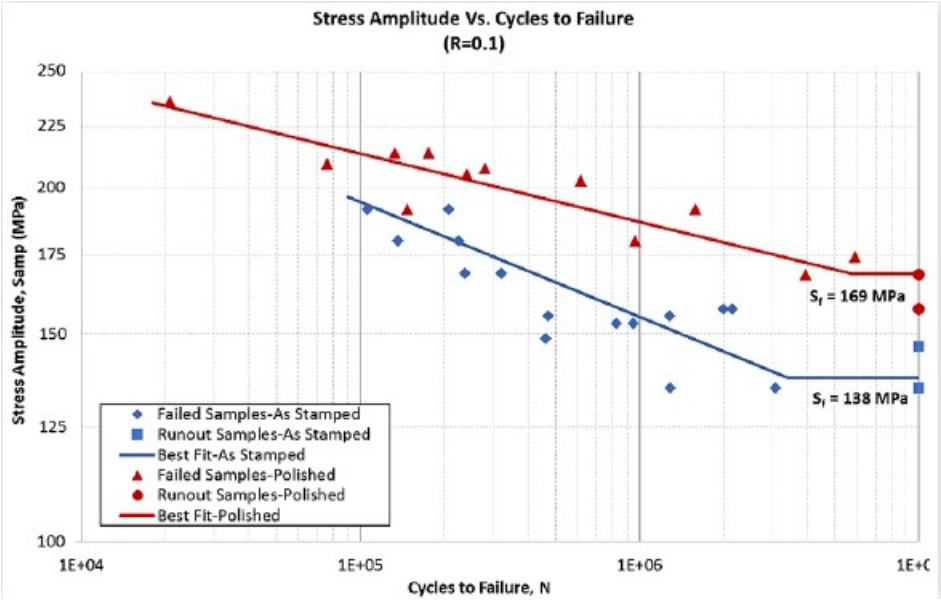

Figure 2.22: *Stress amplitude vs. cycles to failure of as-stamped and polished samples [2]*

The fracture mechanism for fatigue testing was cleavage fracture with the crack initiating from micro-notches shown in Figure 2.23a [19]. The majority of the micro-notches were shallow notches shown in Figure 2.23b introduced by plastic deformation during the manufacturing process.The authors [19] observed that although these shallow notches were rounded and should have less stress concentration factors, they were more likely to cause fatigue fracture because of the plastic deformation reducing the deformation resistance of these shallow notches. Other crack initiation sites included angular holes from dislodged particles during testing. Similarly, Liying et al. [66] reported that the preferred sites for crack initiation

included surface grain boundary, crystal grains and inclusion. Irrespective of the crack initiation site, Bode et al [19] and Liying et al. [66] reported that the crack is propagated by stable crack extension and fails transgranularly along the cleavage facets.

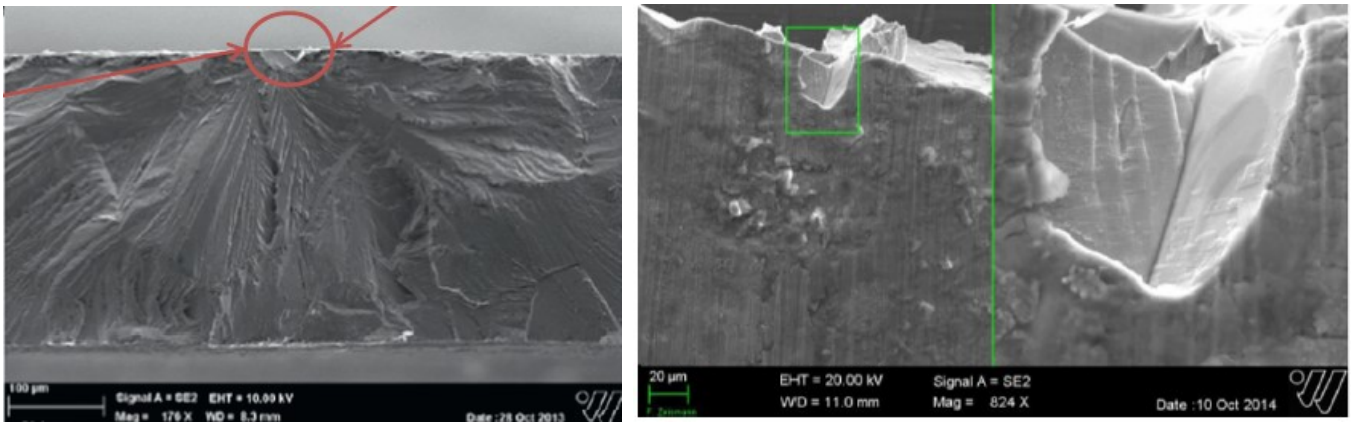

(a) Fracture surface highlighting a micro-notch that initiated the crack [19]

(b) Shallow notches from manufacturing processes [19]

Figure 2.23: *SEM image of fatigue crack surface and crack initiation site [19]*

Chapter 3

Methodology

3.1 Microstructure and Texture Analysis

The microstructural study was performed on three grades of non-oriented electrical steel sheets namely: 27PNX1350F, 25SW1250 and 20SW1200 were studied with nominal thicknesses of 0.27mm, 0.25mm and 0.20mm respectively. The 27PNX1350F grade was the main material being studied while the other grades were studied for the purpose of comparison and as such, while a more detailed microstructural analysis was performed on the 27PNX1350F grade, a very limited microstructural analysis was performed on the other two grades.

3.1.1 *Specimen Extraction*

For the microstructural and texture analysis, small rectangular samples were extracted from the three grades of non-oriented electrical steel sheets in the rolling and transverse directions, grinded up to 600 grit, polished, and etched with nitric acid to prepare them for analysis.

3.1.2 *Experimental Details*

To identify the grain size and distribution for the 27PNX1350F grade, a Zeiss Inverted Optical Microscope (OM) with INFINITY2-3 (3.3 Megapixel) was used and the images captured at 200x magnification while the chemical composition and precipitate characterization was performed using the Zeiss LEO 1530 Field Emission Scanning Electron Microscope (FE-SEM) with Energy Dispersive X-ray Sepctroscopy (EDX) equipped and operated at 20kV. The average grain size was calculated according to ASTM E112-13 [67] which provides the standard test methods for measuring grain size. A Thermo Scientific Quattro FE-SEM equipped with a Thermo Scientific Lumis Electron BackScatter DIffraction (EBSD) system was used for texture analysis and phase identification. For the 25SW1250 and 20SW1200 grades, the grain size and distribution were identified using the Zeiss LEO 1530 FE-SEM.

3.2 Quasi-Static Tensile Tests

The tensile properties of three grades of non-oriented electrical steel sheets namely: 27PNX1350F, 25SW1250 and 20SW1200 with nominal thicknesses of 0.27mm, 0.25mm and 0.20mm respectively at room temperature and an elevated temperature of 150°C were studied.

3.2.1 *Specimen Extraction*

The specimen geometry for the tensile test was designed according to ASTM E8 [33] and is shown in Figure 3.1. Three specimens each were cut along the rolling direction, transverse direction and at a 45° orientation to categorize the tensile properties in each direction. The 27PNX1350F specimens were cut from the steel sheets using water-jet cutting method

while the other two grades were cut using the computer numerical control (CNC) machining method. The sheet matrix for specimen extraction is shown in Figure 3.2.

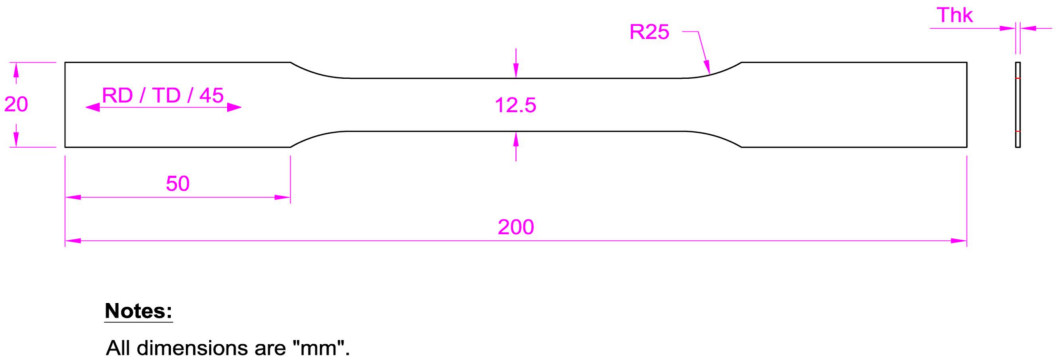

Figure 3.1: *Specimen Geometry for Tensile Testing*

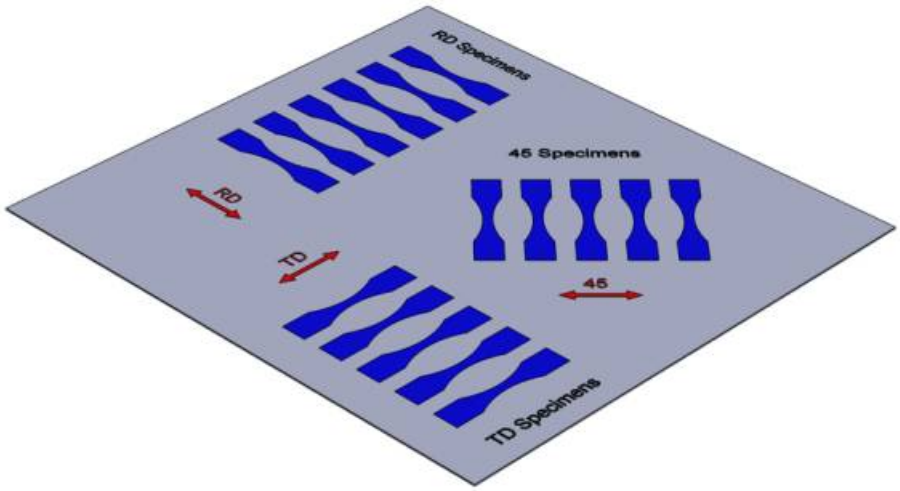

Figure 3.2: *Sheet Matrix for Specimen Extraction*

3.2.2 *Experimental Details*

The tensile tests at room temperature were carried out on the INSTRON 8874 axial-torsional test frame with a load and torque capacity of 25kN and 100N.m respectively while the tests at 150°C were carried out on the MTS 810 load frame with a load capacity of 50kN. The

elevated temperature tests were conducted in the Instron Environmental Chamber Model 3119-609 with a temperature range from -100°C to 350°C. The chamber heated the specimens by forced convection and as such, there was a temperature gradient of along the gauge length of the specimen. While the middle of the gauge section was heated to 150°C, the top and bottom had a difference of ±5°C respectively from the middle of the specimen. The temperature inside the environmental chamber was monitored and controlled by a Type-N thermocouple [68] while an infrared thermometer was used to measure the specimen temperature. The specimens for the tensile tests at both temperatures were loaded in axial tension and the tests were run in displacement controlled mode. According to ASTM E8 [33], the displacement rate was set to 1.2mm/min. For strain measurement, digital image correlation (DIC) technique was used and the specimens were speckled with black on white paint for this purpose with the GOM ARAMIS 3D 5MP with two high resolution CCD cameras and a frame rate of 15fps being the equipment used. Three sets of tests in the rolling direction, transverse direction and at a 45° orientation were performed for each grade of non-oriented electrical steel sheet and from the test data, the tensile properties and Ramberg-Osgood parameters for the different grades along the respective directions were extracted. After the tests were concluded, the fractured surface of the fractured specimens were analyzed. For the fractography analysis, samples 10cm long from the point of fracture were cut and analyzed using Zeiss LEO 1530 FE-SEM. Lastly, the stress-strain curves and tensile properties presented for both room and elevated temperature were normalized by the yield strength of the 27PNX1350F grade tested at room temperature along the rolling direction as requested by the project partners.

3.3 Fatigue Tests

The fatigue properties of three grades of non-oriented electrical steel sheets namely: 27PNX1350F, 25SW1250 and 20SW1200 with nominal thicknesses of 0.27mm, 0.25mm and 0.20mm respectively at room temperature were studied while only the fatigue properties of the 27PNX1350F grade was studied at an elevated temperature of 150°C.

3.3.1 *Specimen Extraction*

The specimen geometry for the cyclic test was designed according to ASTM E466 [54] and is shown in Figure 3.3. The cyclic test specimens were cut parallel to the rolling direction. The specimens were cut from the steel sheets using the computer numerical control (CNC) machining method. The sheet matrix is the same as given in Figure 3.2.

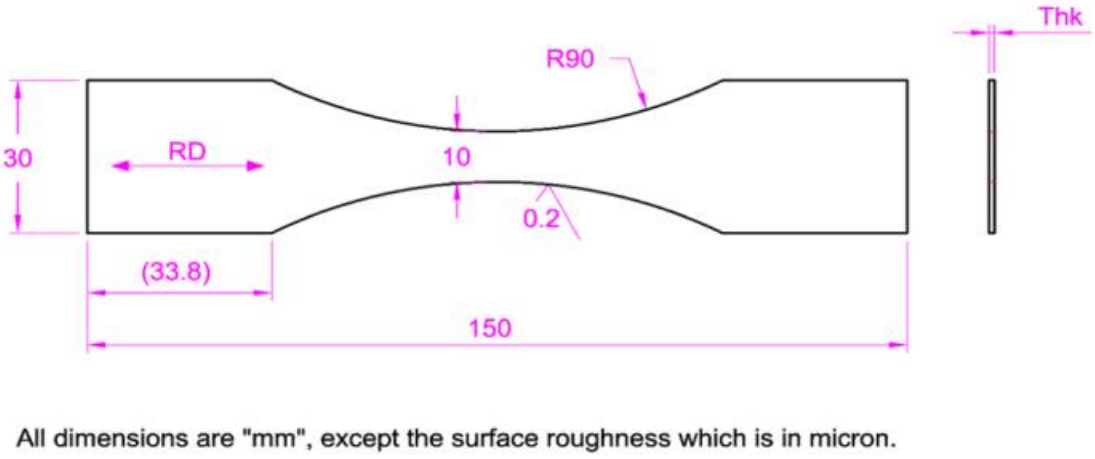

Figure 3.3: *Specimen Geometry for Fatigue Testing*

3.3.2 *Experimental Details*

The cyclic tests were performed according to ASTM E466 [54] on the MTS 810 test frame with a load capacity of 50kN for the 27PNX1350F specimens, the INSTRON 8872 axial test frame with a load capacity of 25kN for the 25SW1250 specimens and the INSTRON 8874 axial-torsional test frame with a load and torque capacity of 25kN and 100N.m respectively for the 20SW1200 specimens. The tests were run in load controlled mode and the frequency of the tests ranged from 0.1-20Hz. The tests at elevated temperature were run in the same INSTRON environmental chamber described in section 3.2. The specimens failed shortly after crack initiation and as such, the life at fracture was used as the failure life (N_f). To avoid buckling of the thin sheet specimens, the loading was done in axial tension with a load ratio of R=0.1 and a sinusoidal wave shape. For these set of tests, the run-out life was set to $2x10^6$ cycles.

To investigate the effect of cutting method and mean stress on the fatigue life, extra cyclic tests were performed on the 27PNX1350F grade of non-oriented electrical steel sheets. For these set of tests, the cutting method was changed to water-jet and digital image correlation technique was used to determine the 1mm crack initiation life in selected specimens which were painted with white paint to facilitate crack detection by DIC in which the correlated solution 3D 5MP with two high resolution CCD cameras and a frame rate of 13fps was the equipment used. However, the specimens failed shortly after crack initiation and as such, the life at fracture was used as the failure life (N_f). The tests were initially run at a load ratio of R=0.1 and to investigate the effect of mean stress, limited cyclic tests at load-ratios of R=0.3 and R=0.5 were performed at selected stress amplitudes.

The fractured surfaces of the fractured specimens were also analyzed using Zeiss LEO 1530 FE-SEM on samples 10cm long from the point of fracture. Lastly, the stress-life (S-N) curves and fatigue parameters presented were normalized by the yield strength of the 27PNX1350F grade tested at room temperature along the rolling direction as requested by the project partners.

Chapter 4

Microstructure of Non-Oriented Electrical Steel Sheets

The microstructure of electrical steel affects its bulk mechanical properties while its texture is the most important parameter that controls the magnetic properties. A study to identify microstructural properties such as the grain size and distribution, present phases, precipitates, chemical composition, and texture was performed on three different grades of electrical steel sheets with varying thickness. The results of this study are presented in this chapter.

4.1 Results and Discussion

4.1.1 *27PNX1350F*

The chemical composition of this grade of non-oriented electrical steel sheet was first confirmed. The major elements present are shown in Table.4.1. This grade was confirmed to have about

3% silicon content with little aluminium precipitates present. The precipitates present in the steel sheet were observed and confirmed using EDX. Figure 4.1 shows a micrograph of the non-oriented electrical steel sheet with precipitates and the elements present.

Table 4.1: Chemical Composition of 27PNX1350F

Element	**Al**	**C**	**Si**	**Fe**
Wt(%)	0.69	6.65	2.98	89.68

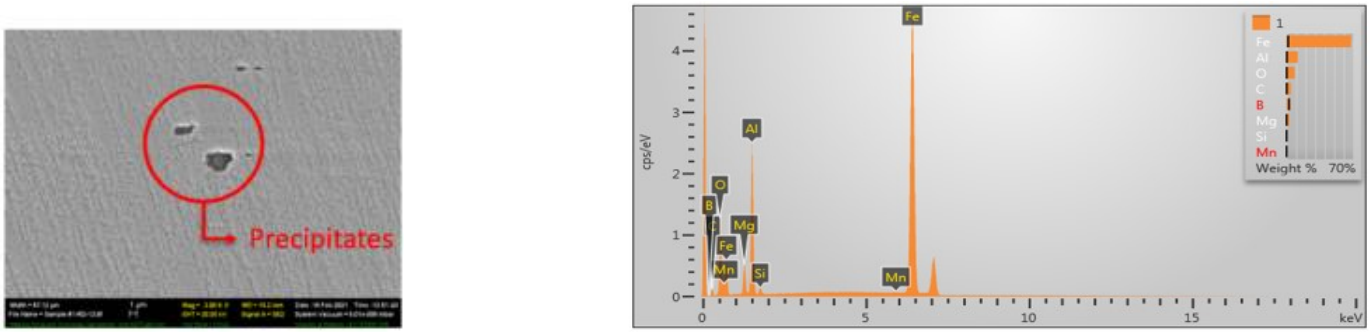

(a) (b)

Figure 4.1: *(a)Micrograph showing precipitates present in the matrix of the non-oriented electrical steel sheet. (b) EDX analysis showing the elements present in the precipitates*

Optical micrographs of the 27PNX1350F grade along the thickness direction are shown in Figures 4.2. The cross-section is characterized by few and relatively large polygonal grains with an average size of $72\mu m$ distributed across the thickness of the non-oriented electrical steel sheet. The distribution of grain sizes for the rolling and transverse directions are shown in the chart given in Figure 4.3. The grain size distribution chart here uses an equivalent diameter of a circle having the same area as the polygonal grain.

(a)

(b)

Figure 4.2: *Optical Micrograph of 27PNX1350F along (a) Rolling Direction (RD) (b) Transverse Direction (TD)*

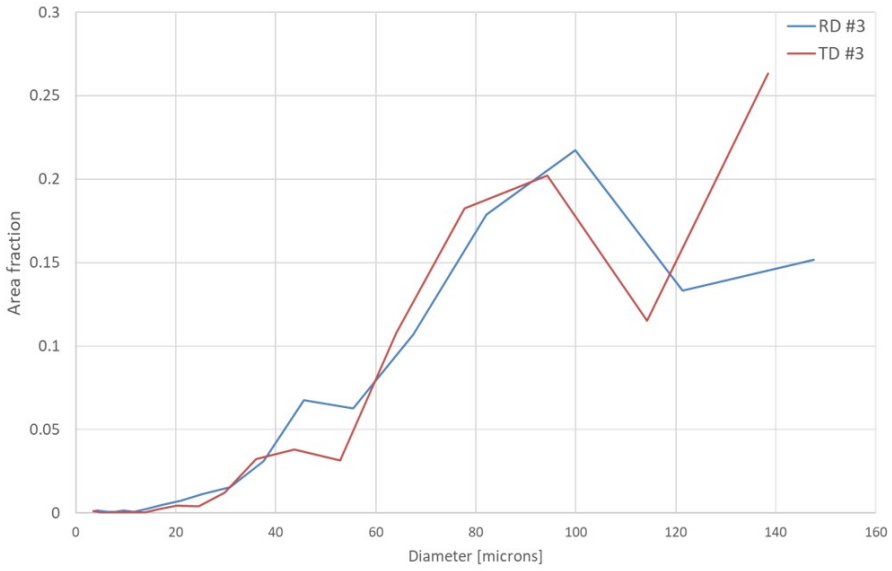

Figure 4.3: *Grain Size Distribution*

The orientation of the grains along the rolling and transverse directions were also extracted using EBSD and the results are displayed in Figure 4.4. The misorientation of the grains was also measured and the results are displayed in the chart given in Figure 4.5. From the figure, the presence of sub-grain boundaries was detected as the majority of the grain boundaries have a misorientation angle less than 15° and of that majority, most have a misorientation of about 2.5°which may represent an array of dislocations.

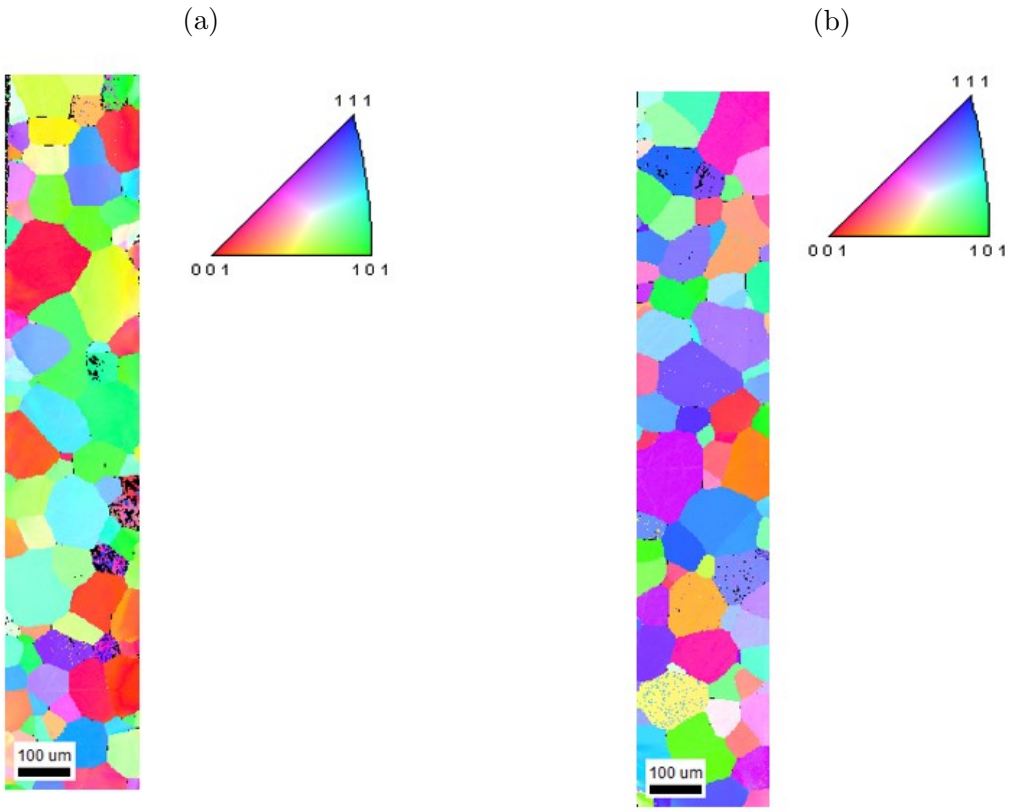

Figure 4.4: *Grain Orientation of 27PNX1350F along (a) Rolling Direction (RD) (b) Transverse Direction (TD)*

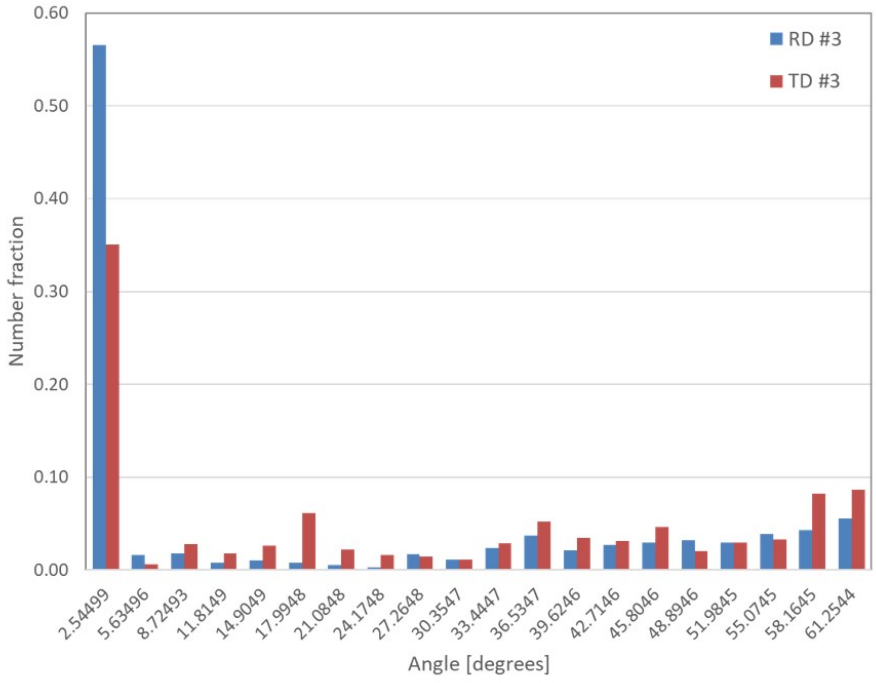

Figure 4.5: *Chart showing the misorientation of the grains relative to each other in the non-oriented electrical steel sheet*

The phases present in the non-oriented electrical steel sheet were also investigated and the results are presented in Figure 4.6. Although a very small percentage of face centered cubic (FCC) crystal structure was detected, the major phase present is ferrite with body centered cubic (BCC) crystal structure.

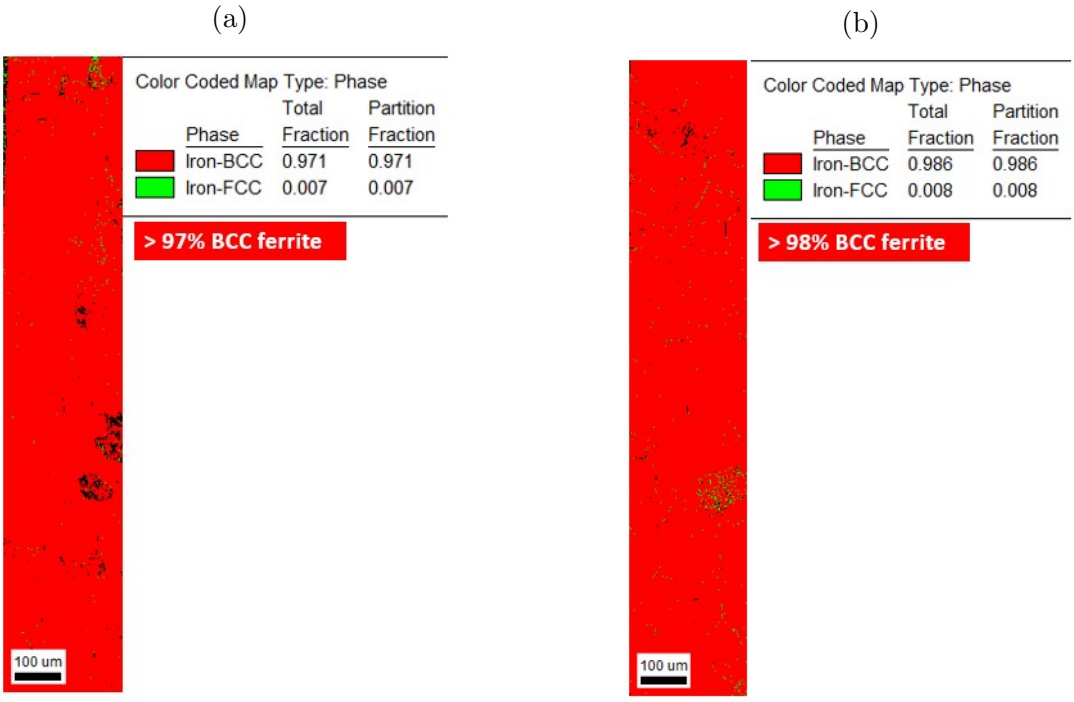

Figure 4.6: *Phase Identification of 27PNX1350F along (a) Rolling Direction (RD) (b) Transverse Direction (TD)*

Finally, to confirm the random distribution of grains expected in the non-oriented electrical steel sheet, the texture of the steel sheet was analyzed using EBSD and the results are presented in Figure 4.7.

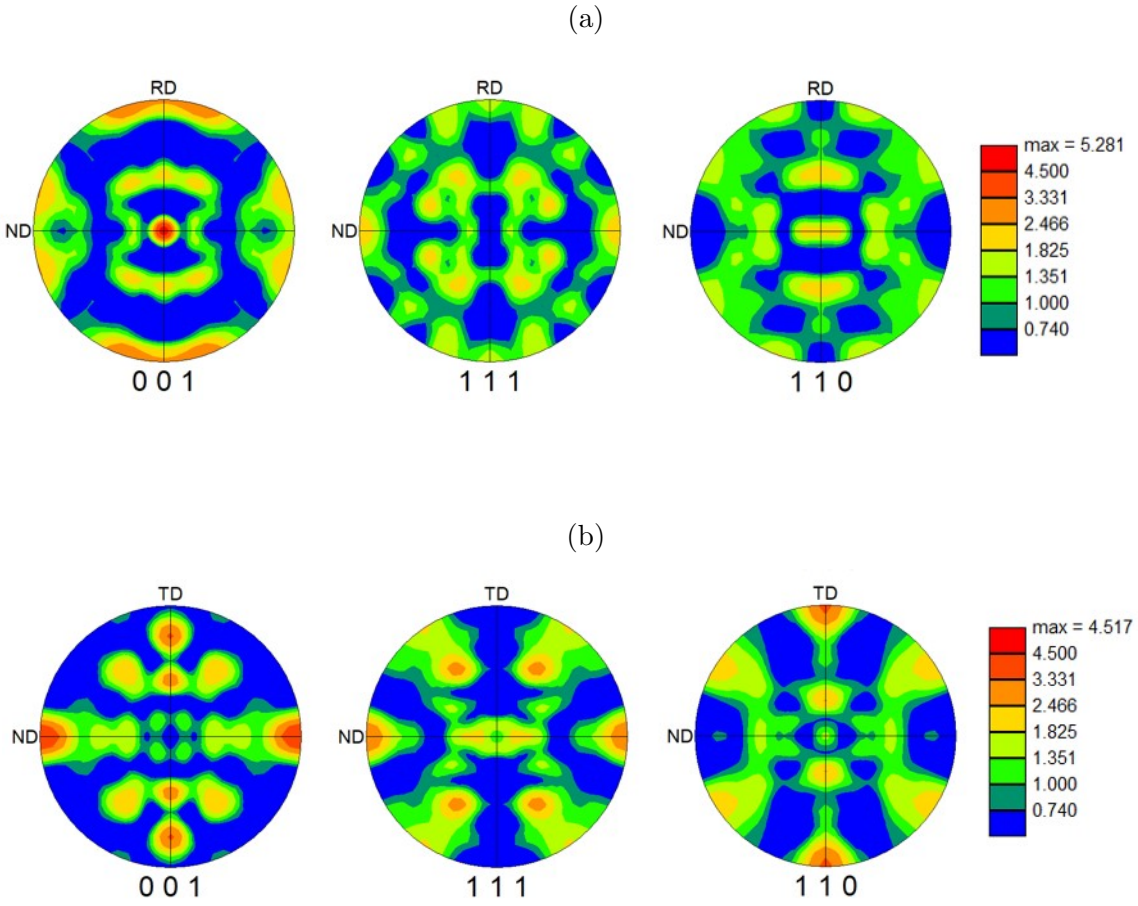

Figure 4.7: *Crystallographic texture of 27PNX1350F along (a) Rolling Direction (RD) (b) Transverse Direction (TD)*

4.1.2 *25SW1250*

For this grade of non-oriented electrical steel sheet, only the grain morphology was investigated. Figure 4.8 shows the SEM micrographs of the distribution and grain sizes along the rolling and transverse directions. Similar to the 27PNX1350F grade, the 25SW1250 grade also had few and relatively large polygonal grains with an average size of $105\mu m$ distributed across

the thickness of the sheet in both the rolling and transverse directions.

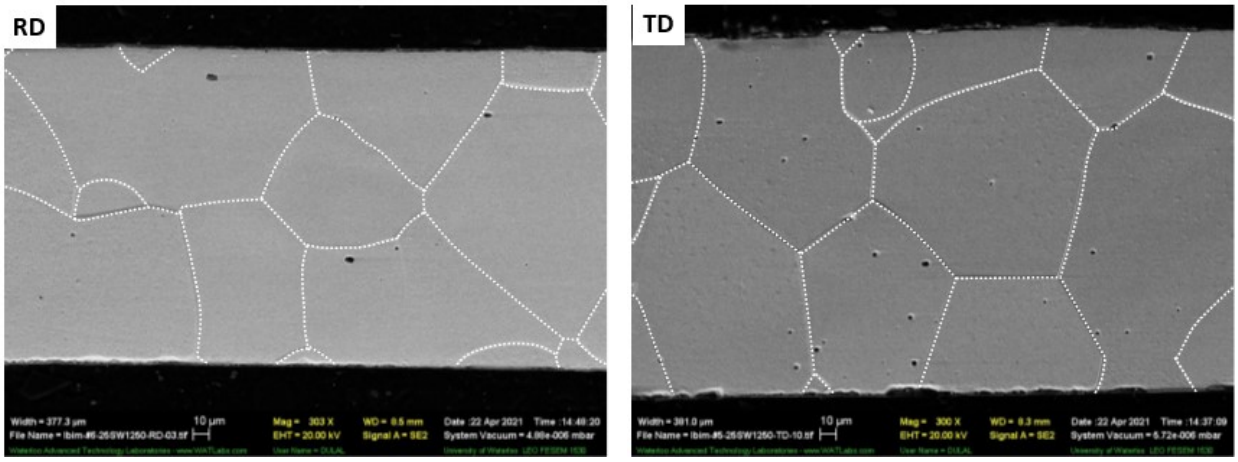

(a) (b)

Figure 4.8: *SEM Micrograph of 25SW1250 along (a) Rolling Direction (RD) (b) Transverse Direction (TD)*

4.1.3 *20SW1200*

Similarly, for this grade of non-oriented electrical steel sheet, only the grain morphology was investigated. Figure 4.9 shows the SEM micrographs of the distribution and grain sizes along the rolling and transverse directions. Similar to the previous two grades, the 20SW1200 grade also had few and relatively large polygonal grains with an average size of $68\mu m$ and $76\mu m$ distributed across the thickness of the sheet in the rolling and transverse directions respectively.

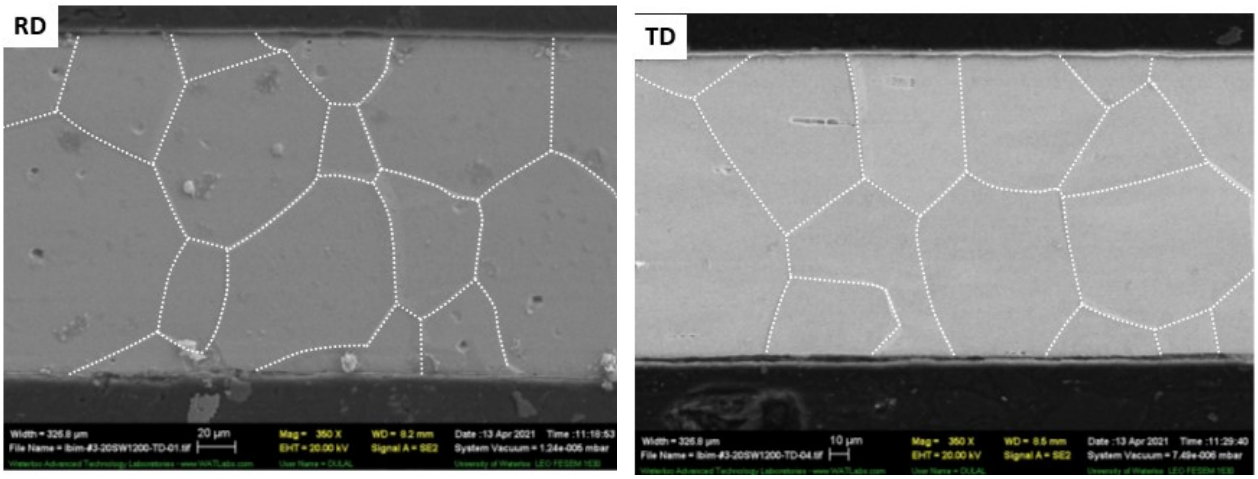

(a) (b)

Figure 4.9: *SEM Micrograph of 20SW1200 along (a) Rolling Direction (RD) (b) Transverse Direction (TD)*

4.1.4 Discussion

From Table 4.1, the electrical steel sheet has about 3% silicon content and from the Fe-Si binary phase diagram shown in Figure 2.5, it would be expected to have a body centered cubic (BCC) crystal structure [4]. This crystal structure was confirmed as shown in Figure 4.6. The grain morphology and distribution was similar for all three grades of non-oriented electrical steel sheets observed. They all had few and relatively large polygonal grains distributed across the thickness of the sheets. A comparison on the average grain size among the three grades is shown in Figure 4.10. From the figure, the 25SW1250 grade of non-oriented electrical steel sheet had the largest average grain size along both the rolling and transverse directions. The Hall-Petch relation [21] which correlates the grain size to the strength of materials would suggest that with the presence and distribution of these large grains, these steel sheets should be expected to have lower strength values than that of typical

structural steel which was confirmed in the tests performed on similar grades [2,3,19]. From

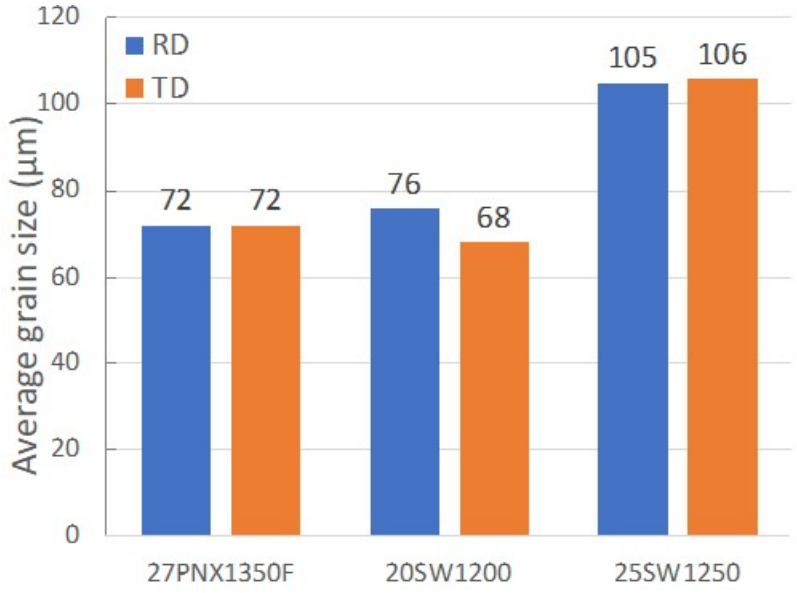

Figure 4.10: *Average Grain Size Comparison among the Three Grades of Non-Oriented Electrical Steel*

the orientation analysis shown in Figure 4.4, the image shows that the grains are randomly oriented and do not orient towards any particular direction. This is also confirmed by the texture analysis presented in Figure 4.7. The presence of precipitates in the steel matrix was also confirmed. Other than steel and silicon, the precipitate with the highest content was found to be aluminium. This was expected as aluminium nitrate precipitates have been confirmed present by other authors who investigated the microstructural properties of electrical steel [4, 19].

4.2 Chapter Conclusion

This chapter investigated the microstructural properties of three grades of non-oriented electrical steel sheets with different thicknesses. The following conclusions can be drawn from this investigation.

- The microstructure of these thin sheets are characterized by the distribution of few and relatively large polygonal grains on the same order of magnitude as the thickness across the sheet thickness.
- The crystal structure of the sheets is body centered cubic.
- The grains are randomly oriented and do not favour any particular direction in terms of its texture.
- Aluminium nitride precipitates are most likely present in the matrix of these steel sheets.

Chapter 5

Tensile Properties of Non-Oriented Electrical Steel Sheets at Room Temperature

Quasi-static tensile tests were conducted on non-oriented electrical steel sheets at room temperature to categorize their tensile properties at the aforementioned temperature. After the tensile tests were completed, the fracture surfaces were studied to characterize the deformation and fracture mechanisms present under this loading condition. The results of this study are presented in this chapter.

5.1 Results and Discussion

5.1.1 27PNX1350F

Tensile Properties

The normalized engineering and true stress-strain curves along all three directions are given in Figure 5.1. The true stress (σ_T) and strain (ϵ_T) were calculated from the engineering stress (σ) and strain (ϵ) by the relationships given in Equations 2.1 and 2.2 respectively. The normalized tensile properties are also presented in Table 5.1 and were calculated using the data collected from the tests performed in each direction. The elastic modulus (E) and yield strength (YS) were both calculated from the linear portion of the engineering stress-strain curve shown in Figure 5.1a. While the elastic modulus (E) was calculated as the slope of the linear portion, the yield strength (YS) was estimated using a 0.2% strain offset method [29]. The engineering and true ultimate strengths were the largest recorded values of stress from the engineering and true stress-strain curves respectively. Finally, the fracture strain was calculated as the final strain at fracture of the specimen and the reduction in area was calculated as the percent difference between the initial area before and the final area after fracture of the specimen. The strength coefficient (H) and strain hardening exponent (n) given in Table 5.1 are parameters from the Ramberg-Osgood relation (given in Equation 2.3) used to model the plastic region of the true-stress strain curve up to the true ultimate tensile strength.

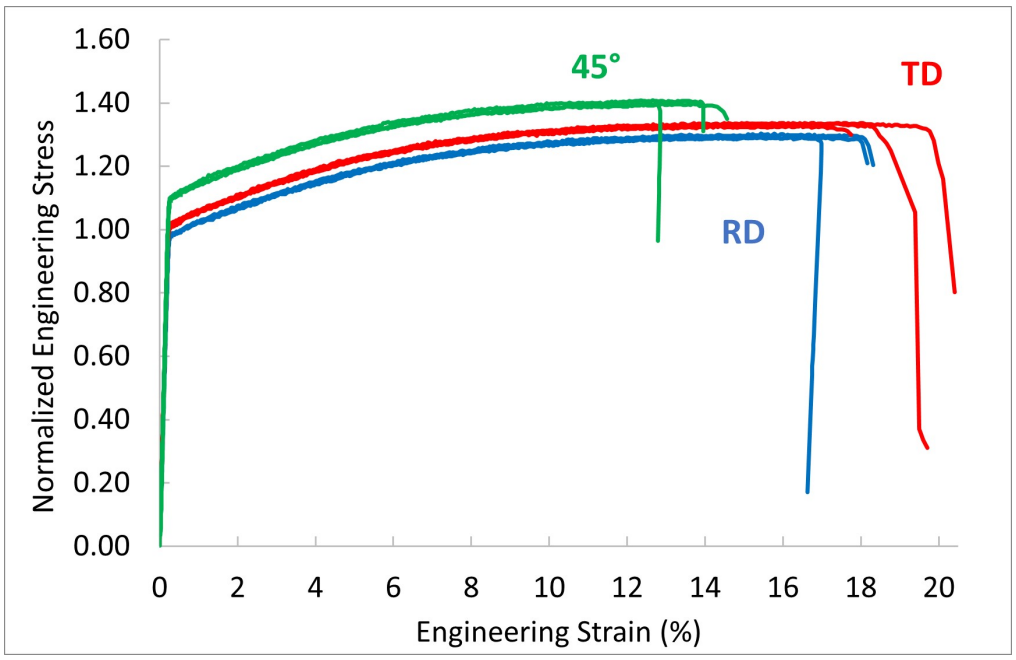

(a)

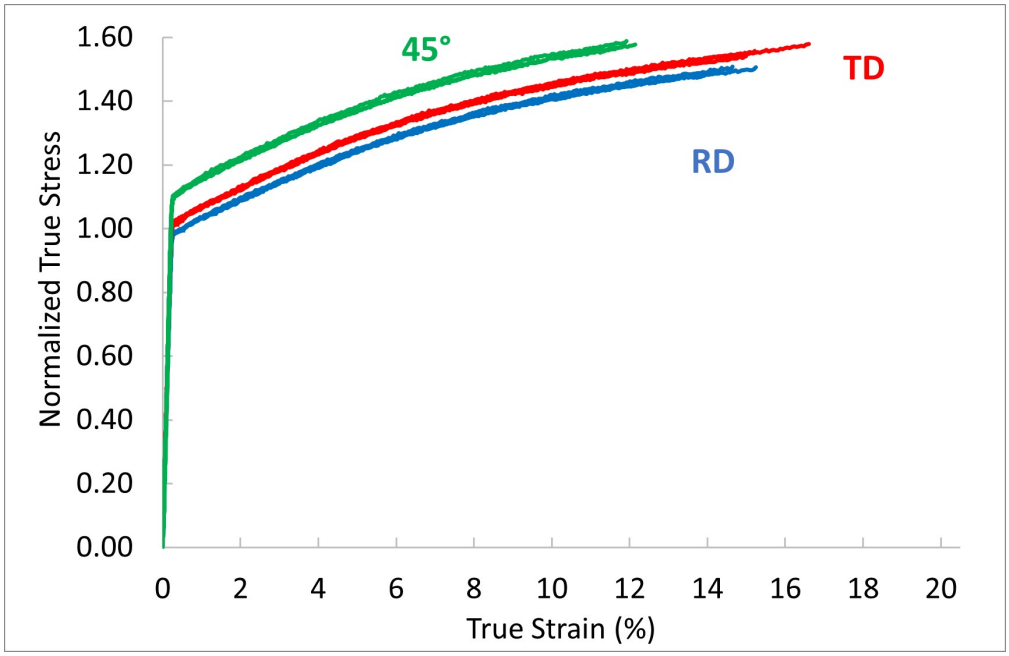

(b)

Figure 5.1: *Normalized stress-strain curves for 27PNX1350F (a) Engineering (b) True*

Table 5.1: Normalized Mechanical Properties of 27PNX1350F along the Different Directions

Mechanical	**RD**		**45°**		**TD**	
Properties	**Avg.**	**Std Dev.**	**Avg.**	**Std Dev.**	**Avg.**	**Std Dev.**
Elastic Modulus	432.28	1.93	492.72	1.23	470.42	3.79
Yield Strength	1.00	1.23	1.11	0.004	1.03	0.003
Engineering Ultimate Strength	1.30	0.01	1.40	0.01	1.34	0.004
True Ultimate Strength	1.50	0.01	1.58	0.01	1.56	0.02
Fracture Strain [%]	18	1	14	1	19	1
Reduction in Area [%]	8	0	4	0	10	0
Strength Coefficient, H	1.95	0.01	2.04	0.01	2.01	0.01
Strain Hardening exponent, n	0.14	0.00	0.12	0.00	0.14	0.00

The strain distribution along the gauge length of the samples were extracted from the DIC images and rather than being concentrated in a single region, the strain during plastic deformation was distributed in shear bands along the gauge section. This was also observed in the tests performed by Bode et al. [19]. Images showing the strain distribution for the three directions for one test are shown in Figure 5.2

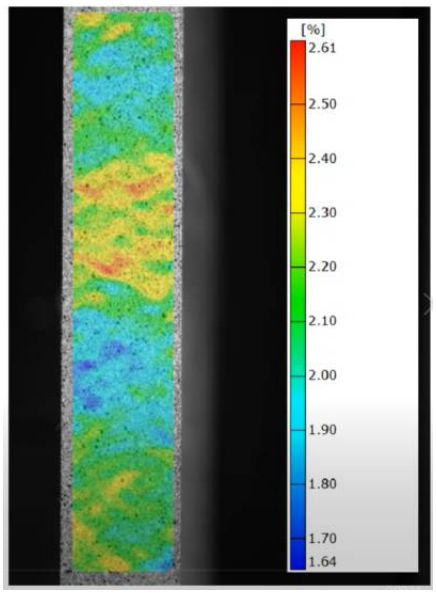

(a)

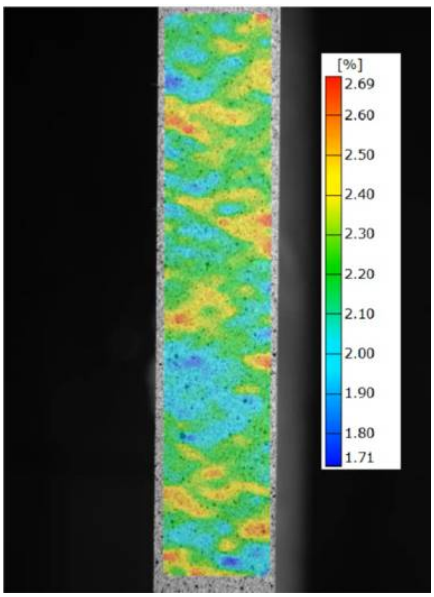

(b)

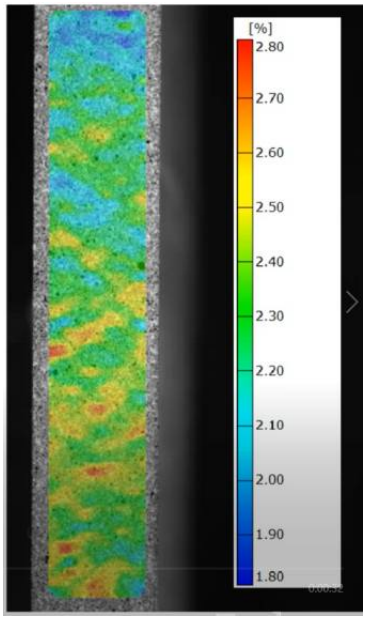

(c)

Figure 5.2: *Strain Distribution for 27PNX1350F specimens along the (a) Rolling Direction (b)45° Orientation (c)Transverse Direction*

Fracture Analysis

The specimens along all three directions fractured at an angle of about 45° to the loading direction (see Figure 5.3). The fracture at an angle is indicative of a ductile mode of fracture although no visible signs of necking were confirmed on the specimens as seen in Figure 5.3. As stated previously, during the plastic deformation of the specimens, the strain was distributed in shear bands across the gauge length of the specimen. However, right before fracture, the strain distribution localizes and concentrates around the plane of fracture (see Figure 5.4).

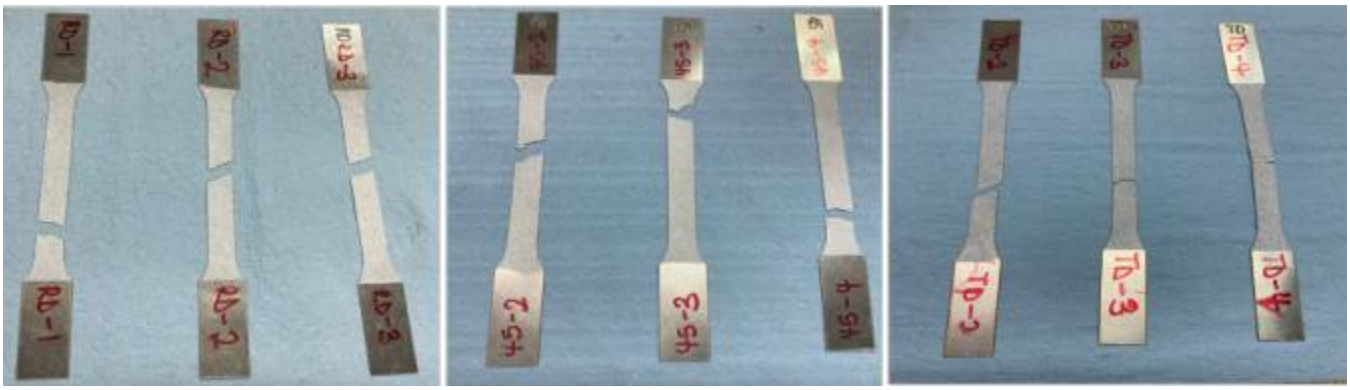

Figure 5.3: *Fractured 27PNX1350F specimens along the Rolling, 45° and Transverse Directions respectively*

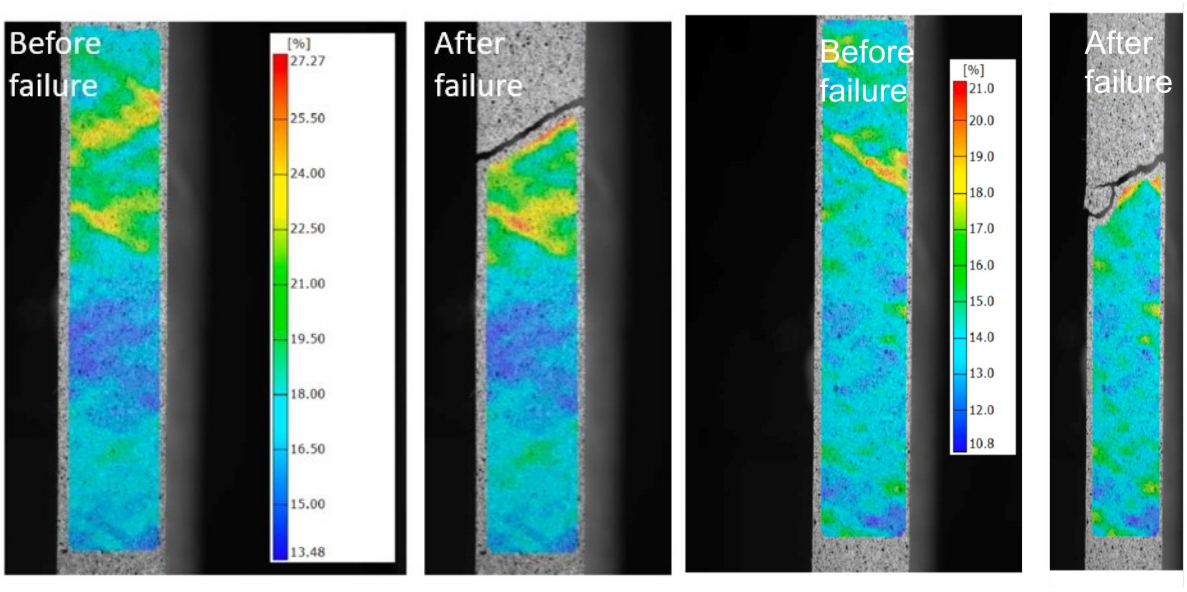

(a) (b)

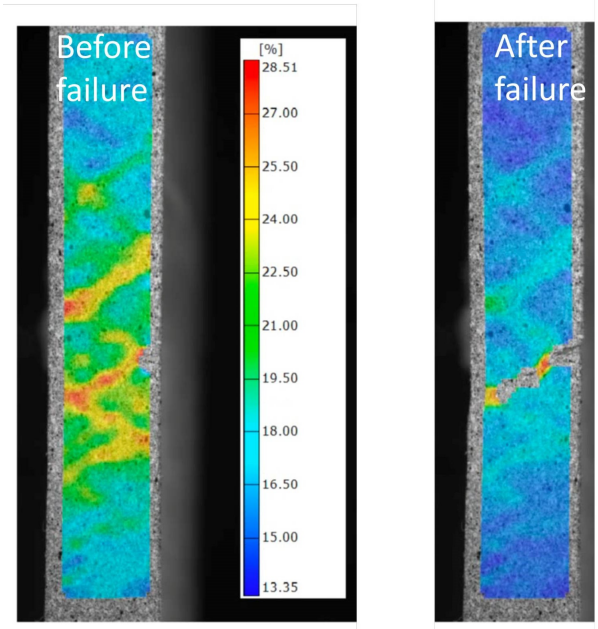

(c)

Figure 5.4: *Strain Distribution for 27PNX1350F specimens right before fracture along the (a) Rolling Direction (b)45° Orientation (c)Transverse Direction*

The fracture surfaces for specimens oriented along the rolling and transverse directions showed very similar features. Significant straining was observed on the fracture surfaces evidenced by the presence of shear bands as well as a severe thinning (significant reduction in thickness) of the fractured specimens that was localized to the region of fracture (see Figure 5.5). Also from Figure 5.5, the crack propagated along and fractured between the grain boundaries after significant straining of the grains (intergranular fracture mechanism).

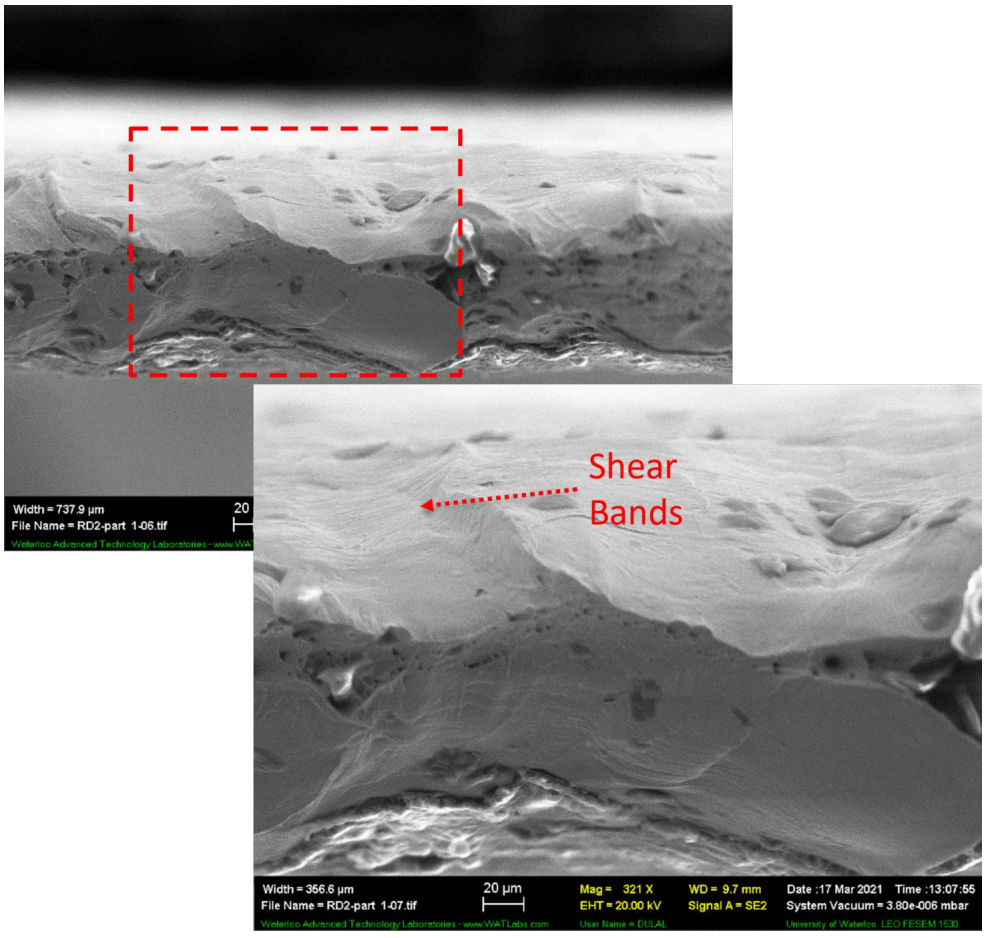

Figure 5.5: *Typical fracture surface for specimens along the Rolling and Transverse Directions*

While the RD and TD mainly showed a ductile type of failure, the fracture surface for the specimens oriented along 45° was mixed with signs of both ductile and cleavage fracture present. After crack initiation, the crack propagated in a ductile manner and then failed suddenly. Hence, the fracture surface of specimens oriented along 45° was divided into two regions: a ductile and brittle region (see Figure. 5.6). The brittle region showed little to no local necking and thickness reduction that was seen in the ductile region. It displayed a transgranular type cleavage fracture where the fracture propagated through the grains rather than along the grain boundaries. Furthermore, the microstructure surrounding the fracture surface was inspected and deformation twins (see Figure. 5.7) as well as slip bands originating from triple point junctions (see Figure. 5.8) which are mechanisms of accommodating plastic deformation were confirmed to be present.

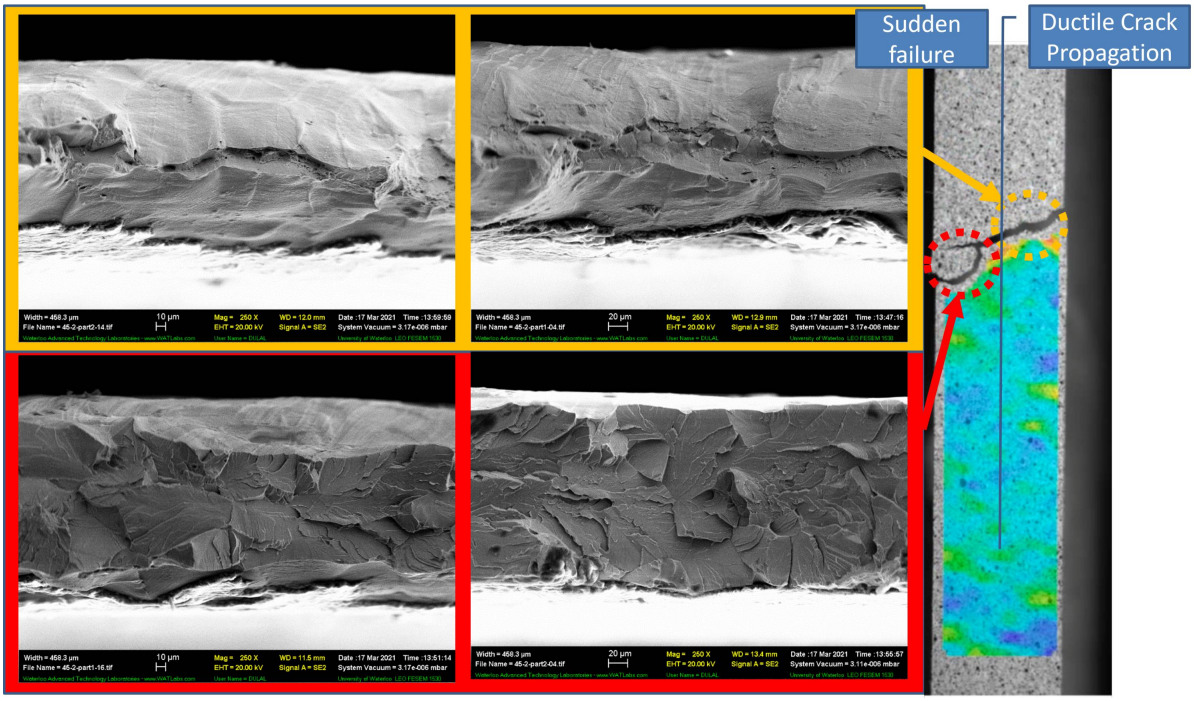

Figure 5.6: *Fracture surface of specimens oriented in 45° showing its features*

Figure 5.7: *Typical microstructure surrounding the fracture surface of specimens oriented along RD and TD showing mechanisms of accomodating plastic deformation*

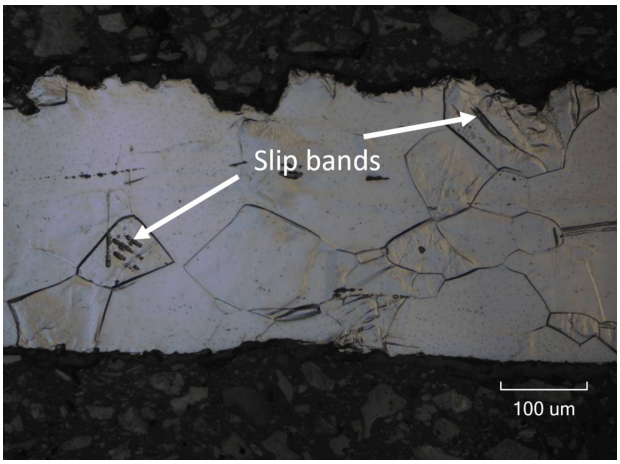

(a)

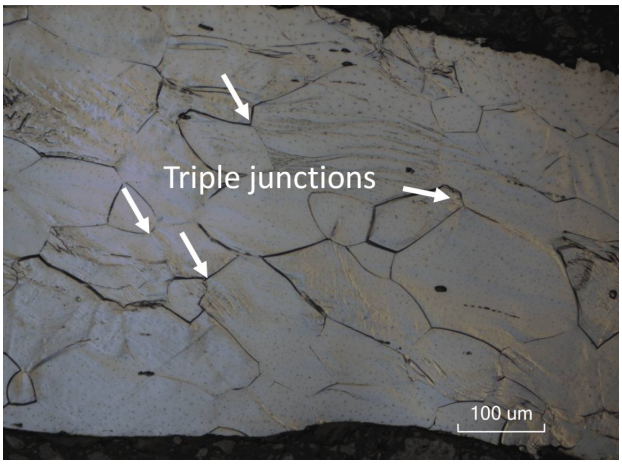

(b)

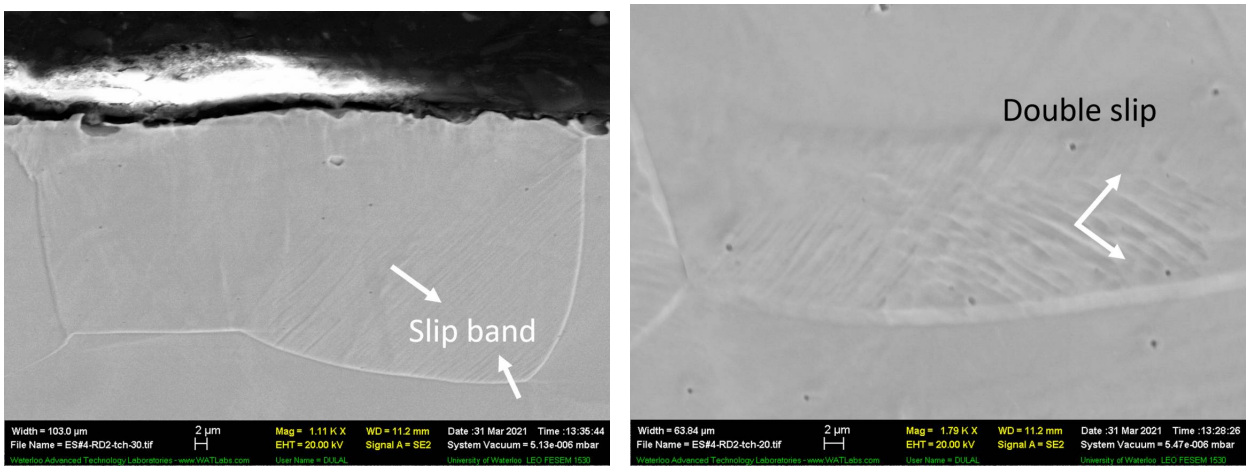

(c) (d)

Figure 5.8: *Typical microstructure surrounding the fracture surface of specimens oriented in RD and TD showing slip band deformation features*

5.1.2 25SW1250

Tensile Properties

The normalized engineering and true stress-strain curves along all three directions are given in Figure 5.9 and the normalized tensile properties are also presented in Table 5.2 which were calculated using the data collected from the tests performed in each direction. The relationship between the true stress and strain and engineering stress and strain remains the same as described above for the 27PNX1350F grade as does the methodology in extracting the tensile properties and parameters of the Ramberg-Osgood model. Similar to the 27PNX1350F grade, the strain during plastic deformation was distributed in shear bands along the gauge length of the specimen for specimens oriented along all three directions. Images showing the strain distribution for the three directions for one test are shown in Figure 5.10.

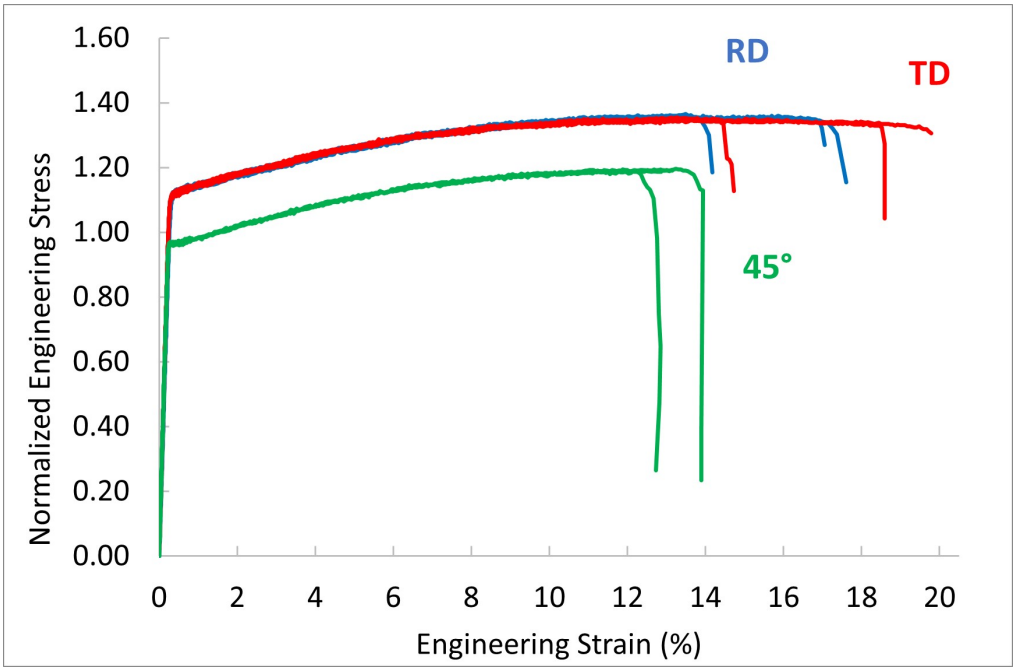

(a)

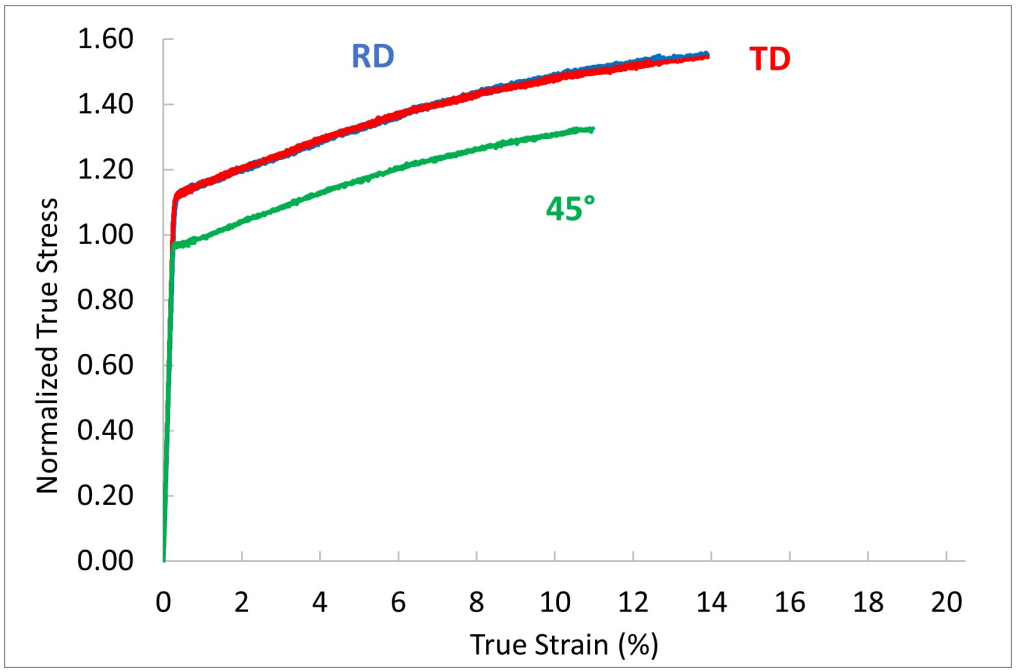

(b)

Figure 5.9: *Normalized stress-strain curves for 25SW1250 (a) Engineering (b) True*

Table 5.2: Normalized Mechanical Properties of 25SW1250 along the Different Directions

Mechanical	**RD**		**45°**		**TD**	
Properties	**Avg.**	**Std Dev.**	**Avg.**	**Std Dev.**	**Avg.**	**Std Dev.**
Elastic Modulus	389.92	2.24	418.15	1.73	426.43	2.40
Yield Strength	1.12	0.01	0.96	0.01	1.12	0.004
Engineering Ultimate Strength	1.36	0.004	1.19	0.004	1.35	0.004
True Ultimate Strength	1.55	0.01	1.33	0.02	1.54	0.01
Fracture Strain [%]	16	2	13	1	18	3
Reduction in Area [%]	5	1	7	0	11	2
Strength Coefficient, H	1.93	0.01	1.66	0.01	1.91	0.01
Strain Hardening exponent, n	0.12	0.00	0.11	0.01	0.11	0.00

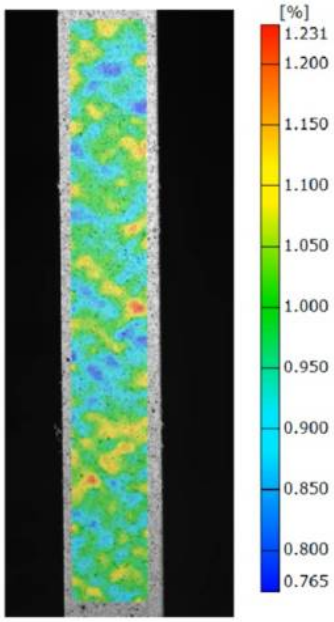

(a)

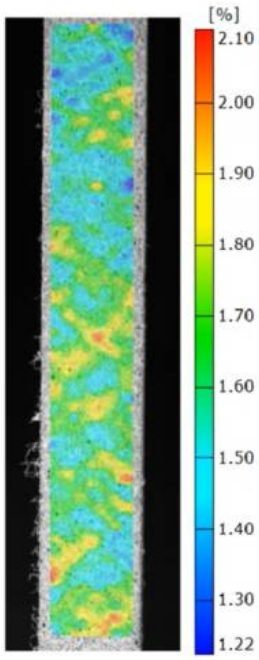

(b)

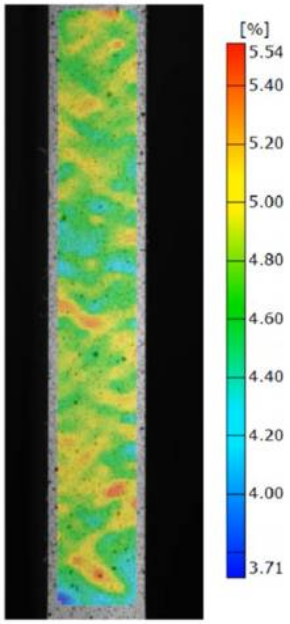

(c)

Figure 5.10: *Strain Distribution for 25SW1250 specimens along the (a) Rolling Direction (b)45° Orientation (c)Transverse Direction*

Fracture Analysis

The specimens oriented along all three directions fractured perpendicular to the loading direction (see Figure 5.11) which may be indicative of a more brittle mode of fracture. There were no visible signs of necking on the fractured specimens shown in Figure 5.11. Also, the shear bands across the length of the specimens resolved themselves along two planes and the crack initiated where these planes intersected as shown in Figure 5.12. From Figure 5.12, while the crack for the specimens oriented along the rolling direction and 45° orientation initiated at the edge of the specimens, the crack for specimens oriented along the transverse direction initiated within the specimen. Despite the difference in the location of crack initiation, the fracture surfaces showed similar features for all three directions. The fracture surfaces were characterized by an initial region of ductile deformation where thinning (described as "local necking" in Figure 5.14) of the sample occurred which was then followed by a region of brittle failure (see Figures 5.13, 5.14 and 5.15). Finally, upon studying the microstructure around the fracture region, the presence of deformation twins, micro-separation of the grain boundaries and transgranular cracks were confirmed (see Figure 5.16). These plastic deformation accommodation mechanisms and the transgranular nature of the cracks were confirmed to be present in all three directions. Figure 5.16 shows the typical microstructure around the fracture zone for all three directions.

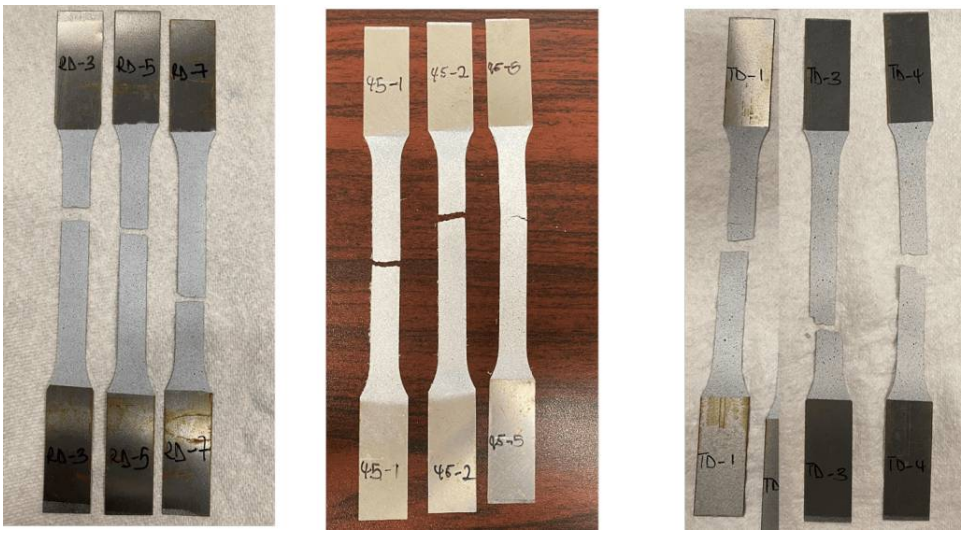

Figure 5.11: *Fractured 25SW1250 specimens along the Rolling, 45° and Transverse Directions respectively*

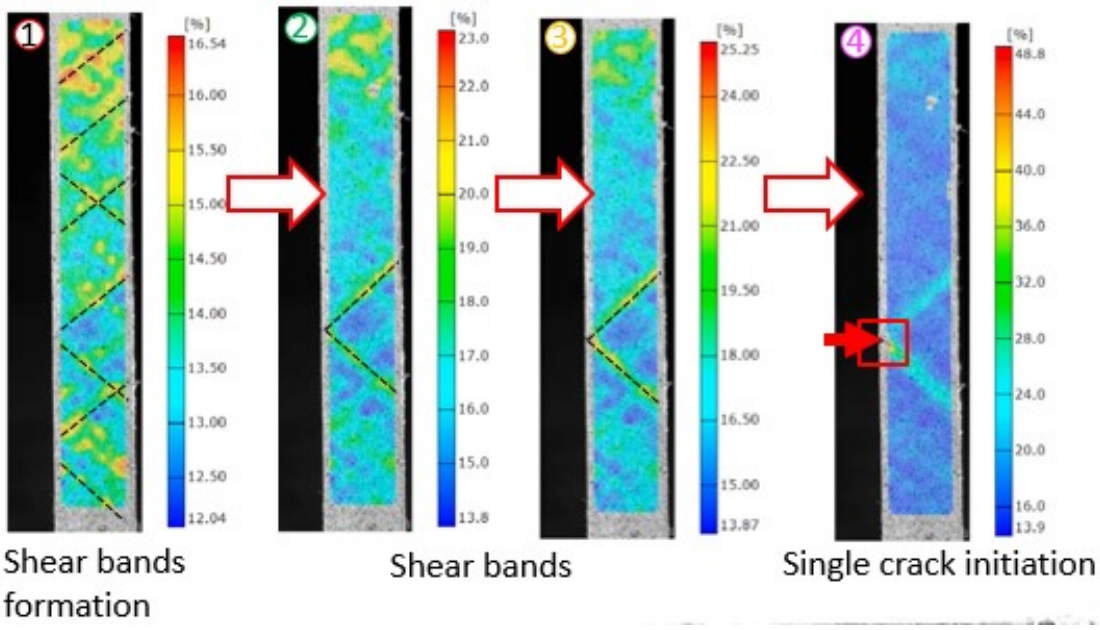

(a)

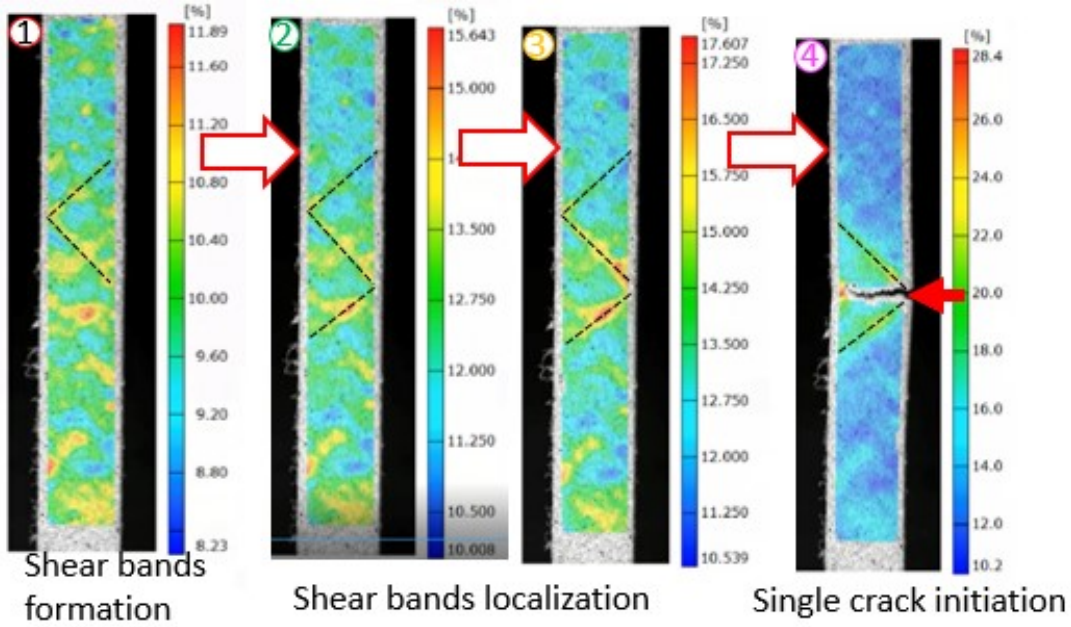

(b)

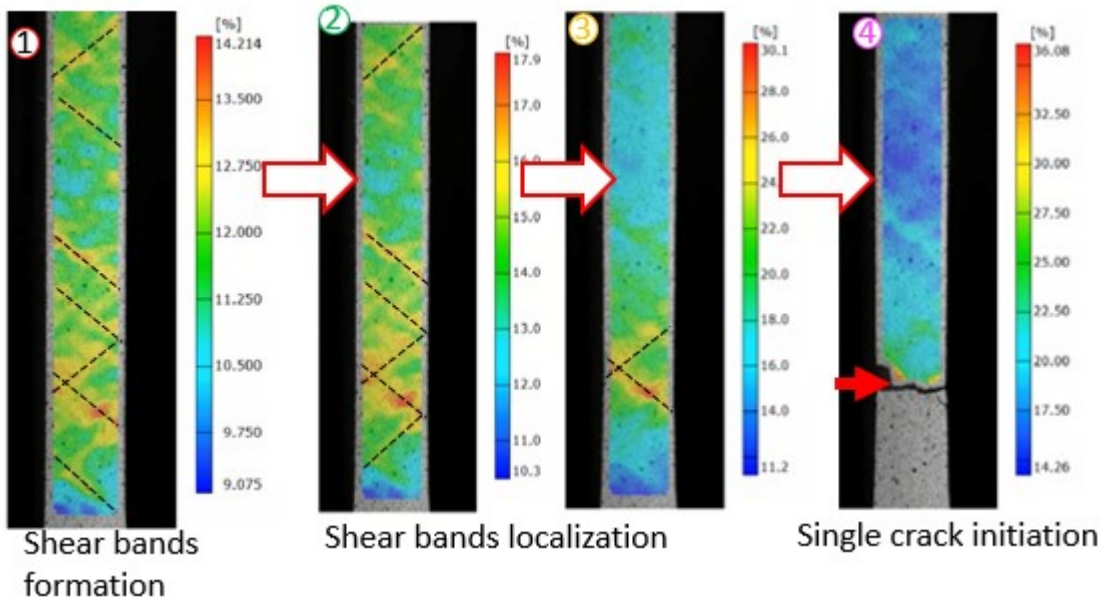

(c)

Figure 5.12: *Strain Distribution for 25SW1250 specimens right before fracture along the (a) Rolling Direction (b)45° Orientation (c)Transverse Direction*

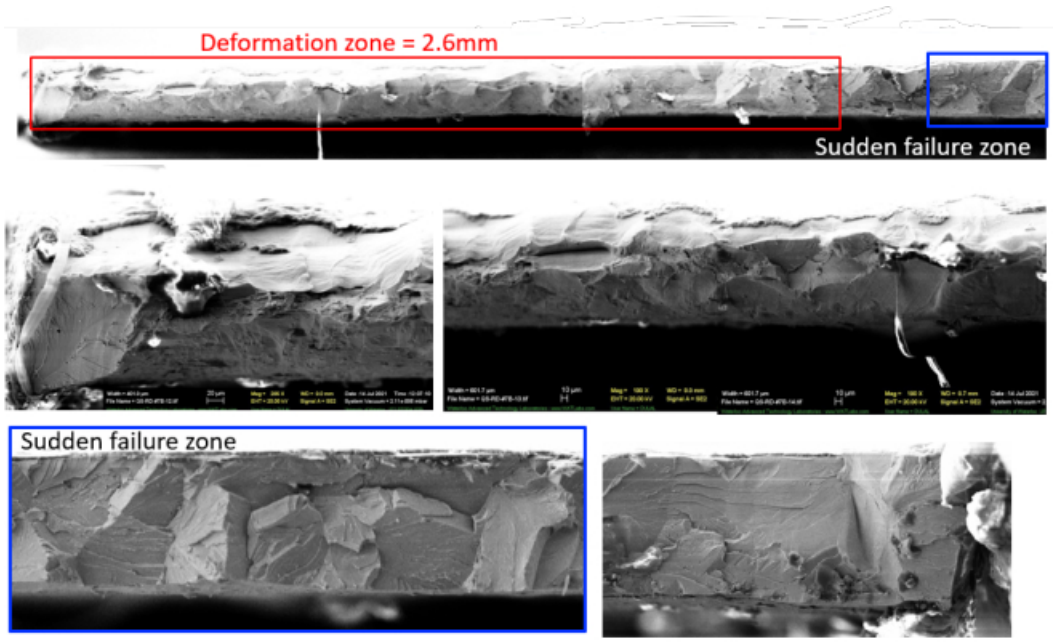

Figure 5.13: *SEM images of the typical fracture surface for specimens oriented along the rolling direction*

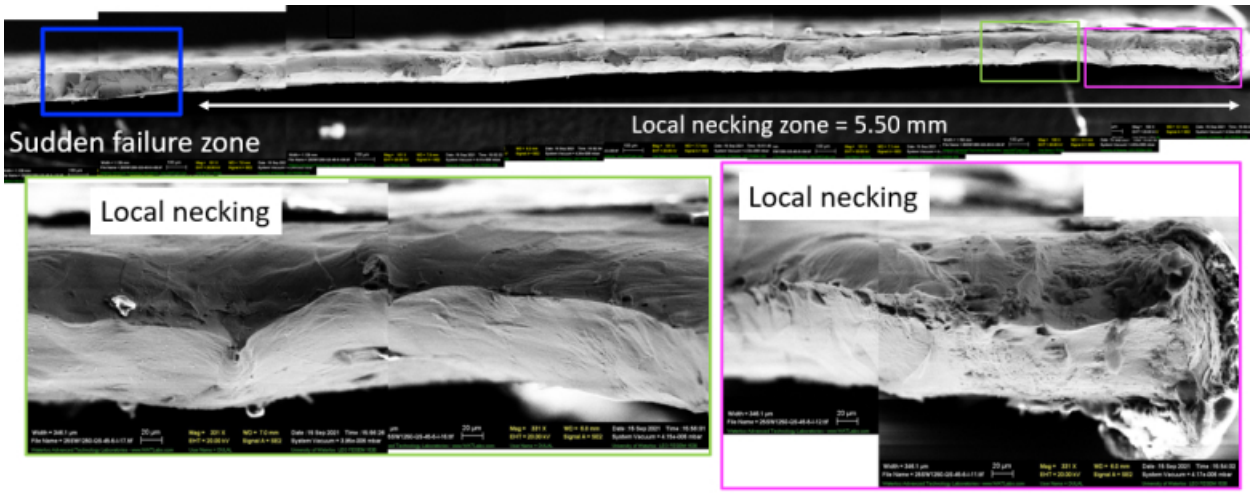

Figure 5.14: *SEM images of the typical fracture surface for specimens oriented along the 45° orientation*

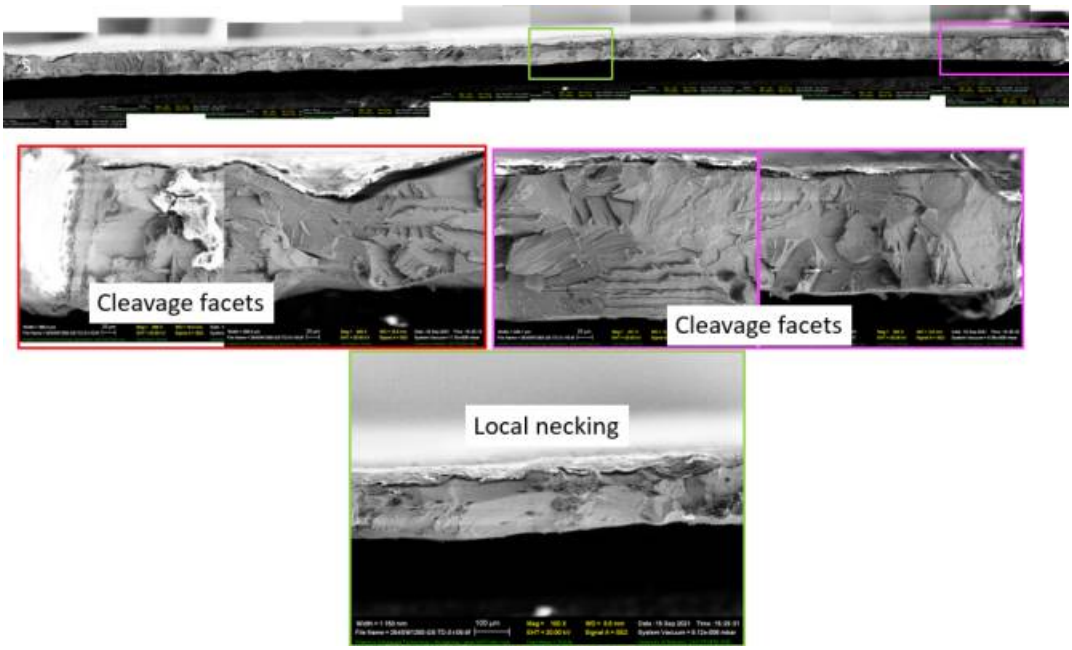

Figure 5.15: *SEM images of the typical fracture surface for specimens oriented along the transverse direction*

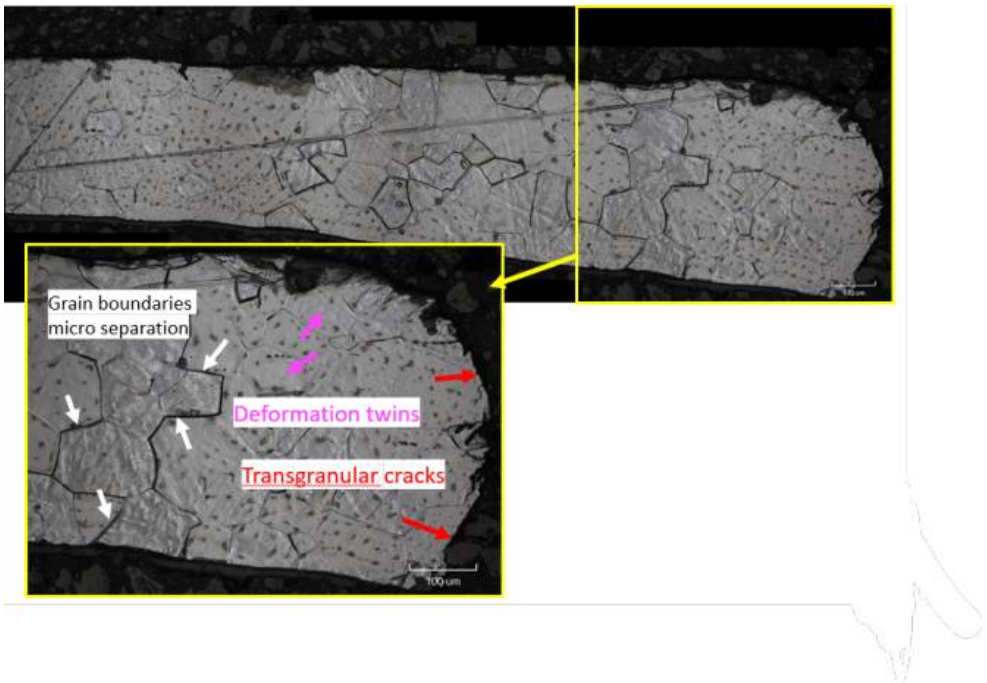

Figure 5.16: *Typical microstructure surrounding the fracture surface of the 25SW1250 specimens showing mechanisms of accommodating plastic deformation*

5.1.3 20SW1200

Tensile Properties

The normalized engineering and true stress-strain curves for all three directions are given in Figure 5.17 below. The normalized tensile properties are also presented in Table.5.3 below and were calculated using the data collected from the tests performed in each direction. The relationship between the true stress and strain and engineering stress and strain remains the same as described above for the 27PNX1350F grade as does the methodology in extracting the tensile properties and parameters of the Ramberg-Osgood model. Similar to the 27PNX1350F and 25SW1250 grades, the strain during plastic deformation was distributed in shear bands along the gauge length of the specimen for all three directions. Images showing the strain distribution for the three directions are shown in Figure 5.18

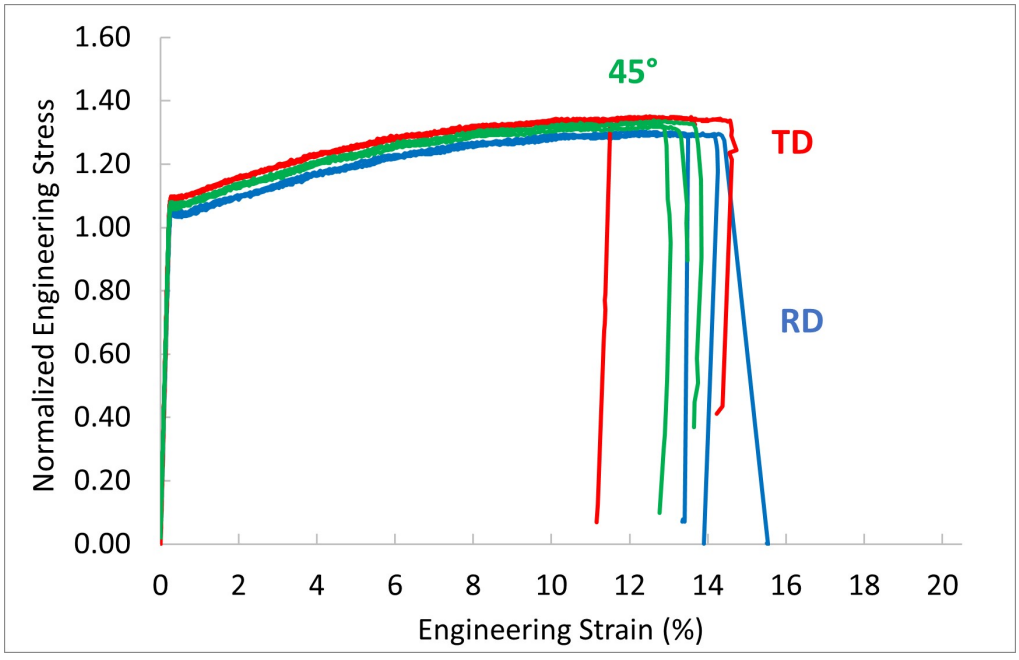

(a)

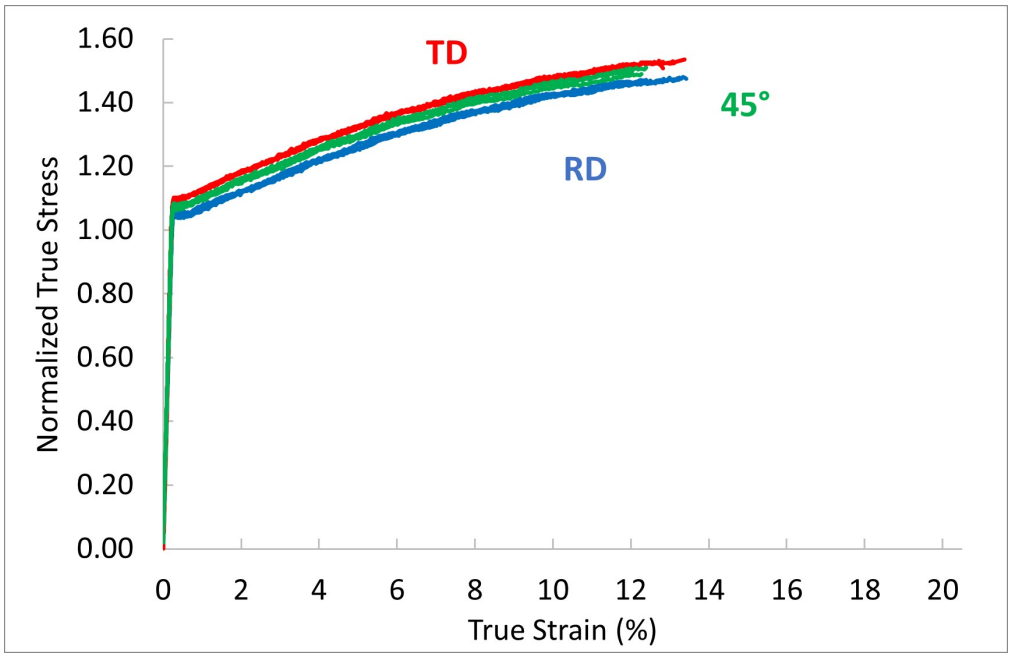

(b)

Figure 5.17: *Normalized stress-strain curves for 20SW1200 (a) Engineering (b) True*

Table 5.3: Normalized Mechanical Properties of 20SW1200 along the Different Directions

Mechanical	**RD**		**45°**		**TD**	
Properties	**Avg.**	**Std Dev.**	**Avg.**	**Std Dev.**	**Avg.**	**Std Dev.**
Elastic Modulus	441.60	2.61	466.50	3.16	483.49	1.48
Yield Strength	1.04	0.01	1.07	0.01	1.09	0.01
Engineering Ultimate Strength	1.30	0.01	1.33	0.01	1.35	0.01
True Ultimate Strength	1.47	0.004	1.50	0.01	1.52	0.03
Fracture Strain [%]	14	1	13	0	13	2
Reduction in Area [%]	6	0	6	0	6	1
Strength Coefficient, H	1.90	0.003	1.92	0.02	1.94	0.02
Strain Hardening exponent, n	0.13	0.00	0.12	0.00	0.12	0.00

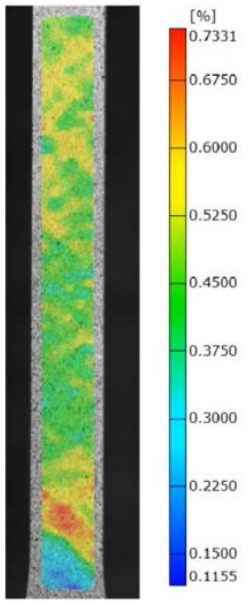

(a)

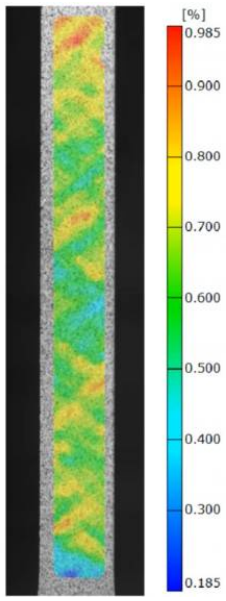

(b)

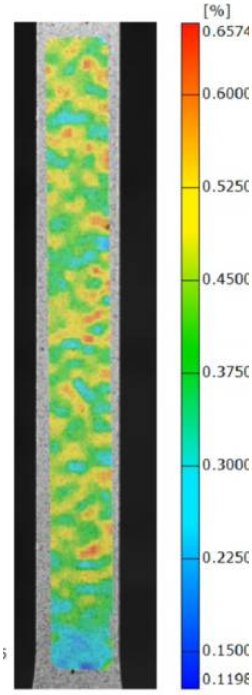

(c)

Figure 5.18: *Strain distribution for 20SW1200 specimens along the (a) Rolling Direction (b)45° Orientation (c)Transverse Direction*

5.1.4 Discussion

Along the rolling (RD) and transverse directions (TD) all three grades each had similar tensile properties. However, for the 27PNX1350F and 25SW1250 grades, the tensile properties along the 45° orientation had noticeable differences while for the 20SW1200 grade, the tensile properties along the 45° orientation were also similar to the rolling and transverse directions. For the 27PNX1350F grade, the 45° orientation showed higher strength properties when compared with the RD and TD directions while the opposite of this was observed for the 25SW1250 grade. Despite these differences, the 45° orientation generally displayed lower ductility than the other two directions regardless of the grade. A comparison of the average tensile properties of the three grades of electrical steel along the three directions has been shown in Figures 5.19, 5.21 and 5.20. From the figures, the three grades have comparable tensile properties with the 27PNX1350F and 25SW1250 grades performing slightly better and worse respectively. Therefore, from the tensile tests performed on three grades of non-oriented electrical steel sheets with different thicknesses, the tensile properties showed no trend to conclusively suggest that the sheet thickness had any effect on these properties. The distribution of strain during plastic deformation was consistent among all three directions and grades. The strain was distributed in shear bands across the length of the specimen during testing which then resolved themselves along the plane of fracture just before the crack initiated from one edge.

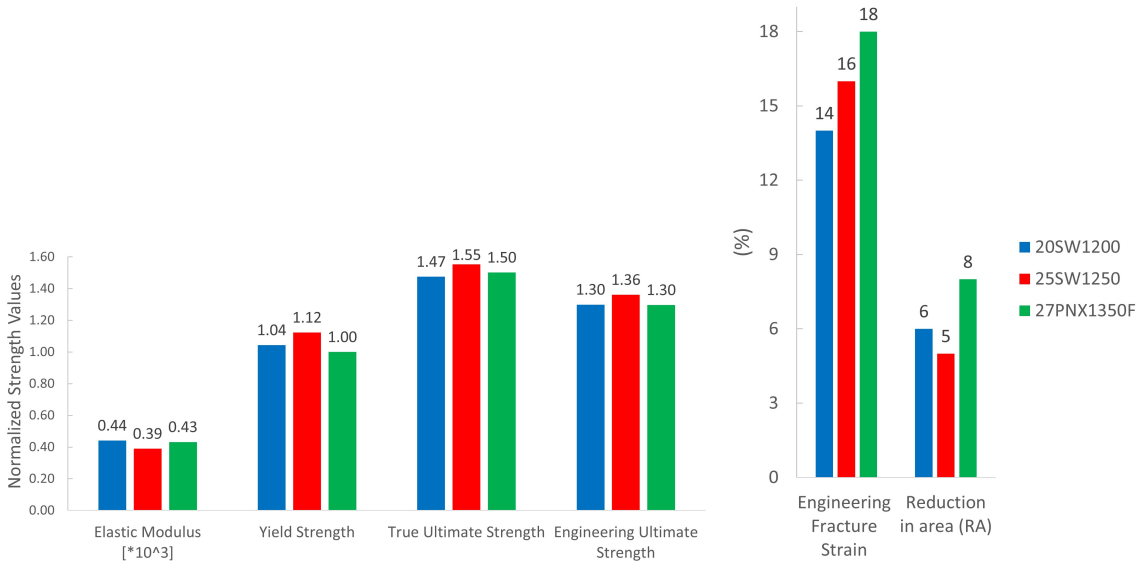

(a) (b)

Figure 5.19: *Average tensile properties along RD*

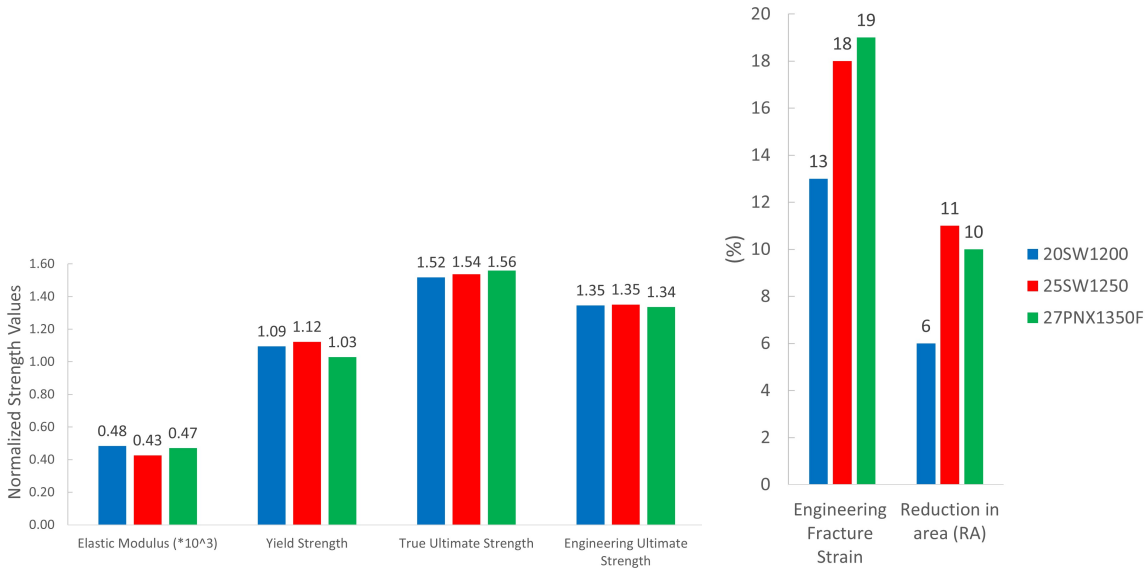

(a) (b)

Figure 5.20: *Average tensile properties along TD*

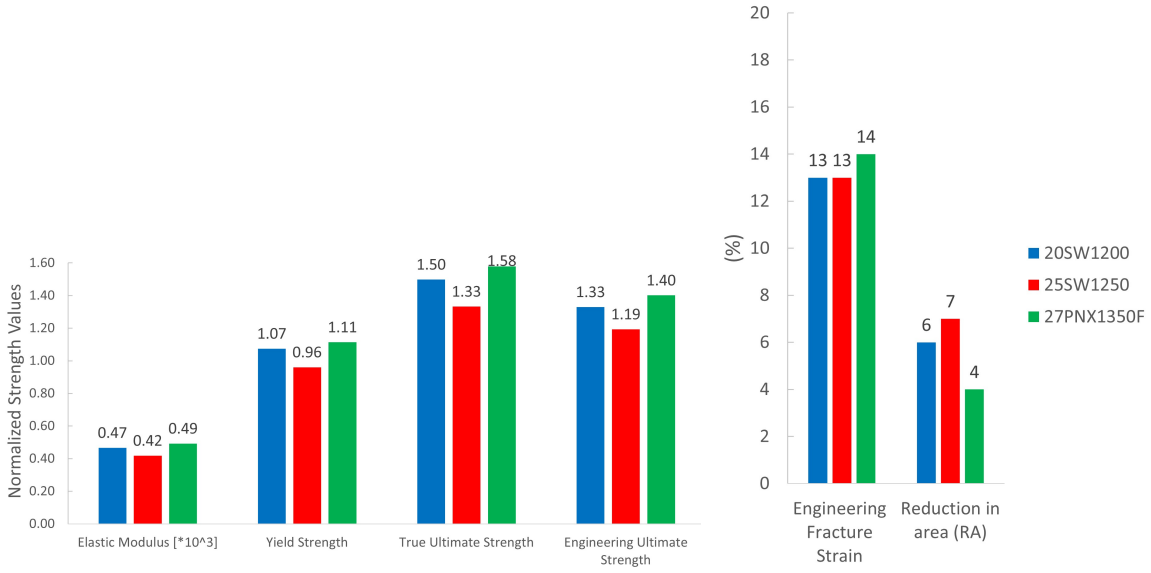

(a) (b)

Figure 5.21: *Average tensile properties along the 45° orientation*

The fractography of the fracture surfaces of the specimens revealed similar information across the three directions and grades investigated. Although there were no visible signs of necking on the fractured specimens, at least partial local necking was observed on the fracture surfaces. The fracture surfaces were characterized by a deformation zone where crack initiation and ductile crack propagation occurred and a sudden failure zone due to overload of the remaining area. While for the 27PNX1350F grades along the RD and TD, the sudden failure zone is almost non-existent, it is evidently present in the fracture surfaces along the 45° orientation and in the 25SW1250 grade irrespective of direction. The deformation zone failed along the grain boundary and thus was an intergranular type fracture while the sudden failure zone failed in a transgranular manner. The area around the fracture surface also revealed plastic deformation accommodation mechanisms such as the slip bands and deformation twins.

5.2 Chapter Conclusion

This chapter investigated the tensile properties of the three grades of electrical steel as well as explored the surfaces of the fractured specimens to identify the deformation mechanisms. The following conclusions can be drawn.

- The tensile properties along the rolling and transverse directions were comparable for all three grades of non-oriented electrical steel sheets tested at room temperature.
- The 20SW1200 grade showed the most isotropy out of the three grades of non-oriented electrical steel sheets tested in terms of its tensile properties at room temperature.
- Sheet thickness does not seem to have an effect on the tensile properties of non-oriented electrical steel sheets at room temperature.
- Although the fractured specimens had no visible signs of necking, it was observed locally along the fracture surface.
- The general fracture mode was a mix between intergranular type fracture in the ductile deformation region and transgranular type fracture in the sudden failure region.

Chapter 6

Tensile Properties of Non-Oriented Electrical Steel Sheets at an Elevated Temperature of 150°C

Since in its application the electric motor will be operating under a range temperatures from room to elevated temperatures, it is necessary to categorize the tensile properties at an elevated temperature and as such, quasi-static tensile tests were conducted non-oriented electrical steel sheets at 150°C. The purpose of these tensile tests was to categorize the tensile properties of non-oriented electrical steel sheets at an elevated temperature. After the tensile tests were completed, the fracture surfaces were studied to characterize the fracture mechanisms present under this loading condition. The results of this study are presented in this chapter.

6.1 Results and Discussion

6.1.1 *27PNX1350F*

Tensile Properties

The normalized engineering and true stress-strain curves for all three directions at 150°C are given in Figure. 6.1. The true stress (σ_T) and strain (ϵ_T) were calculated from the engineering stress (σ) and strain (ϵ) by the relationships given previously in Equations 2.1 and 2.2 respectively. The normalized tensile properties and Ramberg-Osgood parameters at 150°C are also presented in Table 6.1 below and were calculated using the data collected from the tests performed in each direction and with the same methodology as previously presented in Chapter 3. Similar to the tests performed at room temperature, strain during plastic deformation was distributed in shear bands along the gauge section of the specimen during the test rather than concentrated in a single region (see Figure 6.2).

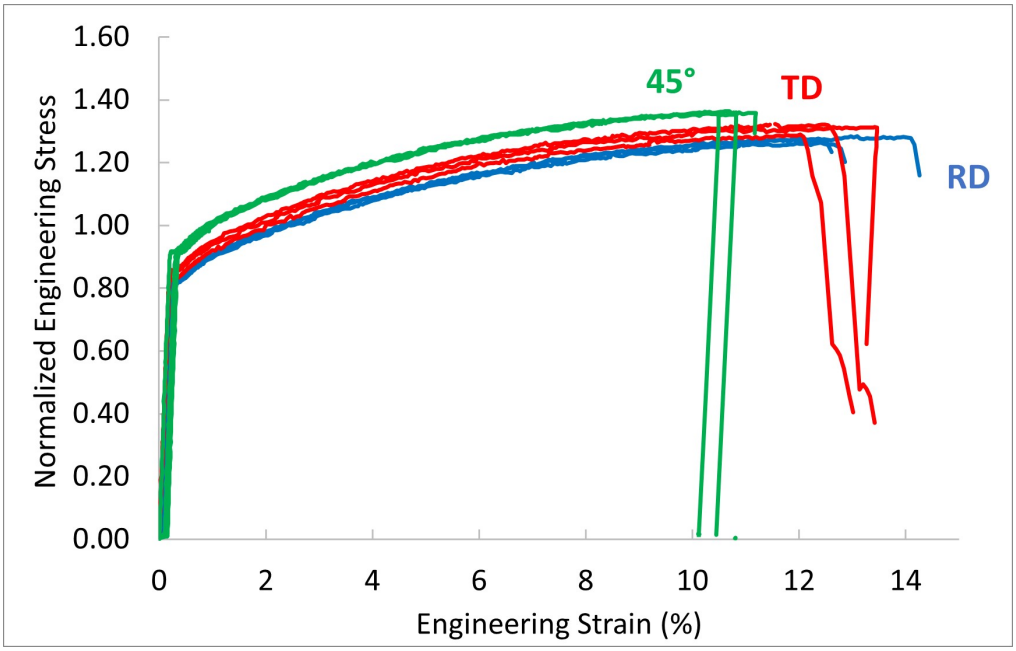

(a)

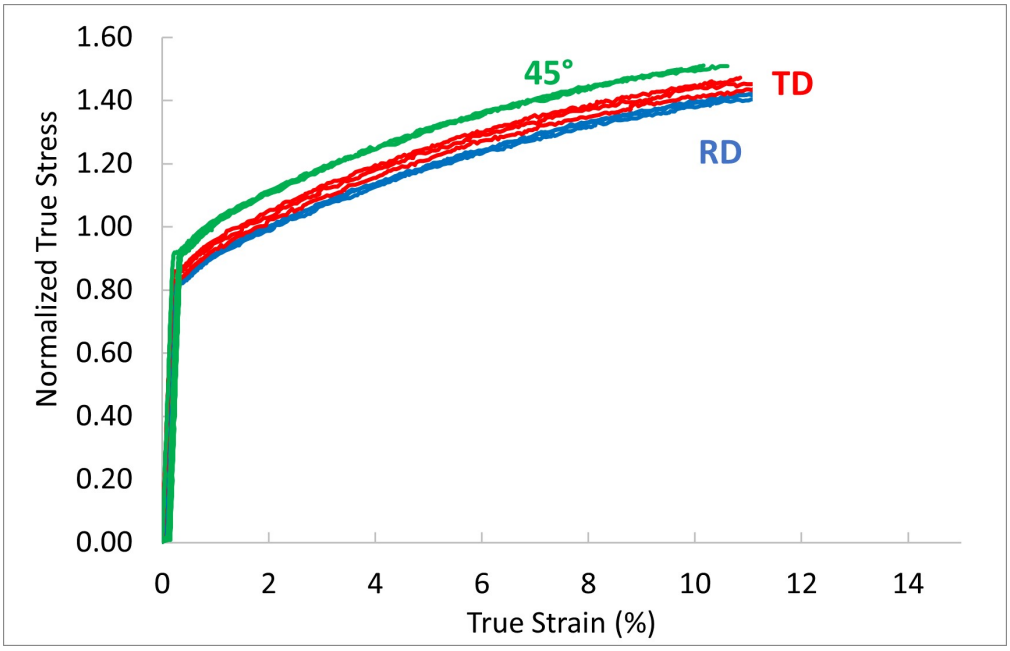

(b)

Figure 6.1: *Normalized stress-strain curves for 27PNX1350F at 150°C (a) Engineering (b) True*

Table 6.1: Normalized Mechanical Properties of 27PNX1350F at 150°C along the Different Directions

Mechanical	**RD**		**45°**		**TD**	
Properties	**Avg.**	**Std Dev.**	**Avg.**	**Std Dev.**	**Avg.**	**Std Dev.**
Elastic Modulus	407.22	1.27	469.08	7.25	447.07	7.56
Yield Strength	0.83	0.003	0.92	0.01	0.86	0.02
Engineering Ultimate Strength	1.27	0.01	1.36	0.002	1.31	0.02
True Ultimate Strength	1.44	0.02	1.51	0.01	1.47	0.02
Fracture Strain [%]	13	1	11	0	13	0
Reduction in Area [%]	6	1	4	0	8	1
Strength Coefficient, H	2.02	0.02	2.10	0.01	2.08	0.01
Strain Hardening exponent, n	0.17	0.00	0.15	0.00	0.17	0.00

Fracture Analysis

Similar to the specimens at room temperature, as shown in Figure 6.3, these specimens also fractured at an angle to the loading direction which is indicative of a ductile mode of fracture. The fracture surface along all three directions showed similar features. Local necking was observed on the fracture surfaces evidenced by the reduction in thickness as shown in Figure 6.4. Studying the microstructure around the fracture region showed severely deformed grains as well as the presence of deformation twins (see Figure 6.5).

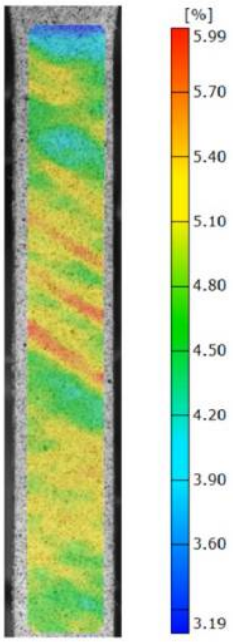

(a)

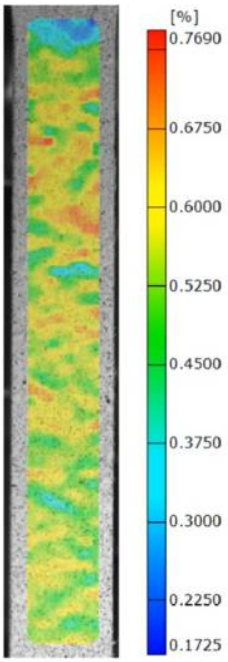

(b)

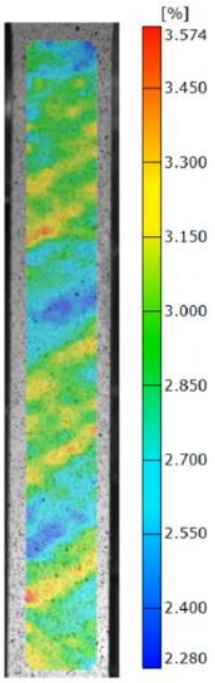

(c)

Figure 6.2: *Strain distribution at 150°C for 27PNX1350F specimens along the (a) Rolling Direction (b)45° Orientation (c)Transverse Direction*

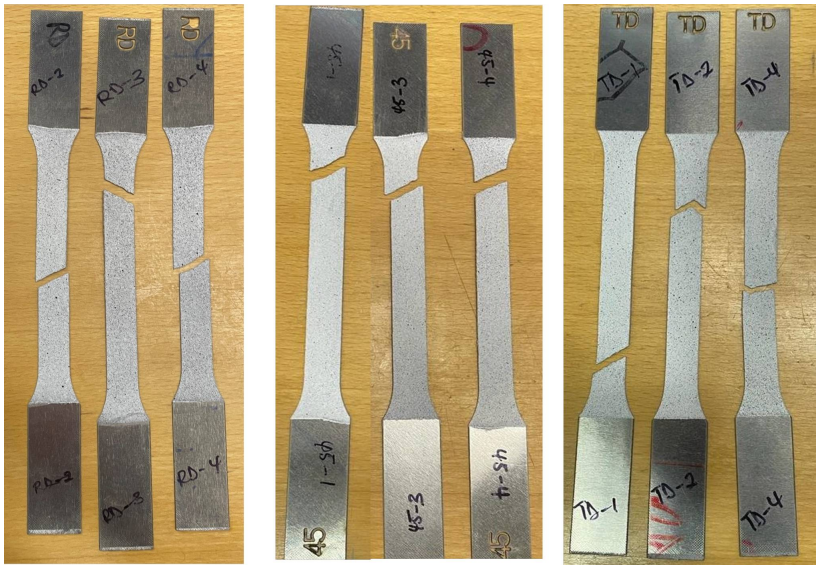

Figure 6.3: *Fractured 27PNX1350F specimens along the Rolling, 45° and Transverse Directions respectively at 150°C*

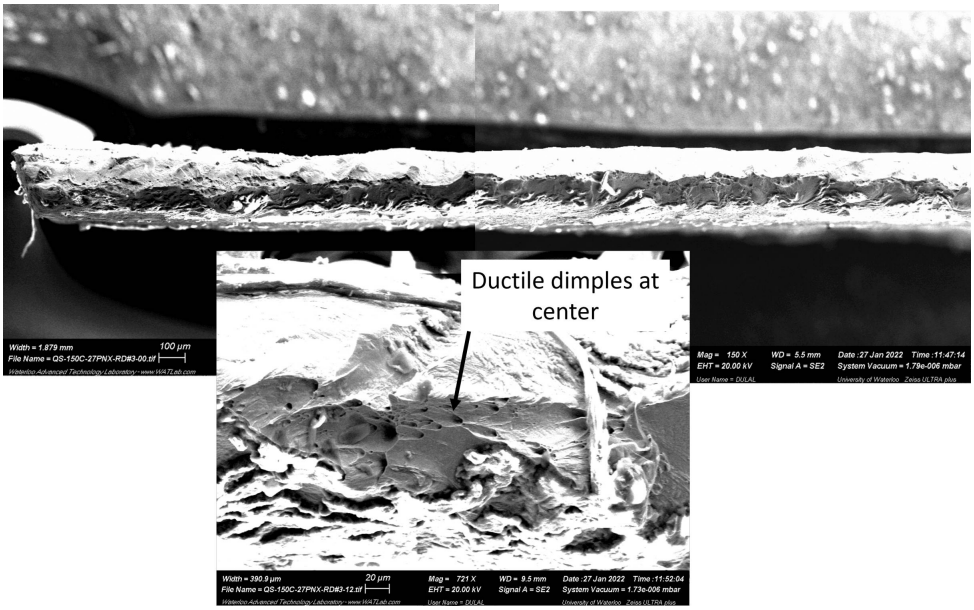

Figure 6.4: *Typical fracture surface specimens along tall three directions at 150°C*

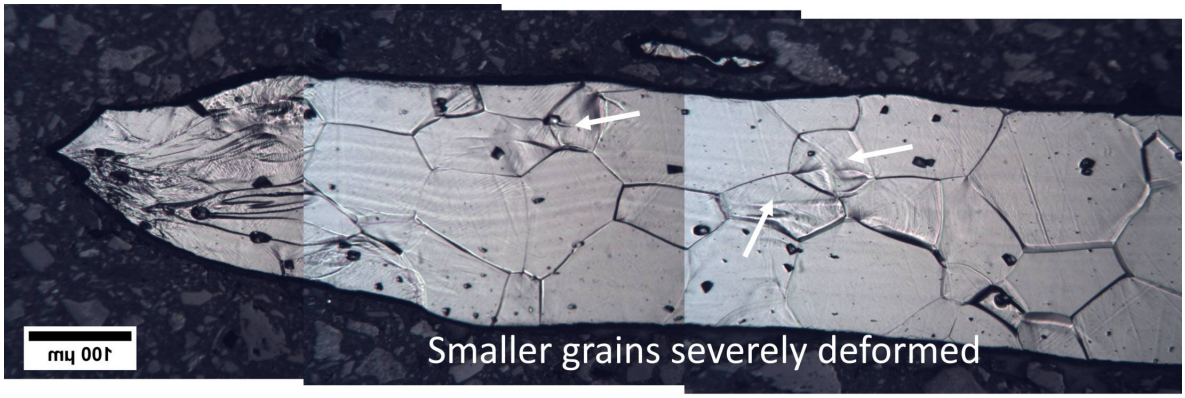

(a)

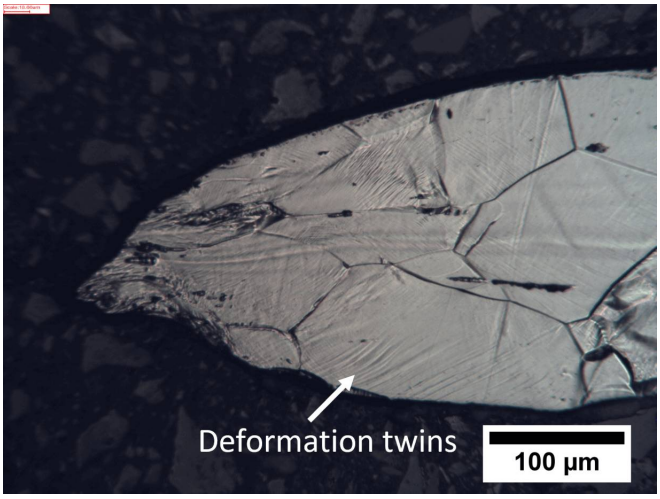

(b)

Figure 6.5: *Typical microstructure surrounding the fracture region of specimens in all three directions at 150° C*

6.1.2 25SW1250

Tensile Properties

The normalized engineering and true stress-strain curves for all three directions at 150°C are given in Figure 6.6. The normalized tensile properties at 150°C are also presented in Table 6.2 and were calculated using the data collected from the tests performed in each direction.

The relationship between the true stress and strain and engineering stress and strain remains the same as described above in Chapter 3 as does the methodology in extracting the tensile properties and parameters of the Ramberg-Osgood model. Similar to the tests performed at room temperature, the strain during plastic deformation was distributed in shear bands along the gauge length of the specimen for all three directions. Images showing the strain distribution for the three directions in Figure 6.7

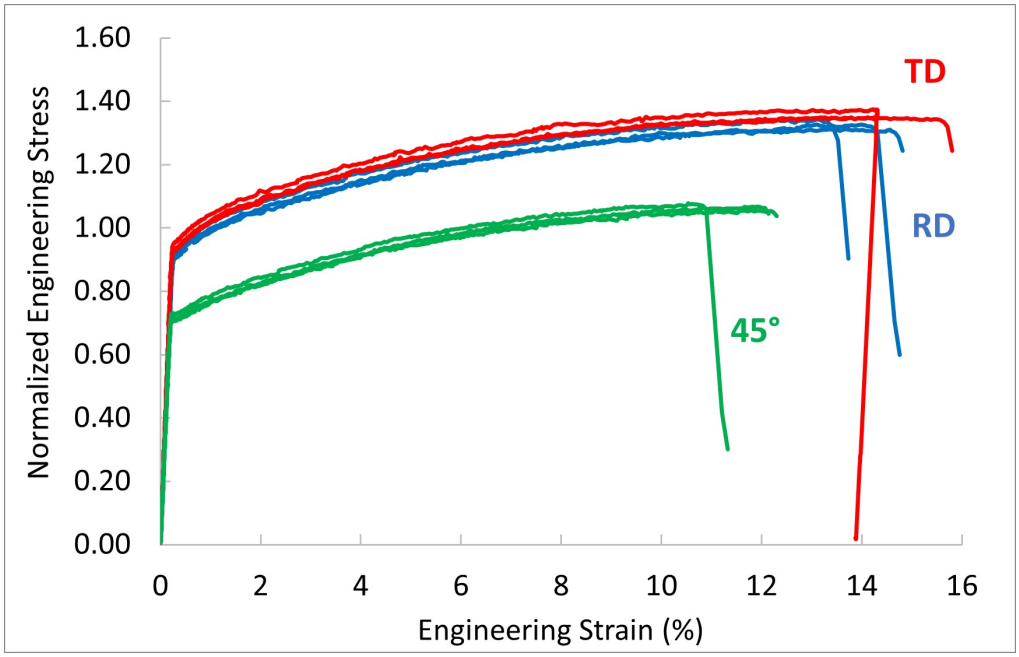

(a)

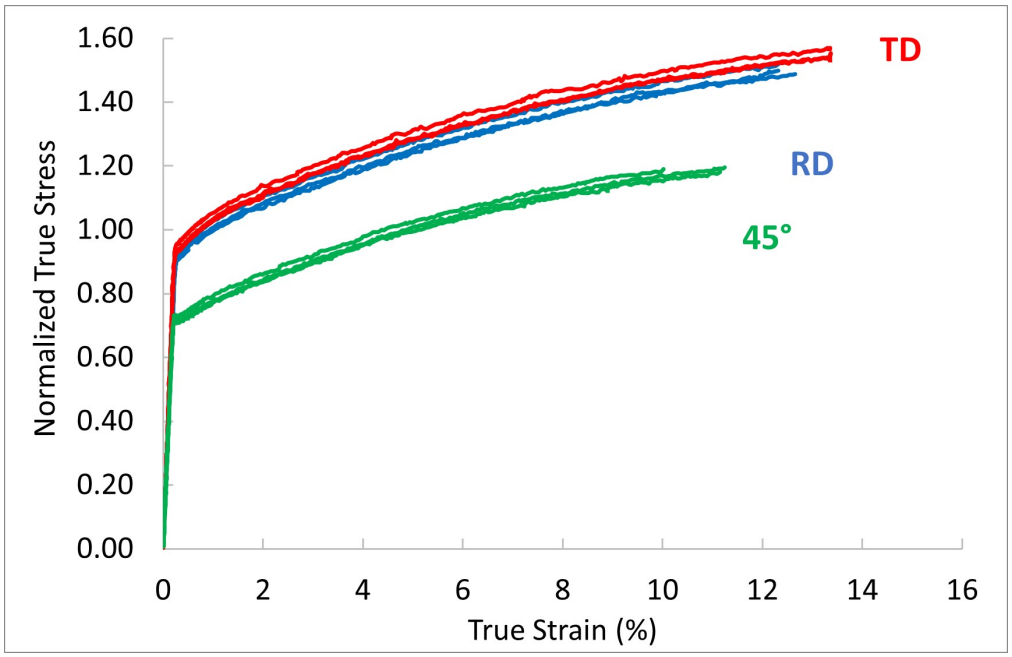

(b)

Figure 6.6: *Normalized stress-strain curves at 150° C for 25SW1250 (a) Engineering (b) True*

Table 6.2: Normalized Mechanical Properties of 25SW1250 at 150°C along the Different Directions

Mechanical	**RD**		**45°**		**TD**	
Properties	**Avg.**	**Std Dev.**	**Avg.**	**Std Dev.**	**Avg.**	**Std Dev.**
Elastic Modulus	376.01	4.27	354.15	7.32	419.30	1.19
Yield Strength	0.94	0.01	0.72	0.01	0.96	0.01
Engineering Ultimate Strength	1.33	0.02	1.07	0.01	1.36	0.01
True Ultimate Strength	1.50	0.02	1.19	0.01	1.55	0.01
Fracture Strain [%]	14	1	12	1	15	1
Reduction in Area [%]	9	2	6	0	14	1
Strength Coefficient, H	2.01	0.02	1.68	0.05	2.05	0.02
Strain Hardening exponent, n	0.15	0.00	0.16	0.01	0.14	0.00

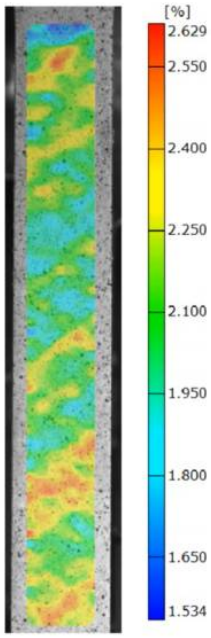

(a)

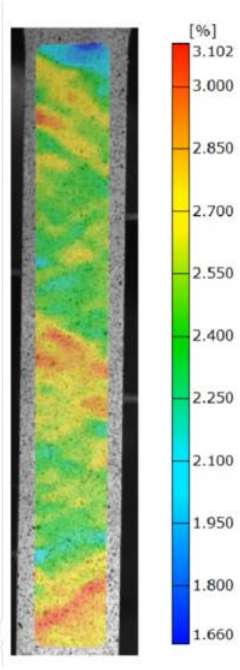

(b)

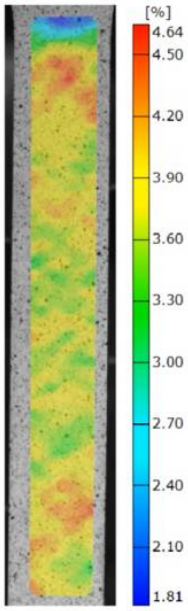

(c)

Figure 6.7: *Strain distribution at 150°C for 25SW1250 specimens along the (a) Rolling Direction (b)45° Orientation (c)Transverse Direction*

6.1.3 20SW1200

Tensile Properties

The normalized engineering and true stress-strain curves for all three directions at 150°C are given in Figure 6.8. The normalized tensile properties at 150°C are also presented in Table 6.3 and were calculated using the data collected from the tests performed in each direction. The relationship between the true stress and strain and engineering stress and strain remains the same as described in Chapter 4 as does the methodology in extracting the tensile properties and parameters of the Ramberg-Osgood model. Similar to the tests performed at room temperature, the strain during plastic deformation was also distributed in shear bands along the gauge length of the specimen for all three directions. Images showing the strain distribution for the three directions for one test are shown in Figure. 6.9

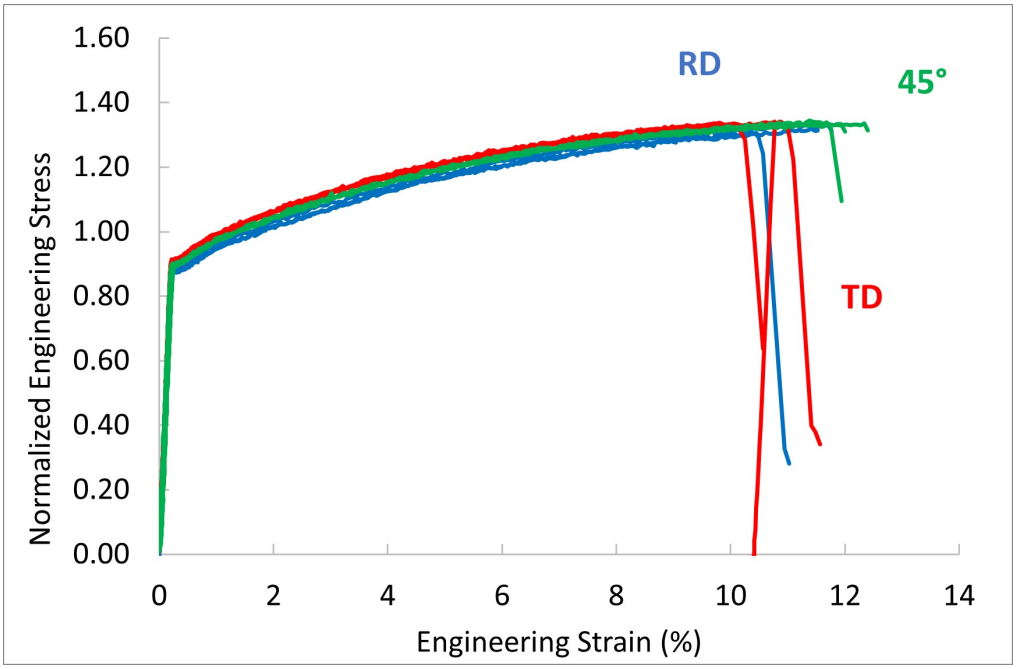

(a)

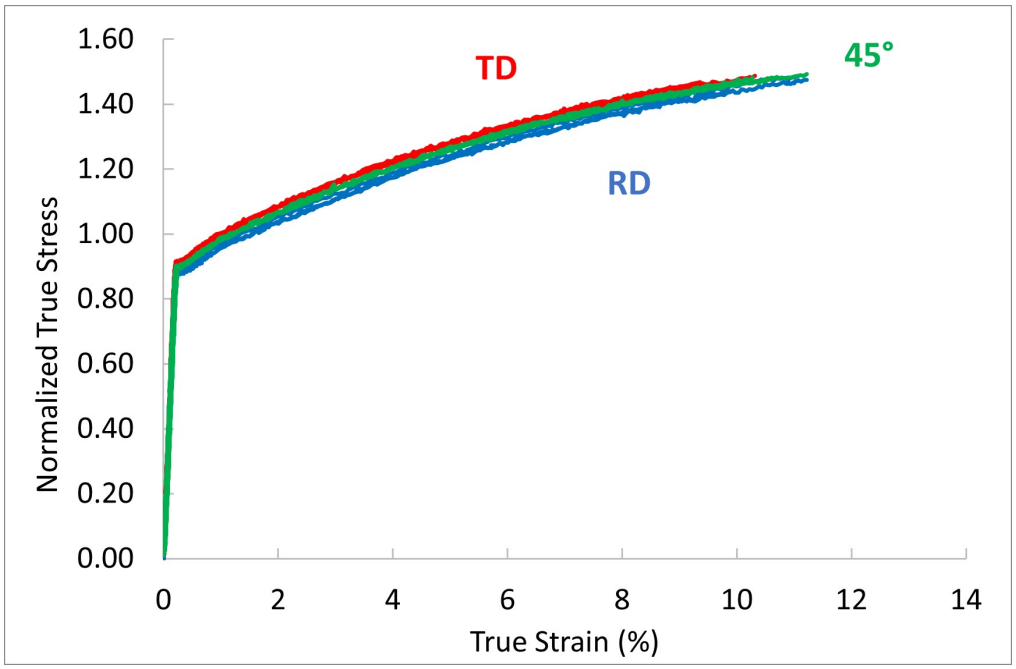

(b)

Figure 6.8: *Normalized stress-strain curves at 150° C for 20SW1200 (a) Engineering (b) True*

Table 6.3: Normalized Mechanical Properties of 20SW1200 at 150°C along the Different Directions

Mechanical	**RD**		**45°**		**TD**	
Properties	**Avg.**	**Std Dev.**	**Avg.**	**Std Dev.**	**Avg.**	**Std Dev.**
Elastic Modulus	423.37	4.81	425.89	29.20	459.80	2.39
Yield Strength	0.89	0.01	0.91	0.01	0.93	0.004
Engineering Ultimate Strength	1.32	0.01	1.34	0.01	1.34	0.003
True Ultimate Strength]	1.47	0.020	1.49	0.01	1.48	0.01
Fracture Strain [%]	12	0	12	0	11	1
Reduction in Area [%]	6	0	6	0	6	1
Strength Coefficient, H	2.08	0.04	2.08	0.02	2.06	0.01
Strain Hardening exponent, n	0.17	0.00	0.16	0.00	0.15	0.00

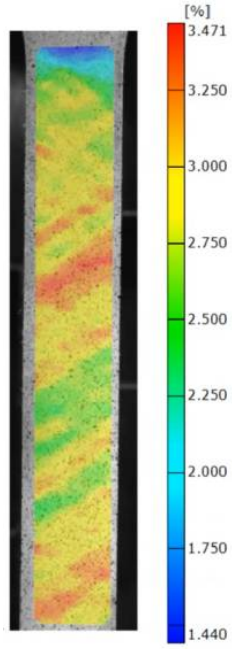

(a)

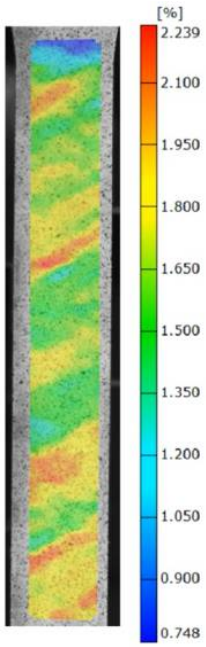

(b)

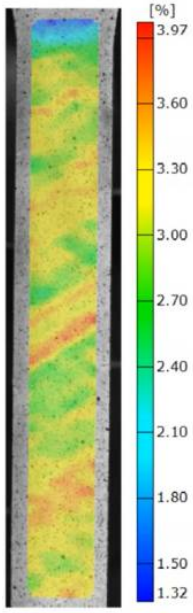

(c)

Figure 6.9: *Strain distribution for 20SW1200 specimens at 150°C along the (a) Rolling Direction (b)45° Orientation (c)Transverse Direction*

6.1.4 Discussion

Similar to the room temperature tests, the rolling (RD) and transverse directions (TD) all three grades each had similar tensile properties. However, for the 27PNX1350F and 25SW1250 grades, the tensile properties along the 45° orientation had noticeable differences while for the 20SW1200 grade, the tensile properties along the 45° orientation were also similar to the rolling and transverse directions. For the 27PNX1350F grade, the specimens oriented along 45° showed higher strength properties when compared with the RD and TD directions while the opposite of this was observed for the 25SW1250 grade. Despite these differences, the 45° orientation generally displayed lower ductility than the other two directions regardless of the grade. A comparison of the average tensile properties of the three grades of electrical steel along the three directions has been shown in Figures 6.10, 6.12 and 6.11. From the figures, the three grades have comparable tensile properties along the rolling and transverse directions. The 25SW1250 grade has noticeably lower strength properties along the 45° orientation. This observation was not seen in the comparison of the three grades at room temperature. At 150°C, there is also no trend to conclusively suggest that the sheet thickness had any effect on the tensile properties. Once again, the distribution of strain during plastic deformation was consistent among all three directions and grades. The strain was distributed in shear bands across the length of the specimen rather than being concentrated at a point.

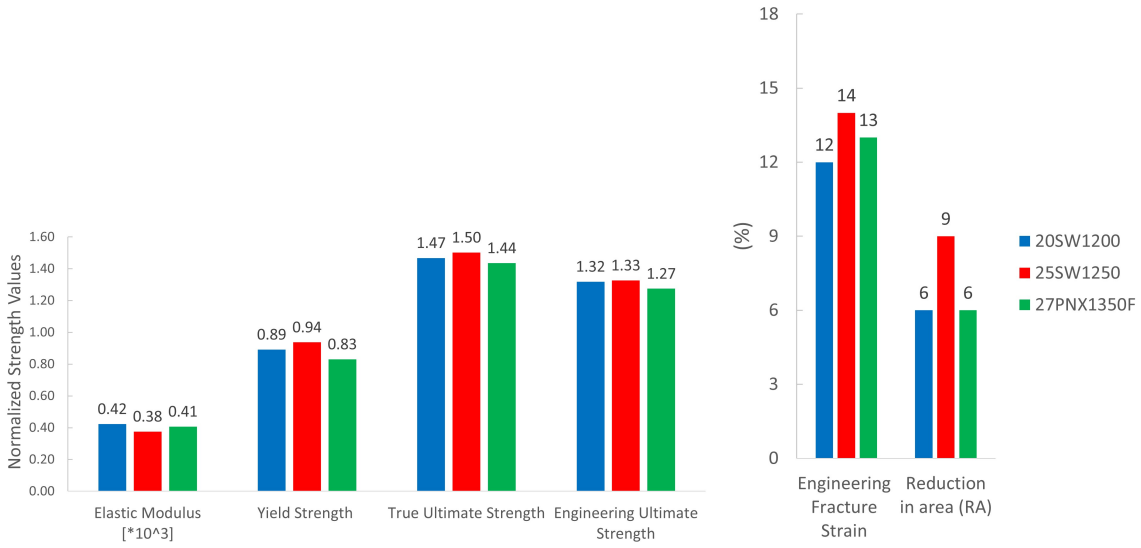

(a) (b)

Figure 6.10: *Average tensile properties at 150° C along RD*

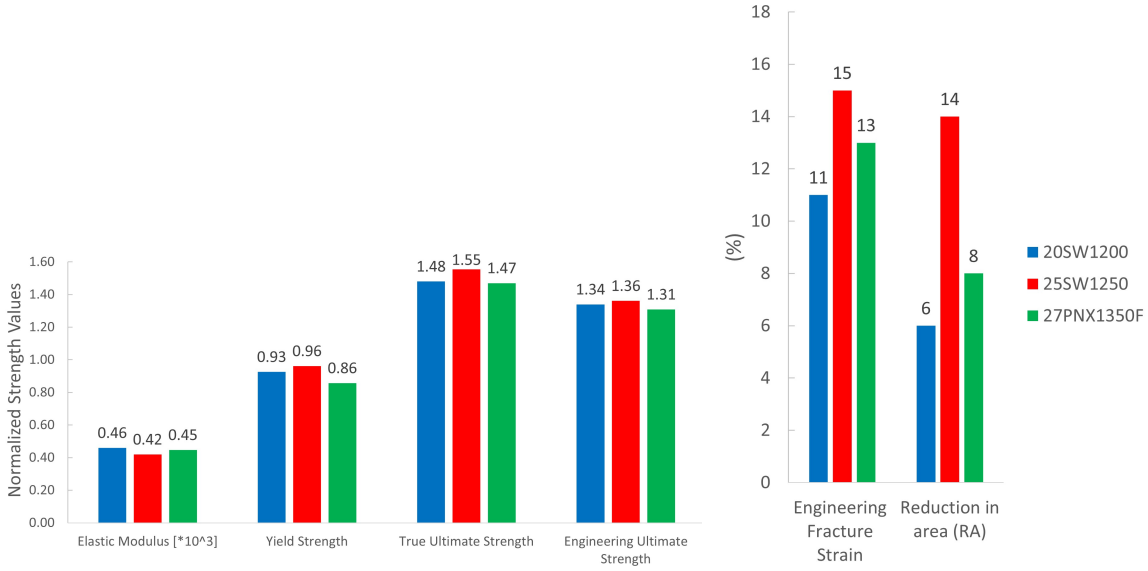

(a) (b)

Figure 6.11: *Average tensile properties at 150° C along TD*

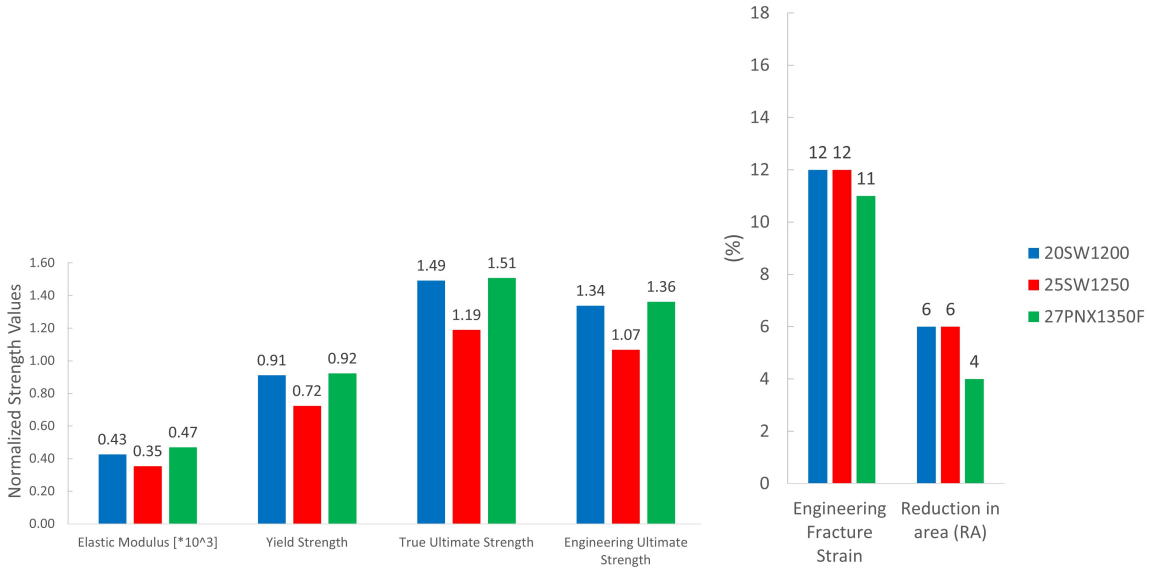

(a) (b)

Figure 6.12: *Average tensile properties at 150° C along the 45° Orientation*

6.1.5 Effect of Temperature on the Tensile Properties of Thin Electrical Steel Sheets

The effect of temperature on the tensile properties of the three grades of non-oriented electrical steel sheets along the rolling direction, transverse direction and at a 45° orientation were investigated.

27PNX1350F

In general, the tests at 150°C showed lower yield strength and elongation when compared to the tests at room temperature. However, the ultimate tensile strengths at the two temperatures remained comparable. The following tables and figures summarize the effect

of temperature on the tensile properties of the 27PNX1350F grade of non-oriented electrical steel sheet. An interesting observation from the tables and figures is that irrespective of the direction, the percent difference between the yield strength at room temperature and 150°C is 17%. The effect of temperature on the tensile properties of these steel alloys was an earlier elastic to plastic regime transition as well as a reduction in the amount of deformation the material can accommodate before fracture.

Table 6.4: Normalized Mechanical Properties of 27PNX1350F at Room Temperature vs 150°C along the Rolling Direction

Mechanical	**RT**		**150°C**		**Difference**
Properties	**Avg.**	**Std Dev.**	**Avg.**	**Std Dev.**	**(%)**
Elastic Modulus	432.28	1.93	407.22	1.27	6
Yield Strength	1.00	0.004	0.83	0.003	17
Engineering Ultimate Strength	1.30	0.006	1.27	0.01	2
Fracture Strain [%]	18	1	13	1	26

Table 6.5: Normalized Mechanical Properties of 27PNX1350F at Room Temperature vs 150°C along the 45° Orientation

Mechanical Properties	**RT**		**150°C**		**Difference (%)**
	Avg.	**Std Dev.**	**Avg.**	**Std Dev.**	
Elastic Modulus	492.72	1.23	469.08	7.25	5
Yield Strength	1.11	0.004	0.92	0.01	17
Engineering Ultimate Strength	1.40	0.01	1.36	0.002	3
Engineering Fracture Strain [%]	19	1	13	0	31

Table 6.6: Normalized Mechanical Properties of 27PNX1350F at Room Temperature vs 150°C along the Transverse Direction

Mechanical Properties	**RT**		**150°C**		**Difference (%)**
	Avg.	**Std Dev.**	**Avg.**	**Std Dev.**	
Elastic Modulus	470.42	3.79	447.07	7.56	5
Yield Strength	1.03	0.003	0.86	0.02	17
Engineering Ultimate Strength	1.34	0.004	1.31	0.02	2
Engineering Fracture Strain [%]:	10	0	8	1	20

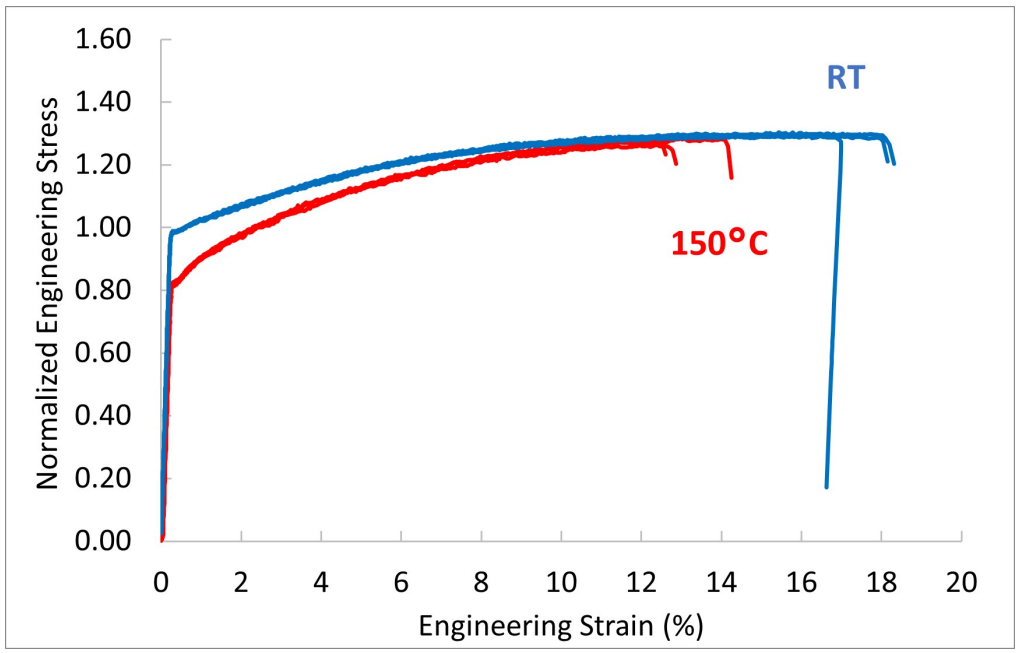
1.60
1.40
1.20
1.00
0.80
0.60
0.40
0.20
0.00
Normalized Engineering Stress
RT
150°C
0
2
4
6
8
10
12
14
16
18
20
Engineering Strain (%)

(a)

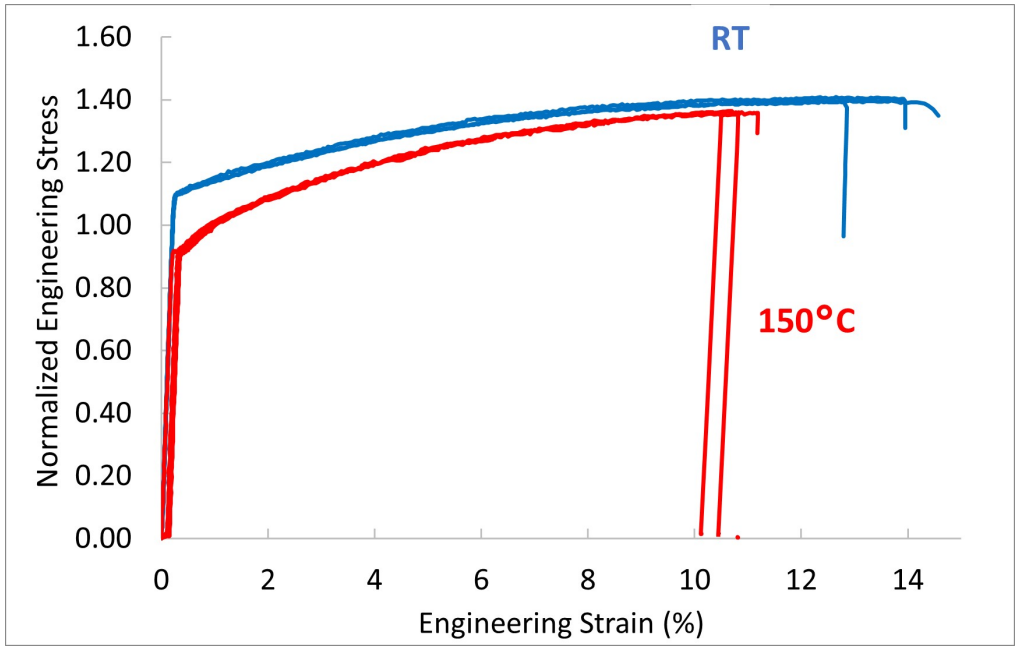
1.60
1.40
1.20
1.00
0.80
0.60
0.40
0.20
0.00
Normalized Engineering Stress
RT
150°C
0
2
4
6
8
10
12
14
Engineering Strain (%)

(b)

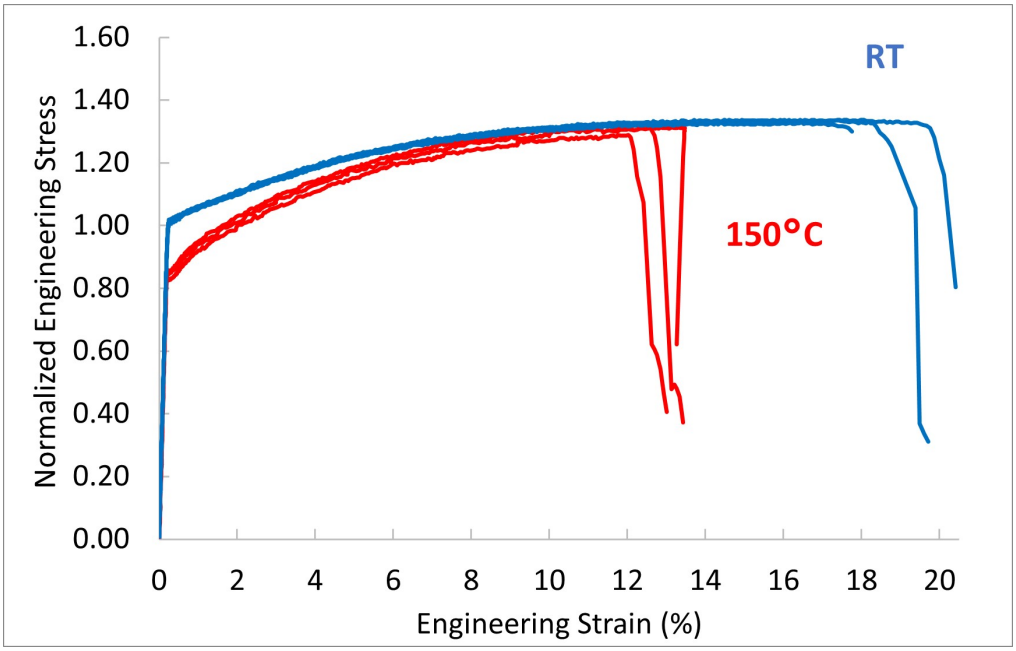

(c)

Figure 6.13: *Stress-Strain curves at RT vs 150°C along (a) RD (b)45° Orientation (c)TD*

25SW1250

Similar to the comparison of the 27PNX1350F grade, the tests at 150°C for the 25SW1250 showed lower yield strength and elongation when compared to the tests at room temperature. The ultimate tensile strength at the two temperatures remained comparable along the rolling and transverse directions while along the 45° orientation, the tensile strength at 150°C was noticeably lower than at room temperature. The following tables and figures summarize the effect of temperature on the tensile properties of the 25SW1250 grade of non-oriented electrical steel sheets. In this grade, the percent difference between the yield strength at RT and 150°C showed a deviation along the 45° orientation. While the percent difference at the rolling and transverse directions are comparable, the percent difference along the 45° orientation is quite larger than the other two directions. The previously stated effect of

temperature on the elastic to plastic transition holds here as well however, the percentage seems to be relatively constant for only two directions. The reduction in the in the amount of deformation the material can accommodate before fracture is also noted as an effect of the temperature here as well. Finally, along the 45° orientation, an overall reduction in the tensile properties was observed.

Table 6.7: Normalized Mechanical Properties of 25SW1250 at Room Temperature vs 150°C along the Rolling Direction

Mechanical	**RT**		**150°C**		**Difference**
Properties	**Avg.**	**Std Dev.**	**Avg.**	**Std Dev.**	**(%)**
Elastic Modulus	389.92	2.24	376.01	4.27	4
Yield Strength	1.12	0.01	0.94	0.01	17
Engineering Ultimate Strength	1.36	0.004	1.33	0.02	3
Fracture Strain [%]	5	1	9	2	57

Table 6.8: Normalized Mechanical Properties of 25SW1250 at Room Temperature vs 150°C along the 45° Orientation

Mechanical Properties	**RT**		**150°C**		**Difference (%)**
	Avg.	**Std Dev.**	**Avg.**	**Std Dev.**	
Elastic Modulus	418.15	1.73	354.15	7.32	15
Yield Strength	0.96	0.01	0.72	0.01	25
Engineering Ultimate Strength	1.19	0.004	1.07	0.01	11
Engineering Fracture Strain [%]	13	1	12	1	10

Table 6.9: Normalized Mechanical Properties of 25SW1250 at Room Temperature vs 150°C along the Transverse Direction

Mechanical Properties	**RT**		**150°C**		**Difference (%)**
	Avg.	**Std Dev.**	**Avg.**	**Std Dev.**	
Elastic Modulus	426.43	2.40	419.30	1.19	2
Yield Strength	1.12	0.004	0.96	0.01	14
Engineering Ultimate Strength	1.35	0.004	1.36	0.01	1
Engineering Fracture Strain [%]	11	2	14	1	21

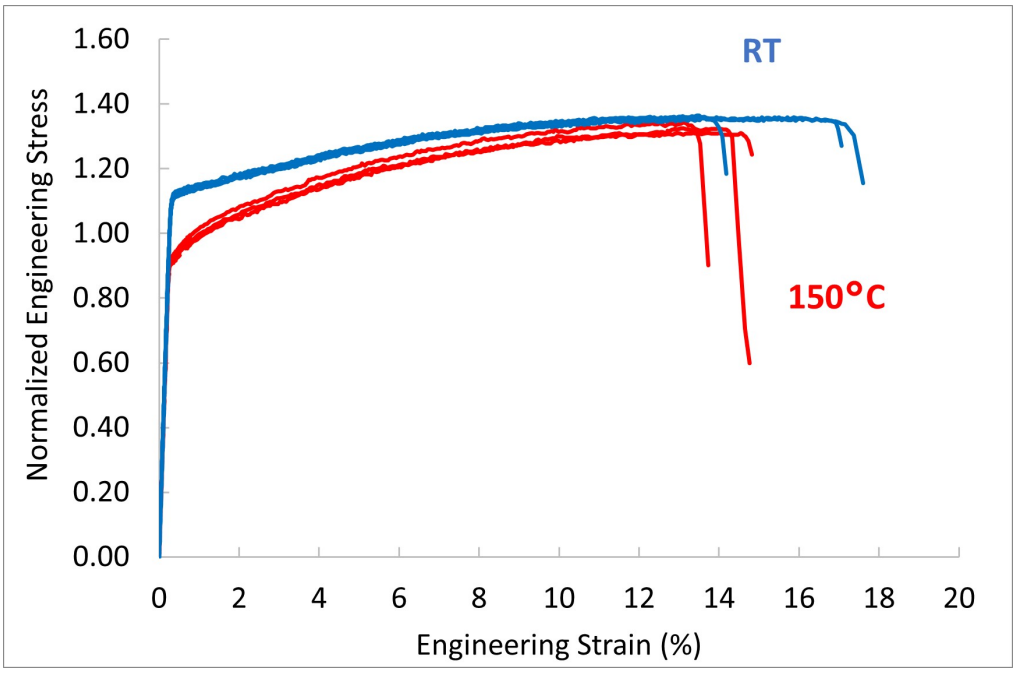
RT
150°C
Normalized Engineering Stress
Engineering Strain (%)
1.60
1.40
1.20
1.00
0.80
0.60
0.40
0.20
0.00
0
2
4
6
8
10
12
14
16
18
20

(a)

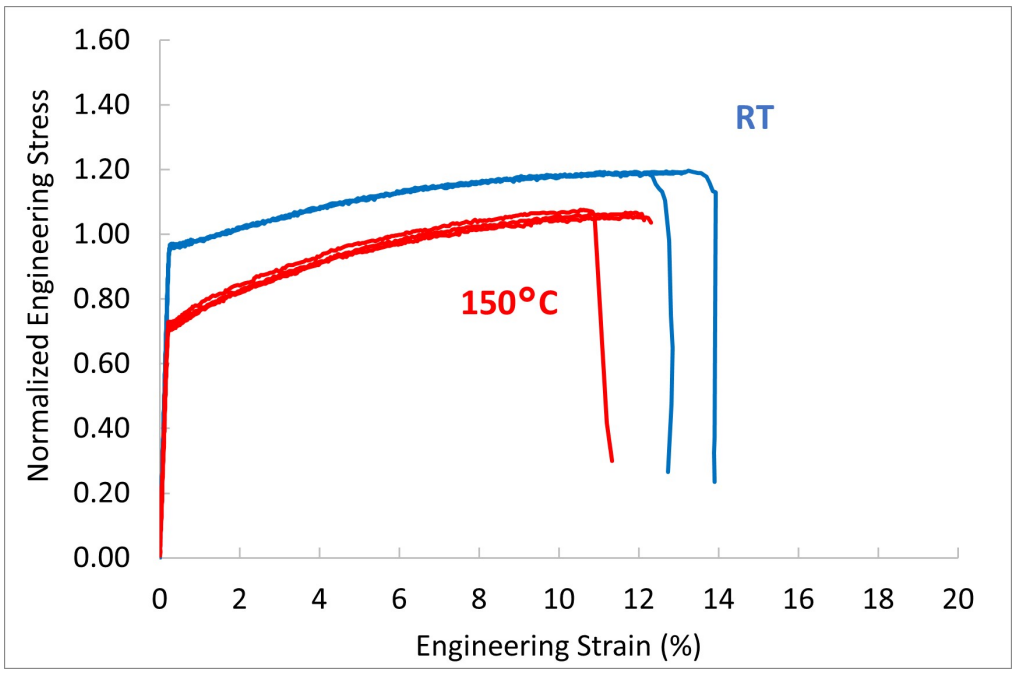
RT
150°C
Normalized Engineering Stress
Engineering Strain (%)
1.60
1.40
1.20
1.00
0.80
0.60
0.40
0.20
0.00
0
2
4
6
8
10
12
14
16
18
20

(b)

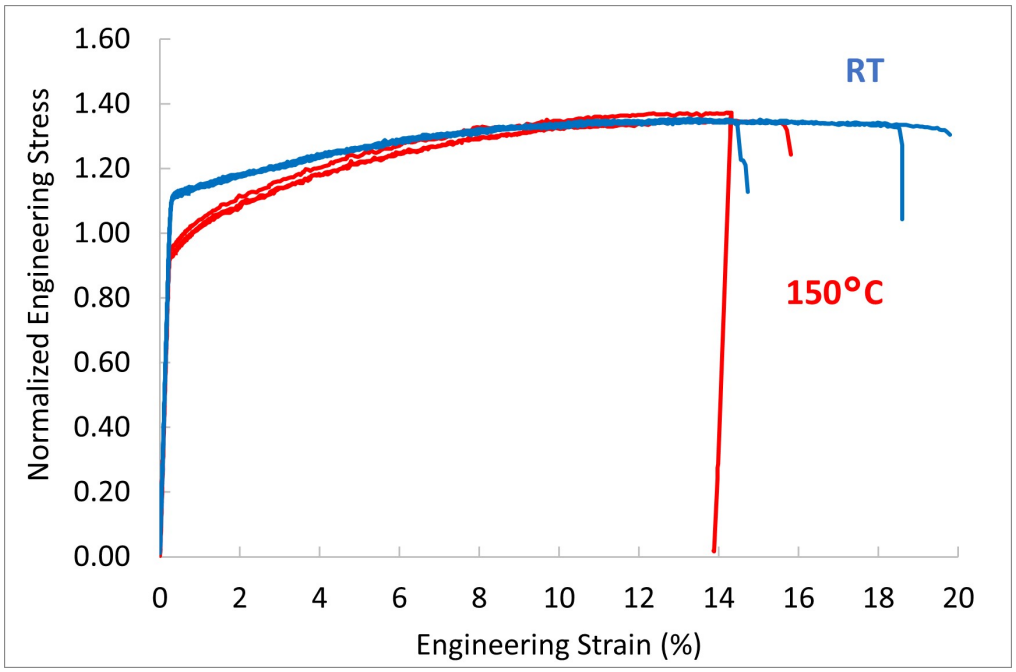

(c)

Figure 6.14: *Comparison of the stress-strain curves at RT and 150° C at (a) Rolling Direction (b)45° Orientation (c)Transverse Direction*

20SW1200

The comparison of the test run at RT and 150°C for the 20SW1200 grade produced similar results as the 27PNX1350F grade. Similar to the previous two grades, the yield strength at 150°C is evidently lower than at room temperature while the ultimate tensile strength remained comparable. Similar to the 27PN1350F grade, the yield strength at 150°C is reduced by a constant percentage irrespective of direction. The elongation at fracture is also lower at 150°C. Therefore, in this grade as well, the increase in temperature results in a lower elastic to yield transition strength as well as a reduction in the deformation capability of the sheets. The following tables and figures summarize the effect of temperature on the tensile properties of the 20SW1200 grade of non-oriented electrical steel sheets.

Table 6.10: Normalized Mechanical Properties of 20SW1200 at Room Temperature vs 150°C along the Rolling Direction

Mechanical	**RT**		**150°C**		**Difference**
Properties	**Avg.**	**Std Dev.**	**Avg.**	**Std Dev.**	**(%)**
Elastic Modulus	441.60	2.61	423.37	4.81	4
Yield Strength	1.04	0.01	0.89	0.01	15
Engineering Ultimate Strength	1.30	0.01	1.32	0.01	2
Fracture Strain [%]	14	1	12	0	20

Table 6.11: Normalized Mechanical Properties of 20SW1200 at Room Temperature vs 150°C along the 45° Orientation

Mechanical Properties	**RT**		**150°C**		**Difference (%)**
	Avg.	**Std Dev.**	**Avg.**	**Std Dev.**	
Elastic Modulus	466.50	3.16	425.89	29.20	9
Yield Strength	1.07	0.01	0.91	0.01	15
Engineering Ultimate Strength	1.33	0.01	1.34	0.01	1
Engineering Fracture Strain [%]	6	0	6	0	0

Table 6.12: Normalized Mechanical Properties of 20SW1200 at Room Temperature vs 150°C along the Transverse Direction

Mechanical Properties	**RT**		**150°C**		**Difference (%)**
	Avg.	**Std Dev.**	**Avg.**	**Std Dev.**	
Elastic Modulus	483.49	1.48	459.80	2.39	5
Yield Strength	1.09	0.01	0.93	0.004	15
Engineering Ultimate Strength	1.35	0.01	1.34	0.003	0.5
Engineering Fracture Strain [%]	13	2	11	1	18

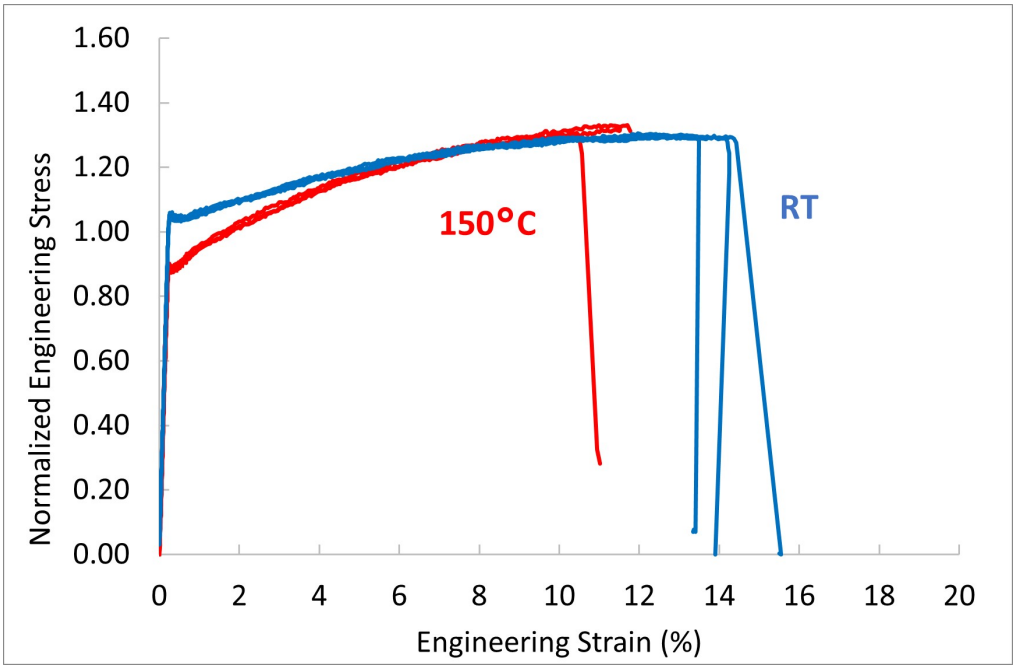
1.60
1.40
1.20
1.00
0.80
0.60
0.40
0.20
0.00
Normalized Engineering Stress
150°C
RT
0
2
4
6
8
10
12
14
16
18
20
Engineering Strain (%)

(a)

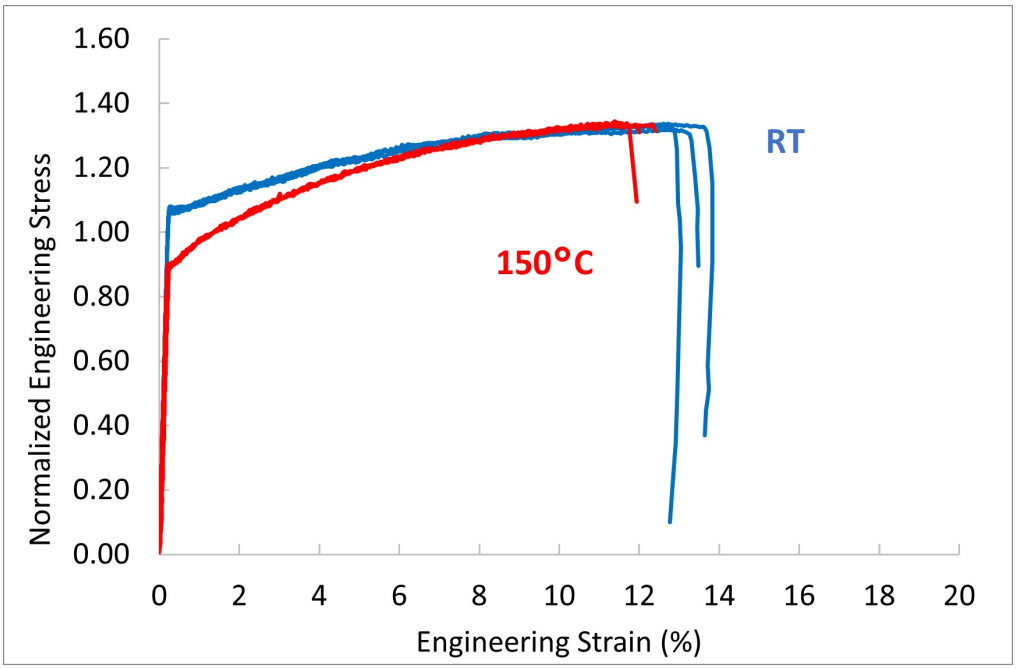
1.60
1.40
1.20
1.00
0.80
0.60
0.40
0.20
0.00
Normalized Engineering Stress
RT
150°C
0
2
4
6
8
10
12
14
16
18
20
Engineering Strain (%)

(b)

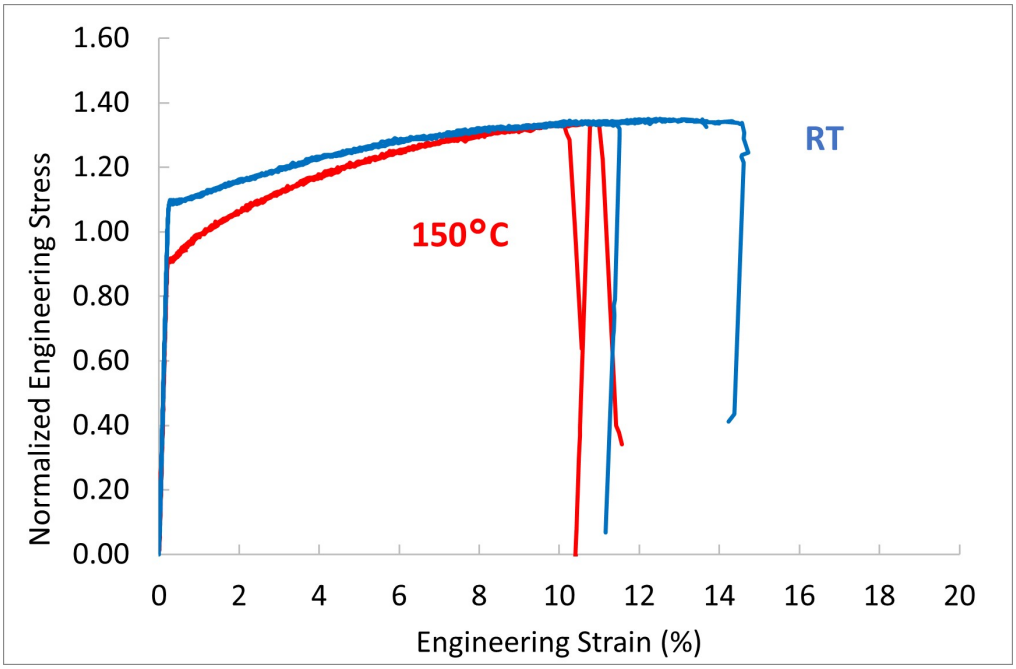

(c)

Figure 6.15: *Comparison of the stress-strain curves at RT and 150° C at (a) Rolling Direction (b)45° Orientation (c)Transverse Direction*

6.2 Chapter Conclusion

This chapter investigated the tensile properties of the three grades of electrical steel at 150°C as well as the surface of the fractured 27PNX1350F specimens to identify its deformation mechanisms. To further categorize, these steel sheets, the effect of temperature on the tensile properties were explored along the three different directions. The following conclusions can be drawn.

- The three grades of non-oriented electrical steel sheets each had similar tensile properties at an elevated temperature of 150°C along the rolling and transverse directions.
- The 20SW1200 remained the most isotropic in terms of its tensile properties out of all

three grades of non-oriented electrical steel sheets tested.

- Sheet thickness does not affect the tensile properties at an elevated temperature of 150°C.

- The fracture surface of the 27PNX1350F specimens were similar to their counterparts at room temperature which displayed significant local necking evidenced by a thinning of the specimens around the fracture region.

- The general effect of temperature on the tensile properties of non-oriented electrical steel sheets was a reduction in the strength and the elongation of the sheets.

Chapter 7

Fatigue Properties of Non-Oriented Electrical Steel Sheets at Room Temperature

Cyclic tests were conducted on non-oriented electrical steel sheets to categorize their fatigue properties at room temperature. After the cyclic tests were completed, the fracture surfaces were studied to characterize the fracture mechanisms present under this loading condition. The results of this study are presented in this chapter.

7.1 Results and Discussion

7.1.1 *27PNX1350F*

Fatigue Properties

In total, 17 cyclic tests were performed, two of which were run-outs (indicated by arrows). The normalized stress-life (S-N) curve for the tests are displayed in Figure 7.1. The shape of the stress-life curve is linear within the range of lives tested with relatively high lives close even when the stress amplitude was close to the yield strength which was consistent with the results from the fatigue tests performed by Bode et al. and Lakkonavar et al. [2, 19].

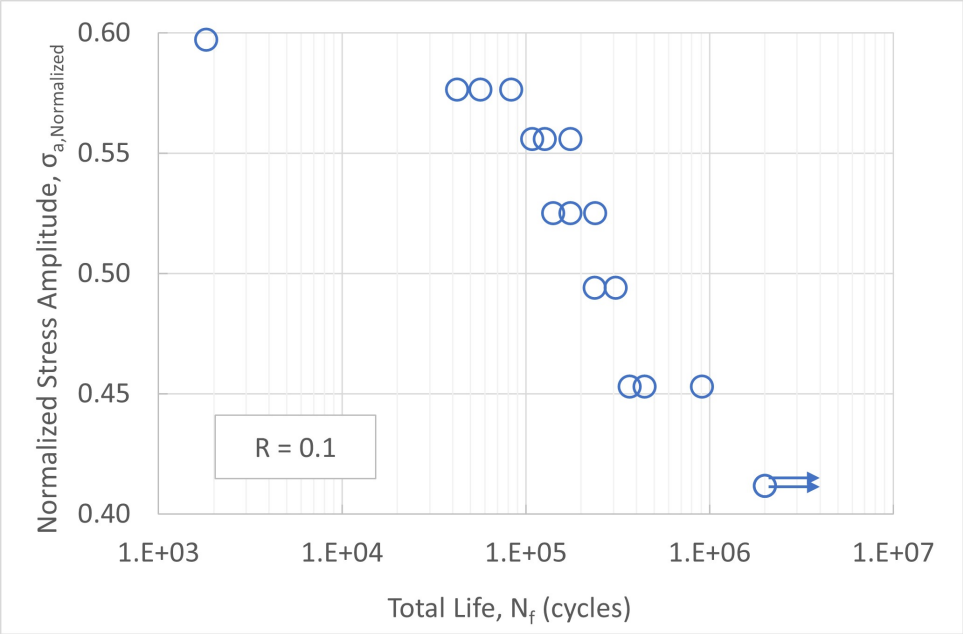

Figure 7.1: *Stress Life Curve for 27PNX1350F at R=0.1*

Since the tests were performed with a mean stress present, a correction must be applied and as such using the Smith-Watson-Topper method (SWT) [53] (see Equation 7.1), the equivalent fully reversed stress amplitudes (σ_{ar}) at R=-1 were obtained and the corrected

S-N curve was generated, which is shown in Figure 7.2. This method accounts for the mean stress (σ_m) by taking into account the stress amplitude (σ_a) and the maximum stress (σ_{max}) tested.

$$\sigma_{ar} = \sqrt{\sigma_{max} * \sigma_a} \tag{7.1}$$

where $\sigma_{max} = \sigma_m + \sigma_a$.

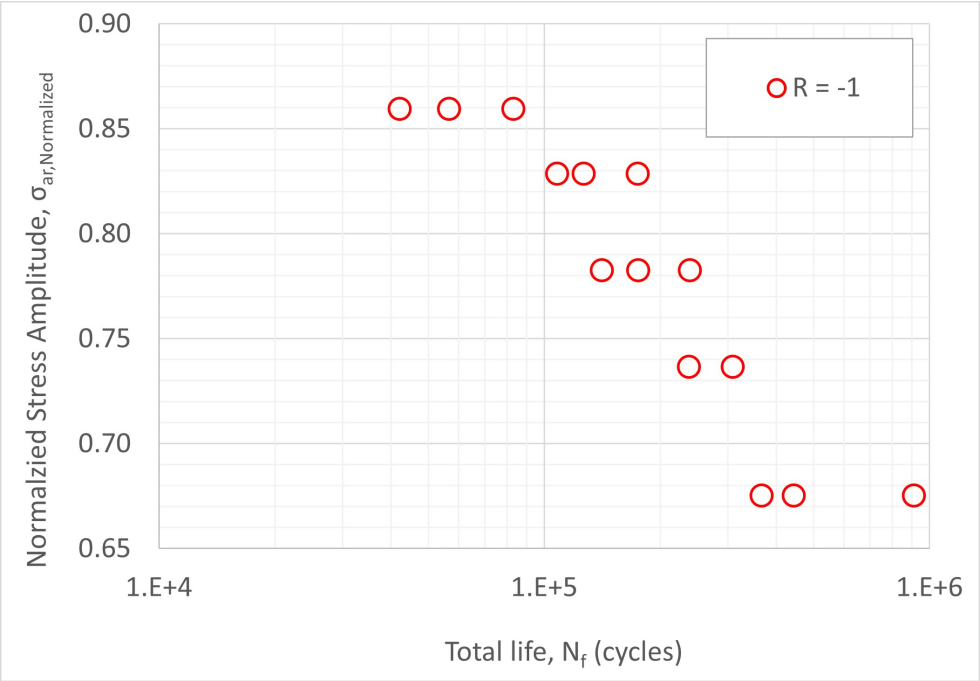

Figure 7.2: *Linear region of the Stress Life Curve for 27PNX1350F at R=-1*

The Basquin model, $\sigma_{ar} = \sigma_f(2N_f)^b$, was fitted to the fully reversed S-N curve and the model parameters (σ_f and b) were obtained from linear regression as well as generating a design curve with a reliability of 90% and a confidence level of 90% using the Owen's tolerance limit method [69]. Owen's method shifts the fully reversed S-N curve by an amount dependent on the reliability and confidence level but preserves the slope of the curve (see Figure. 7.3). The details of this method are given by Shen et al. [69]. The design curve fatigue

parameters ($\sigma_{f,RC}$ and b) were found from the Basquin model and Owen's method. The fatigue parameters normalized by the average yield strength for both curves are given in Table.7.1

Table 7.1: Normalized Fatigue Parameters for 27PNX1350F

Fatigue	$\sigma'_{f,Normalized}$	$\sigma'_{f,RC,Normalized}$	b
Parameters	3.62	3.33	-0.120

Figure 7.3: *Fully Reversed and Design S-N Curves for 27PNX1350F*

Fracture Analysis

For the cyclic tested specimens, crack was determined to initiate from one edge of the sample and then propagate to the other (see Figure 7.4a). Fatigue damage, evidenced by fatigue

stair lines can be seen in Figure 7.4b. The region of fatigue damage was measured to be between 1mm to 2.4mm with samples tested at low load levels and high fatigue lives having longer regions of fatigue damage (see Figure. 7.5. After the region of fatigue damage, the rest of the specimen failed by brittle fracture evidenced by cleavage facets on the fracture surface (see Figure 7.6). Investigating the fracture surface reveals that the fracture was of a transgranular nature since the crack propagated through and broke the grains rather than at grain boundaries. Thus, the fracture surface can in general be divided into two zones as shown in Figure. 7.7; zone A where fatigue damage is present and includes crack initiation and propagation, and zone B that is characterized by the brittle failure of the specimen as was also seen by Bode et al. [19].

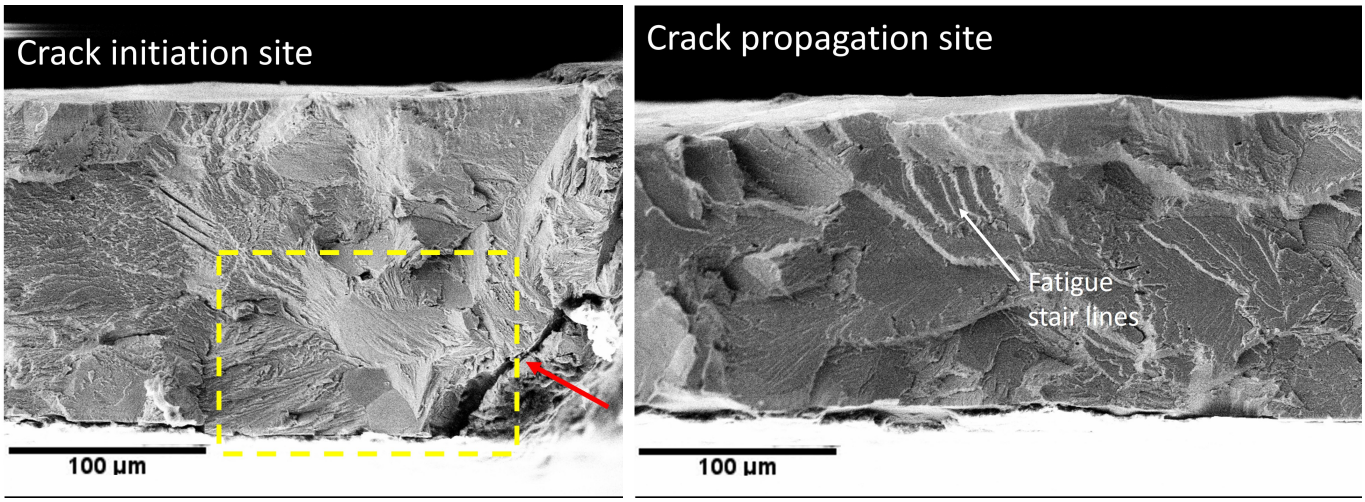

(a) (b)

Figure 7.4: *SEM images showing (a) Crack Initiation Site (b)Fatigue Stair lines*

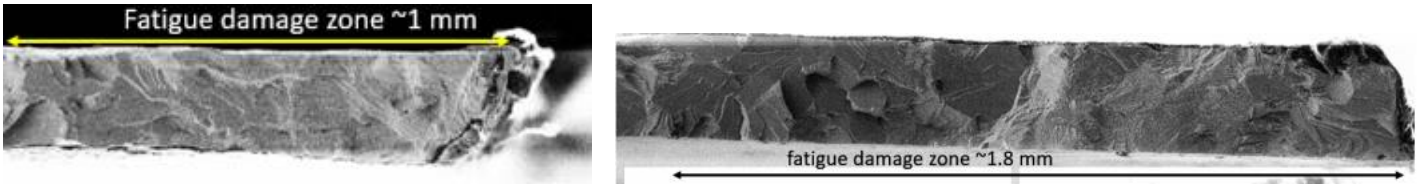

(a) (b)

Figure 7.5: *SEM images showing the fatigue damages zones for specimens with (a) 20,560 total life (b)148,650 total life*

Figure 7.6: *SEM image showing region of brittle fracture characterized by cleavage facets on the fracture surface*

Figure 7.7: *Fracture Surface of across the width of the specimen showing the region of ductile crack propagation and brittle fracture*

Furthermore, precipitate particles were also detected on the fracture surface (shown in Figure. 7.8a). Using energy dispersive X-ray spectroscopy (EDX), the particles were confirmed to be Aluminium Nitride (see Figure. 7.8b).

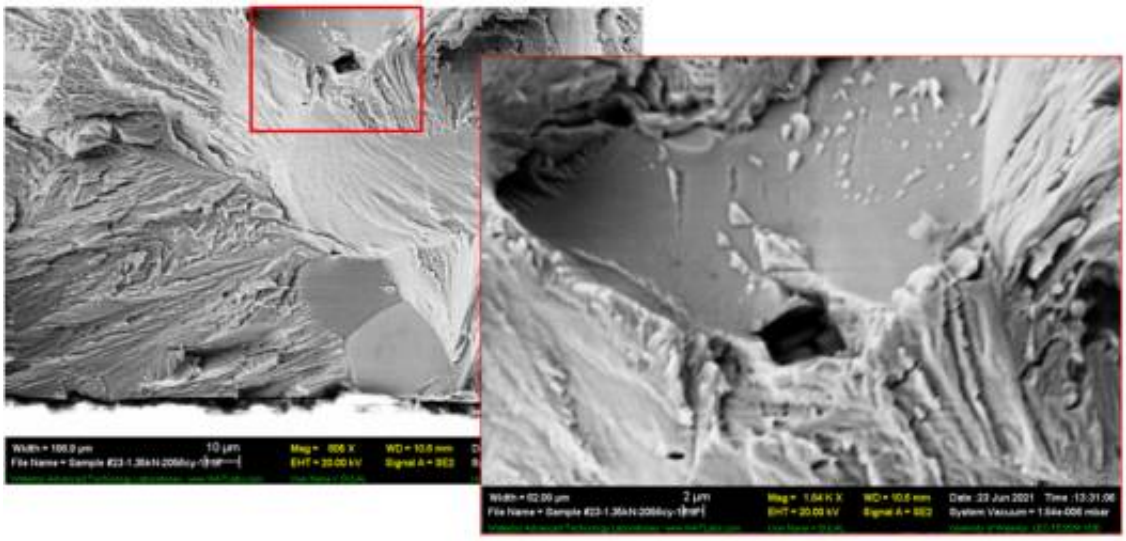

(a)

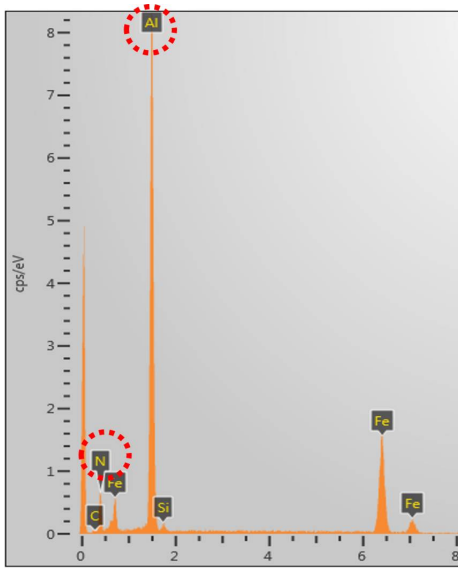

(b)

Figure 7.8: *Images showing (a) Angular holes on fracture surface (b)EDX analysis of angular hole*

7.1.2 *25SW1250*

Fatigue Properties

A total of 28 cyclic tests across 6 major load levels were performed, two of which were run-outs (indicated by arrows). The normalized stress-life (S-N) curve for the tests are displayed in Figure 7.9a. The shape of the S-N curve is linear within the range of fatigue lives tested. Using the Smith-Watson-Topper method (SWT) [53] (see Equation 7.1), the equivalent fully reversed stress amplitudes (σ_{ar}) at R=-1 were obtained and the corrected S-N curve was generated, which is shown in Figure 7.9b

The Basquin model, $\sigma_{ar} = \sigma_f(2N_f)^b$, was fitted to the linear fully reversed S-N curve and the model parameters (σ_f and b) were obtained from linear regression as well as generating a design curve with a reliability of 90% and a confidence level of 90% using the Owen's tolerance limit method [69] (see Figure 7.3). The design curve fatigue parameters ($\sigma_{f,RC}$ and b) were found from the Basquin model and Owen's method. The fatigue parameters normalized by the average yield strength for both curves are given in Table 7.2.

Table 7.2: Normalized Fatigue Parameters for 25SW1250

Fatigue	$\sigma'_{f,Normalized}$	$\sigma'_{f,RC,Normalized}$	b
Parameters	1.41	1.30	-0.05

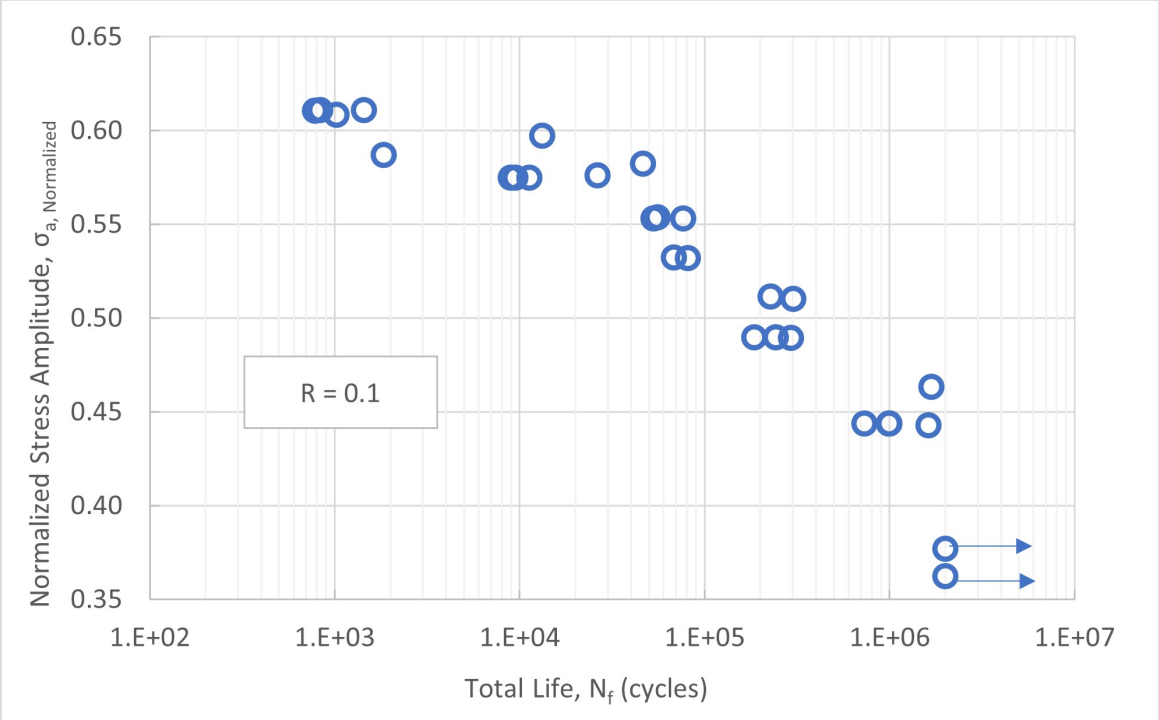

(a) *Stress Life Curve at R=0.1*

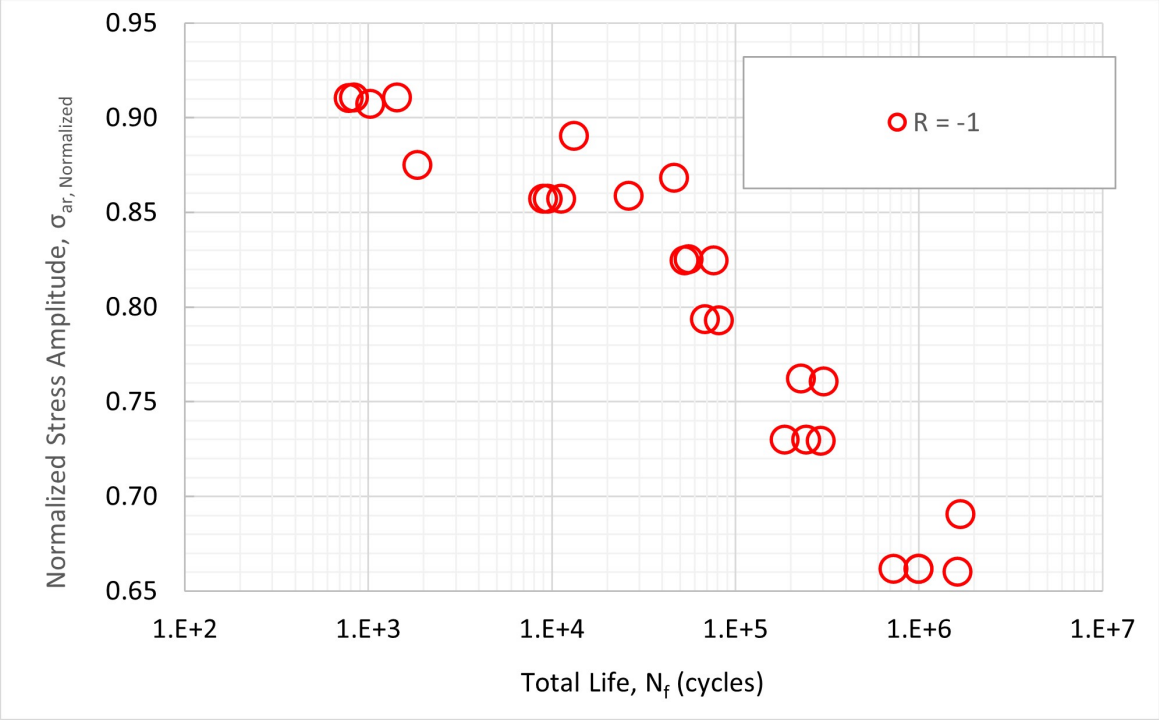

(b) *Stress Life Curve for 25SW1250 at R=-1*

Figure 7.9: Stress Life curves for 25SW1250

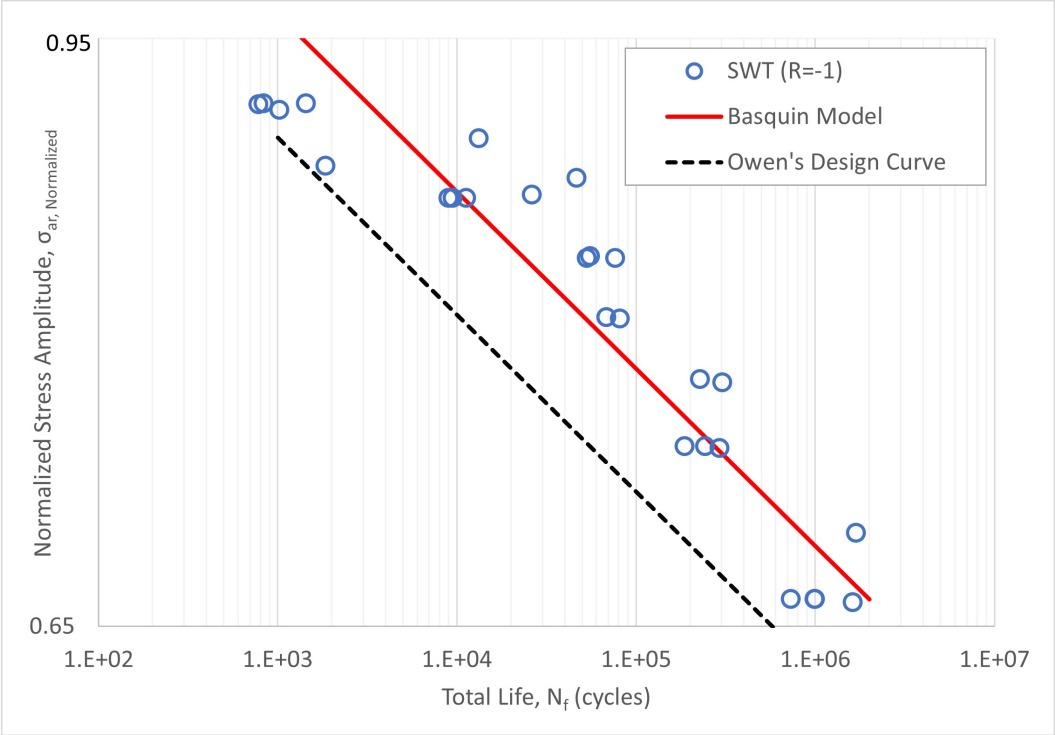

Figure 7.10: *Fully Reversed and Design S-N Curves for 25SW1250*

Fracture Analysis

The fracture surface of this grade showed very similar features to that of the 27PNX1350F grade. The crack was determined to have initiated from one edge and propagated to the other. For specimens in the low cycle regime ($N_f < 5\text{x}10^3$ cycles), the fracture surface showed only cleavage facets from the sudden transgranular fracture of the grains with no signs of fatigue damage (see Figure 7.11) while the immediate region after the crack initiation site for specimens with medium to high cycle fatigue life ($N_f > 10^4$ cycles) showed signs of fatigue damage (stair lines shown in Figure 7.12). The length of the region of fatigue damage was also observed to increase with increasing fatigue life (see Figure 7.13). As shown in Figure 7.12), after the region of fatigue damage, the fracture surface was characterized by

cleavage facets from the transgranular fracture of the grains. Furthermore, as shown in Figure 7.14), investigating the region around the fracture surface revealed the presence of plastic deformation accommodation mechanisms such as deformation twins as well as the presence of transgranular secondary cracks which increased in quantity as the fatigue life increased.

Figure 7.11: *Typical fracture surface for low cycle Fatigue life specimens.*

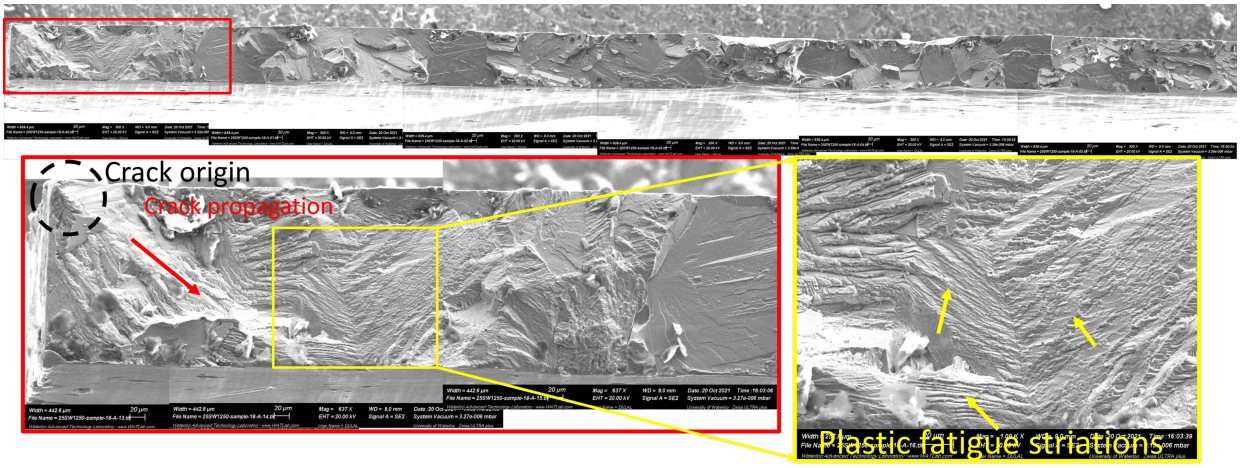

Figure 7.12: *Typical fracture surface for medium to high cycle fatigue life specimens.*

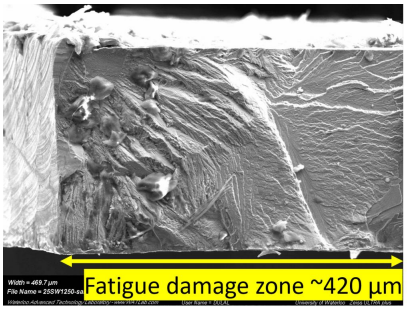

(a)

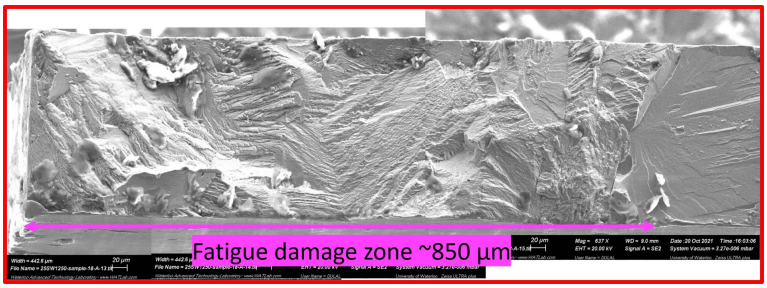

(b)

Figure 7.13: SEM images showing the fatigue damages zones for specimens with (a) 11,232 total life (b) 81, 254total life.

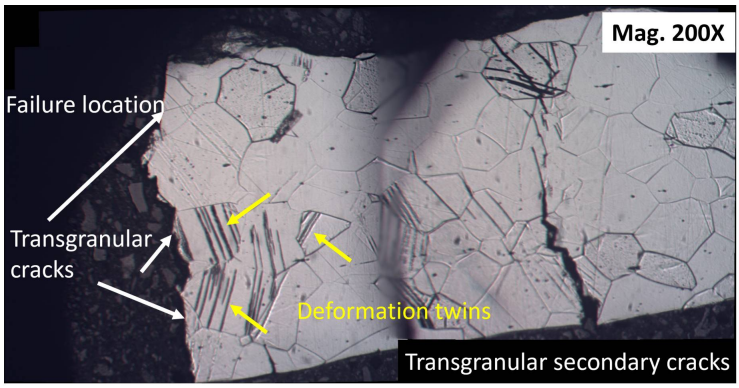

Figure 7.14: *Typical microstructure surrounding the fatigue fracture region.*

7.1.3 *20SW1200*

Fatigue Properties

Very limited cyclic tests were performed for this grade of non-oriented electrical steel sheet. In total 10 cyclic tests were performed with only one of those tests being run-out (indicated by an arrow). The other 9 tests were performed at three selected load levels with three repetitions each to cover a range of fatigue lives. The normalized stress-life (S-N) curve for the tests are displayed in Figure 7.15. The shape of the stress-life curve is seemingly

linear within the range of fatigue lives tested. For this grade, statistical analysis such as the equivalent fully reversed stress amplitude and design curves were not obtained because of the limited tests performed.

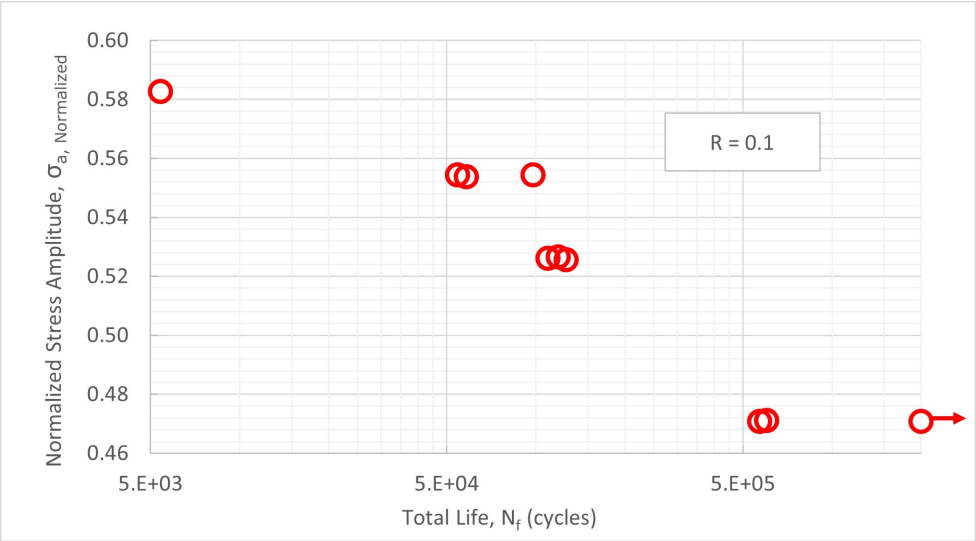

Figure 7.15: *Stress Life Curve for 20SW1200 at R=0.1*

7.1.4 Discussion

The S-N curves for all three grades of non-oriented electrical steel sheets tested at R=0.1 and R=-1 has been shown in Figure 7.16. From the figures, the fatigue lives and shape of the stress-life curves of all three grades are very similar at the same stress amplitudes and as such, the conclusion that the sheet thickness does not have an effect on the fatigue life can be drawn.

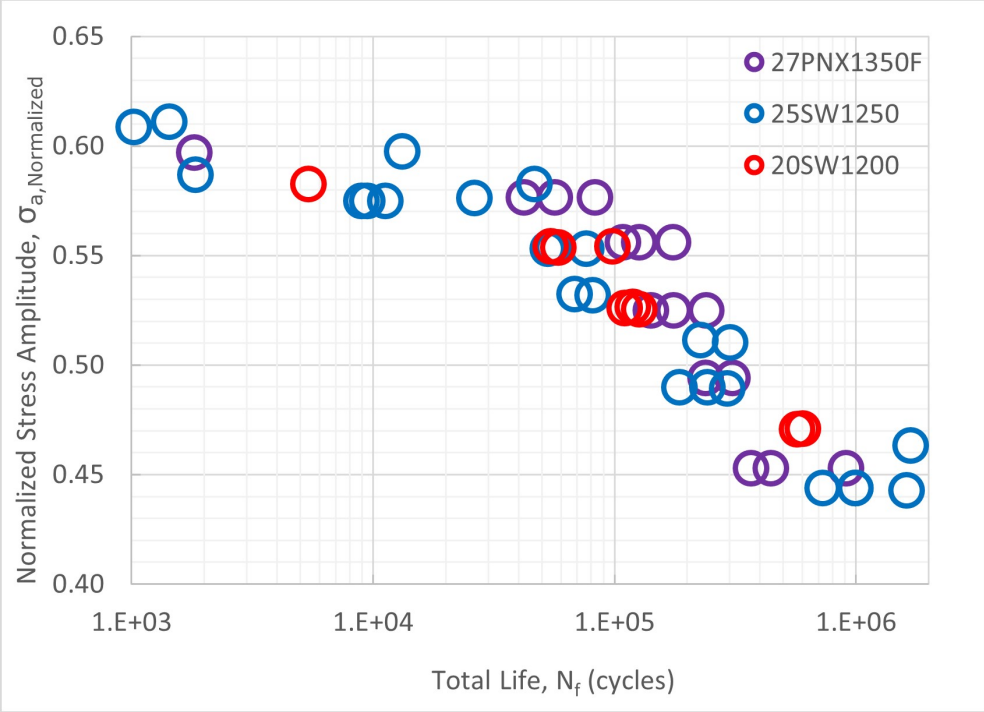

(a)

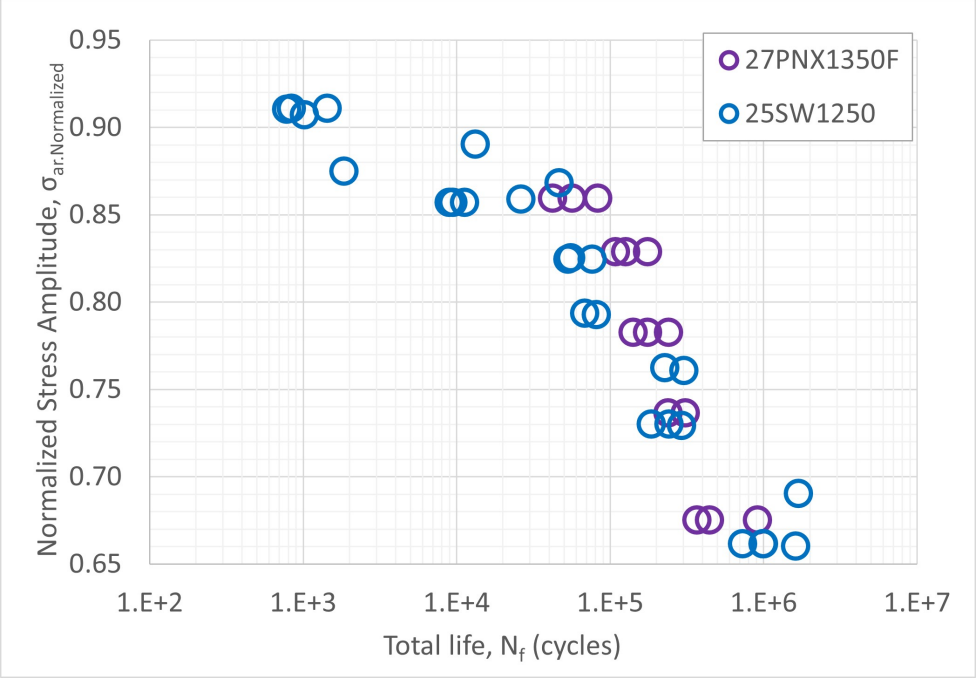

(b)

Figure 7.16: Stress-Life curves comparison at (a) R=0.1 (b) R=-1

7.2 Chapter Conclusion

This chapter investigated the fatigue properties and analyzed the fracture surface of the 27PNX1350F and 25SW1250 grades of non-oriented electrical steel sheet as well as performing limited cyclic tests on the 20SW1200 grade to investigate the effect of thickness on the fatigue properties. The following conclusions can be drawn.

- The S-N curves were linear within the range of fatigue lives tested.
- The sheet thickness does not have an effect on the fatigue life of the non-oriented electrical steel sheets.
- The general fracture mode is a mixed mode of cyclic deformation and transgranular cleavage fracture.

Chapter 8

Fatigue Properties of Non-Oriented Electrical Steel Sheets at an Elevated Temperature of 150°C

Since in its application the electric motor will be operating under a range temperatures from room to elevated temperatures, it is necessary to categorize the fatigue properties at an elevated temperature and as such, cyclic tests were conducted non-oriented electrical steel sheets at 150°C. The purpose of these cyclic tests was to categorize the fatigue properties of non-oriented electrical steel sheets at an elevated temperature. After the cyclic tests were completed, the fracture surfaces were studied to characterize the fracture mechanisms present under this loading condition. The results of this study are presented in this chapter.

8.1 Results and Discussion

8.1.1 *27PNX1350F*

Fatigue Properties

In total, 27 cyclic tests were performed, two of which were run-outs (indicated by arrows). The normalized stress-life (S-N) curve for the tests are displayed in Figure 8.1a. The shape of the S-N curve is linear within the range of fatigue lives tested. Using the Smith-Watson-Topper method (SWT) [53] (see Equation 7.1), the equivalent fully reversed stress amplitudes (σ_{ar}) at R=-1 were obtained and the corrected S-N curve was generated, which is shown in Figure 8.1b

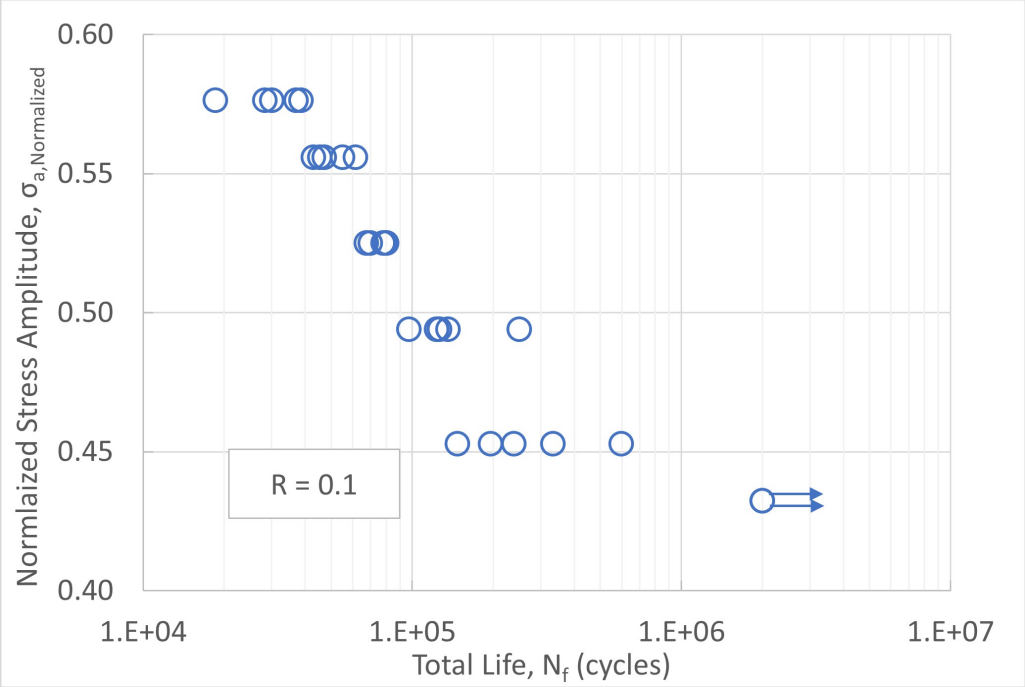

(a) *Stress Life Curve at R=0.1*

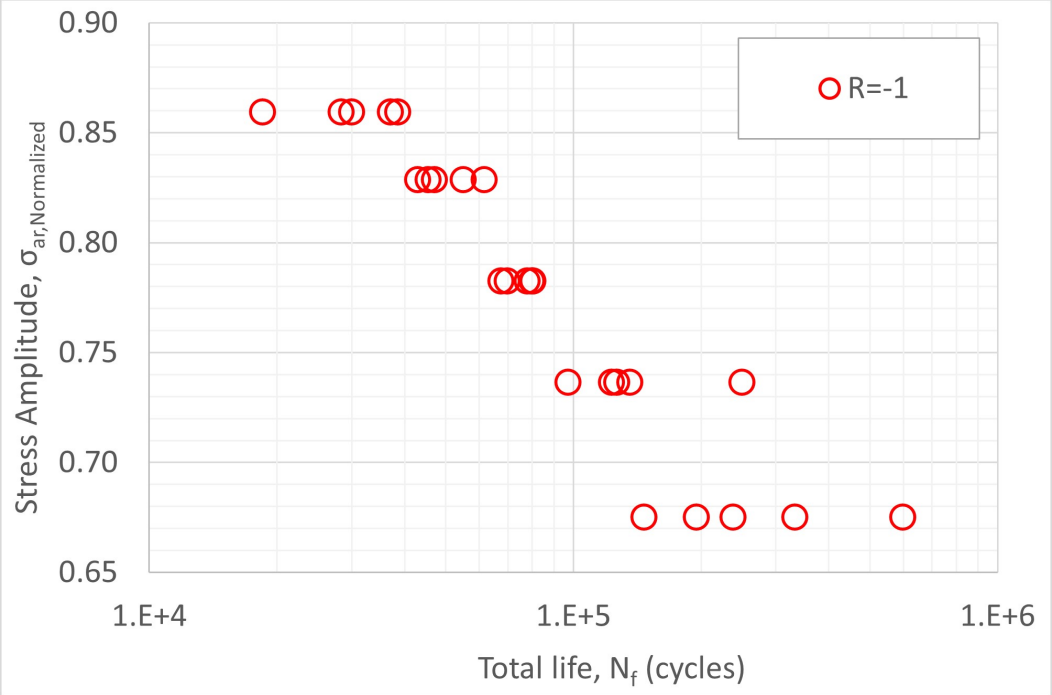

(b) *Stress Life Curve at R=-1*

Figure 8.1: Stress Life curves for 27PNX1350F at 150°C

The Basquin model, $\sigma_{ar} = \sigma_f(2N_f)^b$, was fitted to the linear fully reversed S-N curve and the model parameters (σ_f and b) were obtained from linear regression as well as generating a design curve with a reliability of 90% and a confidence level of 90% using the Owen's tolerance limit method [69] (see Figure 8.2). The design curve fatigue parameters ($\sigma_{f,RC}$ and b) were found from the Basquin model and Owen's method. The fatigue parameters normalized by the average yield strength for both curves are given in Table 8.1.

Table 8.1: Normalized Fatigue Parameters for 27PNX1350F at 150°C

Fatigue	$\sigma'_{f,Normalized}$	$\sigma'_{f,RC,Normalized}$	b
Parameters	2.98	2.80	-0.112

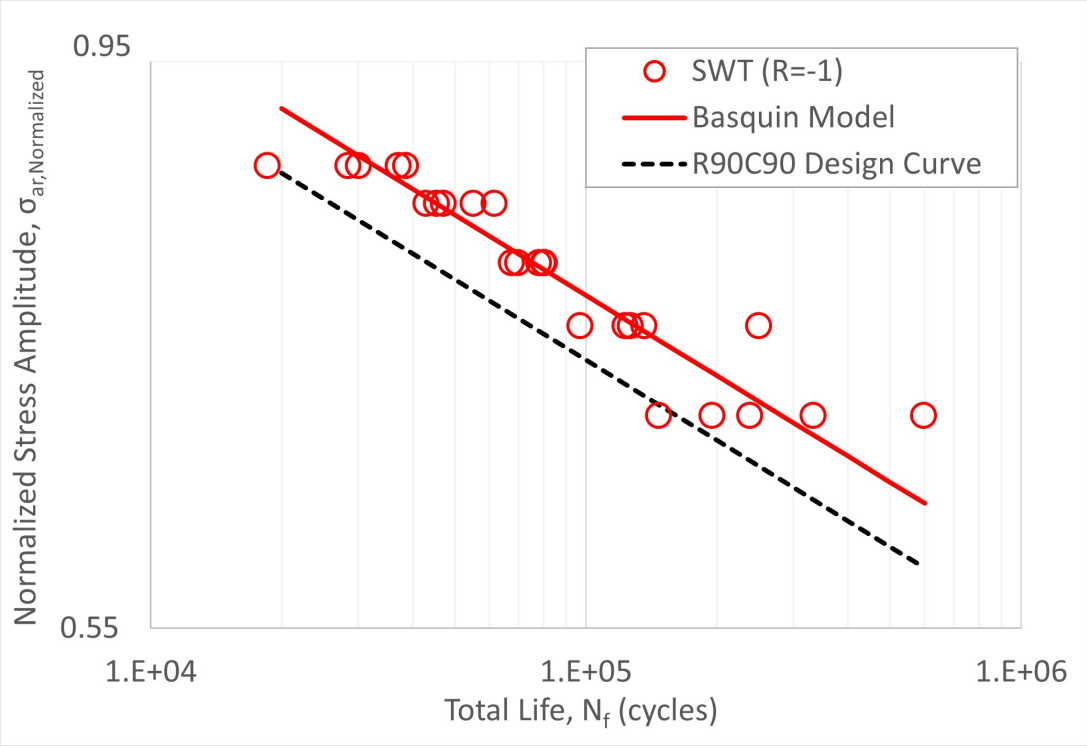

Figure 8.2: *Fully Reversed and Design S-N Curves for 27PNX1350F at 150°C*

Fracture Analysis

The fracture surface for the cyclic tested specimens at 150°C was characterized by cone-like failure of the grains after the crack initiation and propagation region (see Figure 8.3). The region of fatigue deformation was observed to increase with increasing fatigue lives. Similar to the room temperature analysis, this divides the fracture surface into two regions; the first region is characterized by transgranular failure of the grains with fatigue striations (see Figure 8.4) which signifies fatigue damage whereas, the second region was characterized by a more ductile mode of failure. This cone-like fracture is indicative of the local necking caused by severe thinning of the specimen from both sides during testing.

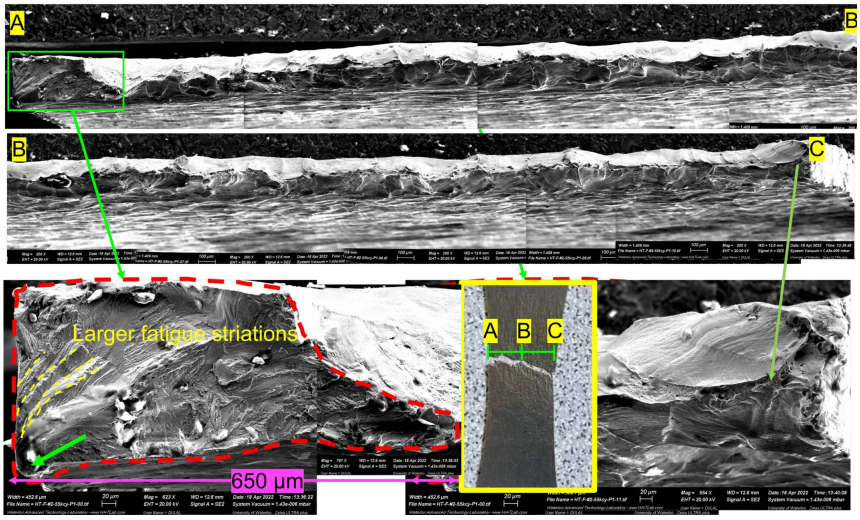

Figure 8.3: *Typical fracture surface for cyclic tested 27PNX1350F at 150° C*

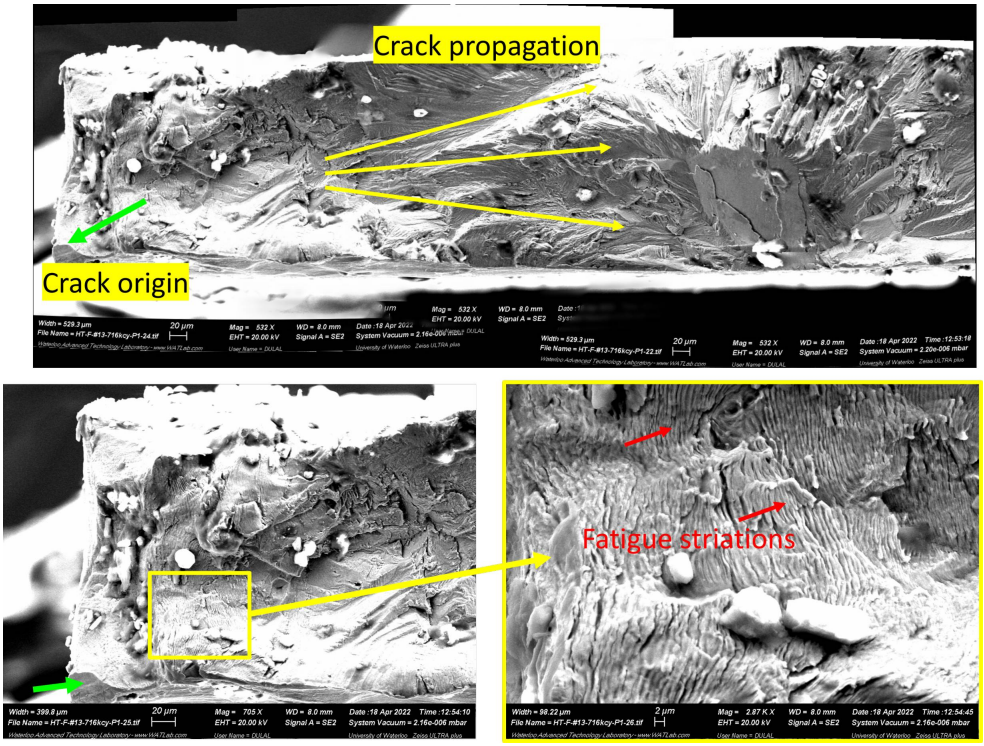

Figure 8.4: *SEM Image showing the crack initiation and propagation region*

8.1.2 *Effect of Temperature on the Fatigue Properties of Electrical Steel Sheets*

A comparison between the stress-life curve at room temperature (RT) and 150°C (HT) is shown in Figure 8.5 and the Table 8.2 gives a comparison between the normalized fatigue parameters. From the figure, there is a noticeably slight difference in the fatigue lives at room temperature and 150°C. The effect of temperature would be a slight but noticeable reduction in the fatigue life of non-oriented electrical steel sheets at increased temperature. Also comparing Figures 7.7 and 8.3, the fracture surfaces at the two temperatures have different final fracture mechanisms. While the room temperature surface finally failed by cleavage transgranular fracture of the grains, the specimens at 150°C failed by ductile cone-like fracture of the grains.

Table 8.2: Comparison of the Normalized Fatigue Parameters at Room Temperature and 150°C

Fatigue Parameters	RT	HT
$\sigma'_{f,Normalized}$	3.62	2.98
b	-0.120	-0.112

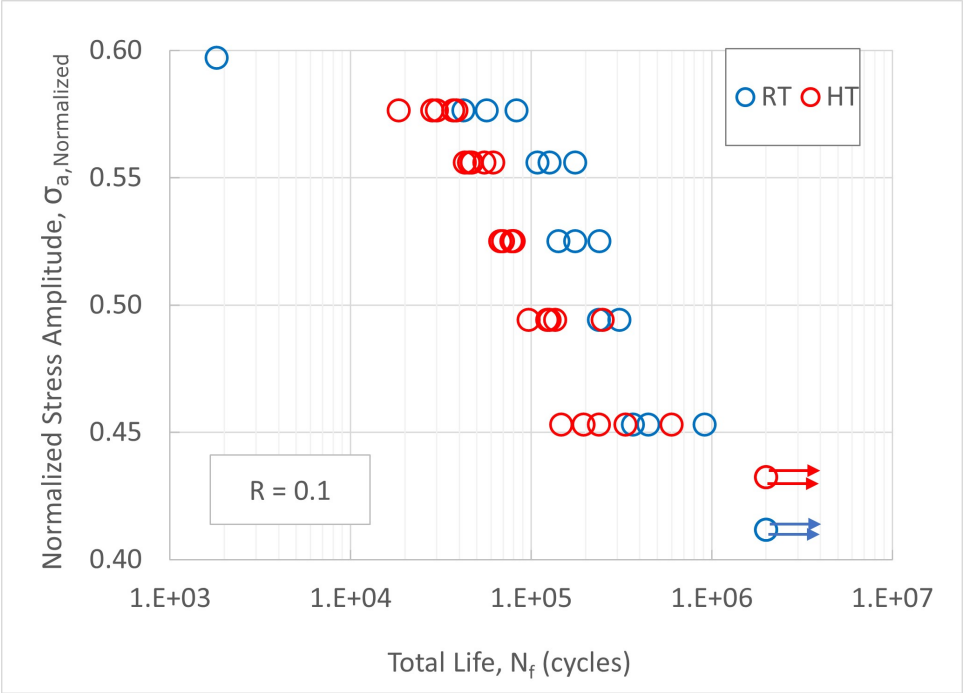

(a)

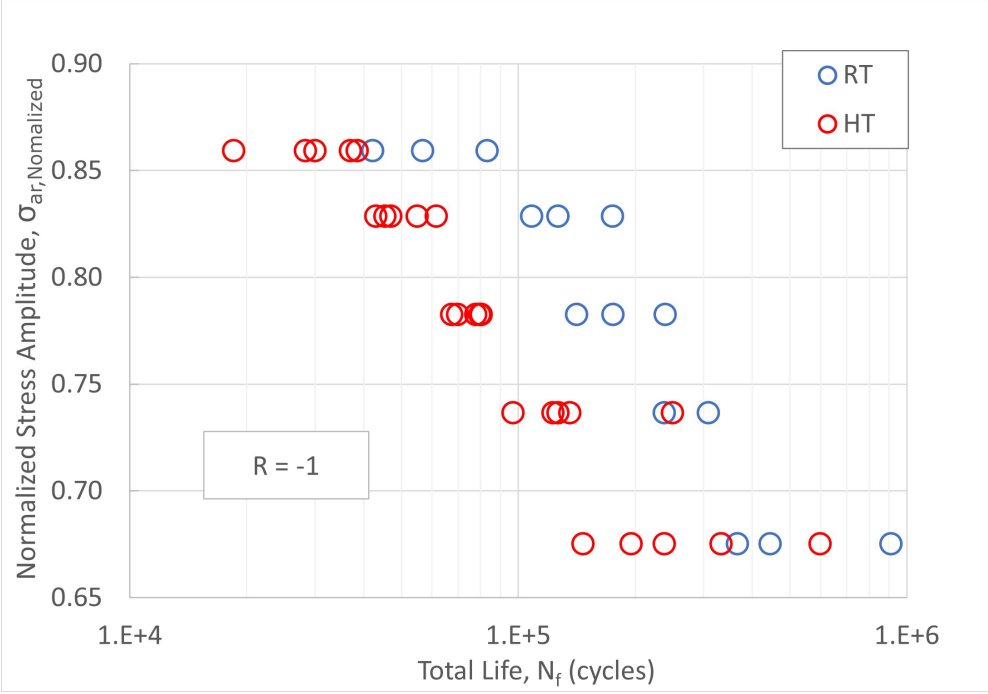

(b)

Figure 8.5: Comparison of the stress-life Curve at RT and 150°C at (a) R=0.1 (b) R=-1

8.2 Chapter Conclusion

This chapter investigated the fatigue properties of non-oriented electrical steel sheets at 150°C and analyzed the fracture surface of the fractured specimens. The effect of temperature on the fatigue life of non-oriented electrical steel sheets were also explored. The two following conclusions can be drawn.

- Increasing the temperature causes a noticeable but slight reduction in the fatigue life at 150°C.
- The fracture surface at 150°C was characterized by a mixture of transgranular crack propagation and final ductile cone-like fracture.

Chapter 9

Effect of Cutting Method and Mean Stress on the Fatigue Life of Non-Oriented Electrical Steel Sheets

In this chapter, the effect of mean stress and cutting method on the fatigue life of non-oriented electrical steel sheets will be presented.

9.1 Results and Discussion

9.1.1 *27PNX1350F*

Fatigue Properties

A total of 47 cyclic tests were performed to cover a range of load and fatigue life levels. Thirty-four of those tests were performed at an R=0.1 while nine tests were performed at an

R=0.3 and the remaining four tests were performed at an R=0.5. Six run-out tests (indicated by arrows) were recorded for the R=0.1 tests while none were recorded for the tests at other R-ratios. The normalized stress-life (S-N) curve for the tests are displayed in Figure 9.1 below as well as the normalized curve for stress amplitude vs 1mm crack initiation life. The shape of the stress-life curve can be divided into three distinct regions by their slopes: the linear section in the middle ($10^5 < N_f < 10^6$ cycles) and two seemingly flat sections at both ends ($N_f < 10^5$ and $N_f > 10^6$ cycles). Ideally, the three regions should be modeled by three equations. However, for this analysis, only the linear portion is of interest and has been modeled.

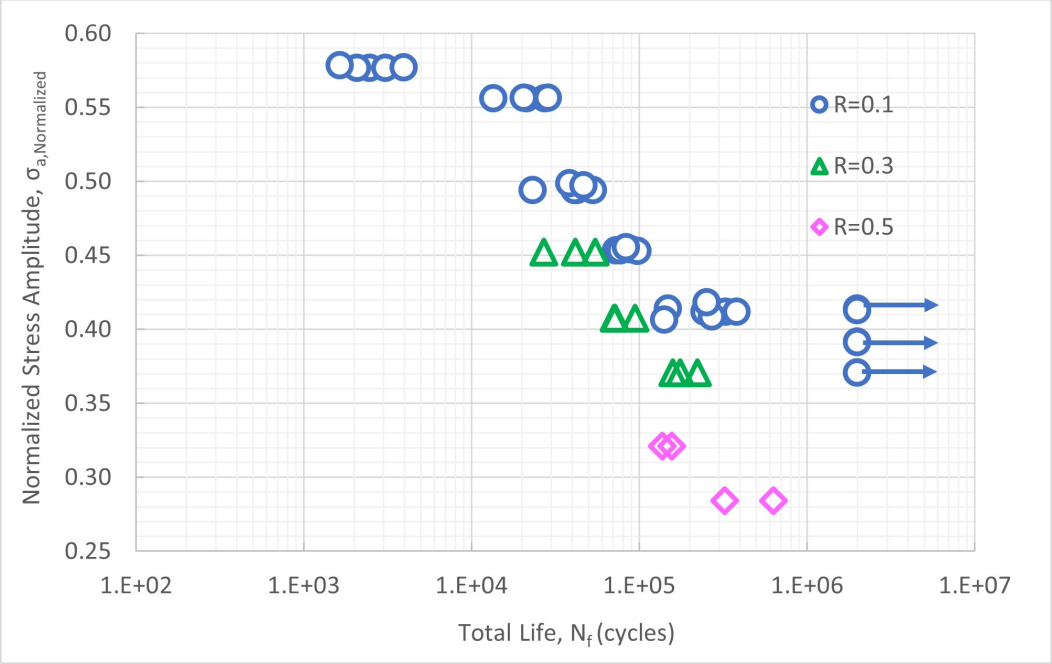

(a)

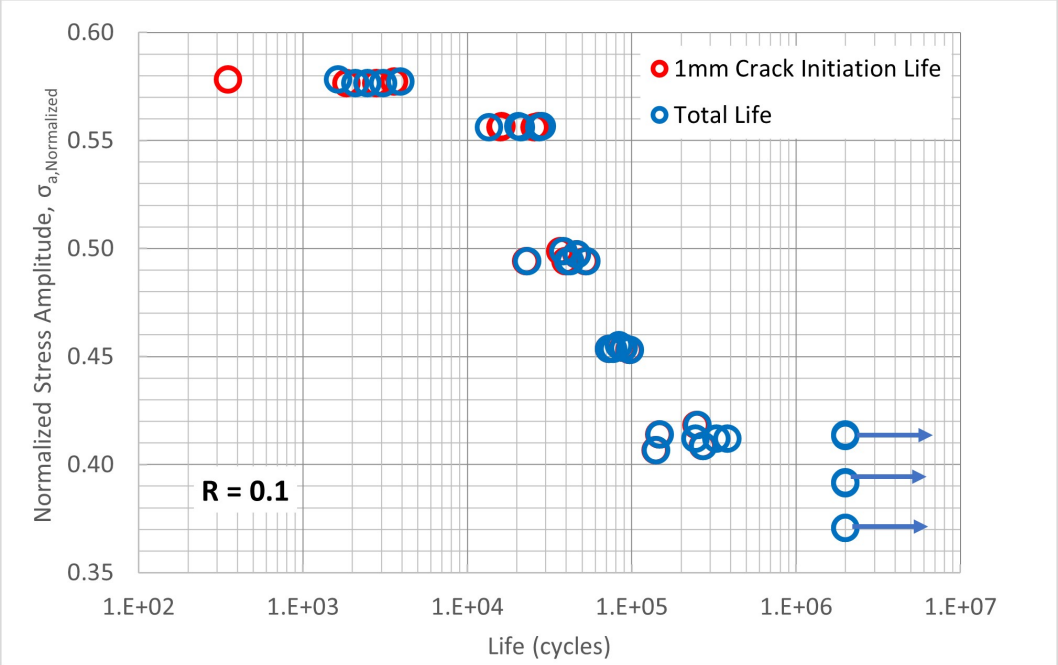

(b)

Figure 9.1: Normalized stress-life curves for water-jet 27PNX1350F showing (a) tests performed at different load ratios (b) crack initiation life vs total life

The equivalent fully reversed stress amplitude was obtained using the Smith Watson Topper mean stress correction method [53] (see Equation.7.1) as well as the Walker mean stress correction method [70] (see Equation.9.1). Similar to the Smith Watson Topper (SWT) method [53], the Walker method accounts for the mean stress (σ_m) by taking into account the stress amplitude (σ_a) and the maximum stress (σ_{max}) tested. However, the Walker method [70] uses an adjustable material parameter (γ) as its exponent. The presence of this adjustable parameter allows the Walker method to be the best mean stress correction method [70]. However, the Walker material parameter is not readily available and obtaining it requires extensive testing which makes its use in engineering applications limited. In this

study, the Walker material parameter was obtained by minimizing the root mean squared value of the linear regression analysis. The normalized equivalent fully reversed stress-life curves using the SWT method and Walker method were both plotted and given in Figure 9.2.

$$\sigma_{ar} = \sigma_{max}^{1-\gamma} * \sigma_a^{\gamma} \tag{9.1}$$

where $\sigma_{max} = \sigma_m + \sigma_a$.

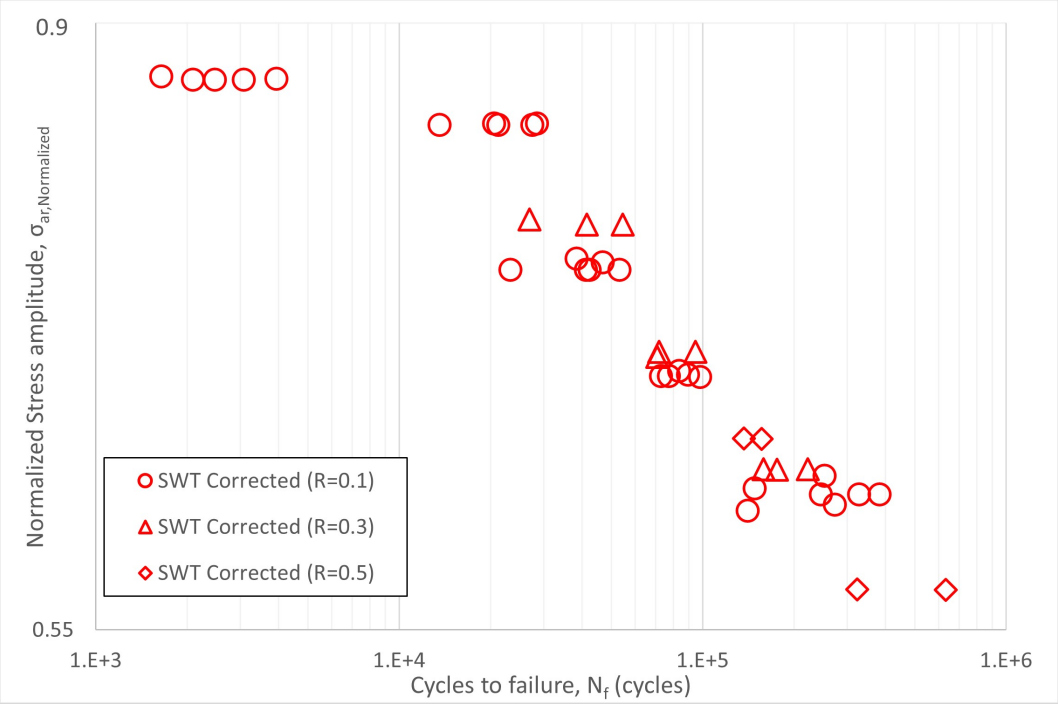

(a)

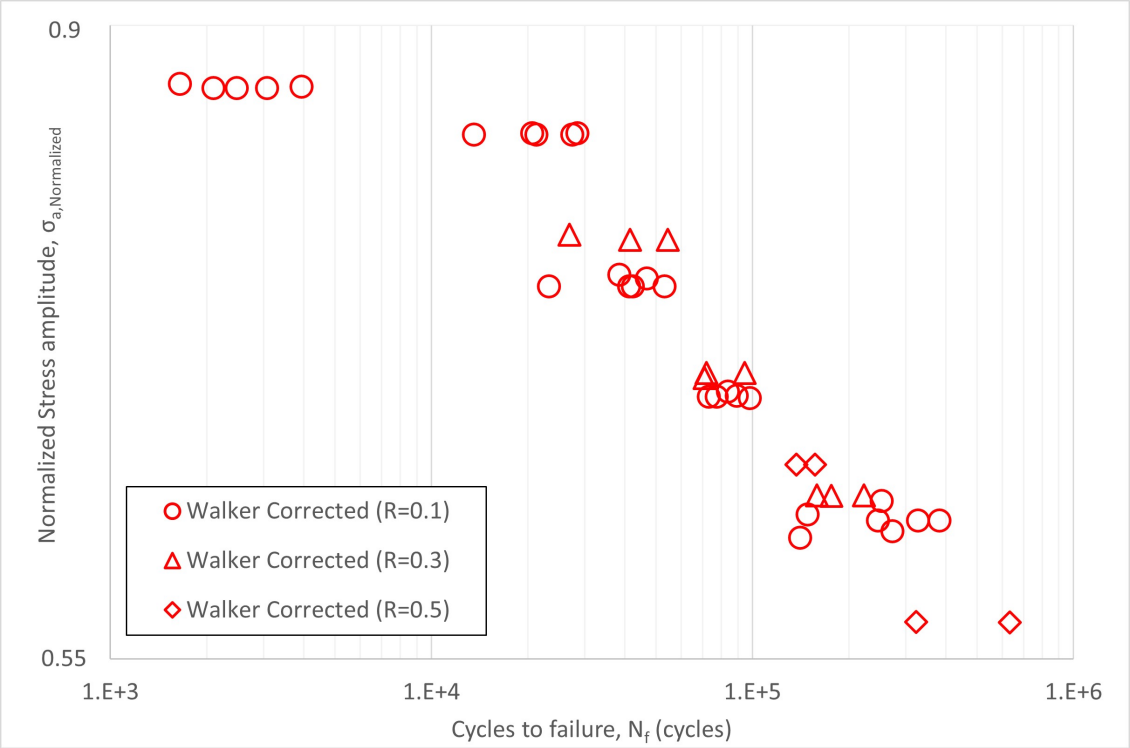

(b)

Figure 9.2: Normalized fully reversed stress-life curves using the (a) Smith Watson Topper Mean Stress Correction Method (b) Walker Mean Stress Correction Method for Water-Jet cut 27PNX1350F specimens

The Basquin model, $\sigma_{ar} = \sigma_f(2N_f)^b$, was fitted to the linear fully reversed S-N curve and the model parameters (σ_f and b) were obtained from linear regression as well as generating a design curve with a reliability of 90% and a confidence level of 90% using the Owen's tolerance limit method [69] (see Figure 9.3). The design curve fatigue parameters ($\sigma_{f,RC}$ and b) were found from the Basquin model and Owen's method. The fatigue parameters normalized by the average yield strength for both curves and mean stress correction methods are given in Table 9.1 and 9.2 respectively.

Table 9.1: Normalized Fatigue Parameters for Water-Jet cut 27PNX1350F using the SWT Correction Method

Fatigue	$\sigma'_{f,Normalized}$	$\sigma'_{f,RC,Normalized}$	b
Parameters	2.09	1.92	-0.094

Table 9.2: Normalized Fatigue Parameters for Water-Jet cut 27PNX1350F using the Walker Correction Method

Fatigue	$\sigma'_{f,Normalized}$	$\sigma'_{f,RC,Normalized}$	b	γ
Parameters	2.09	1.92	-0.094	0.503

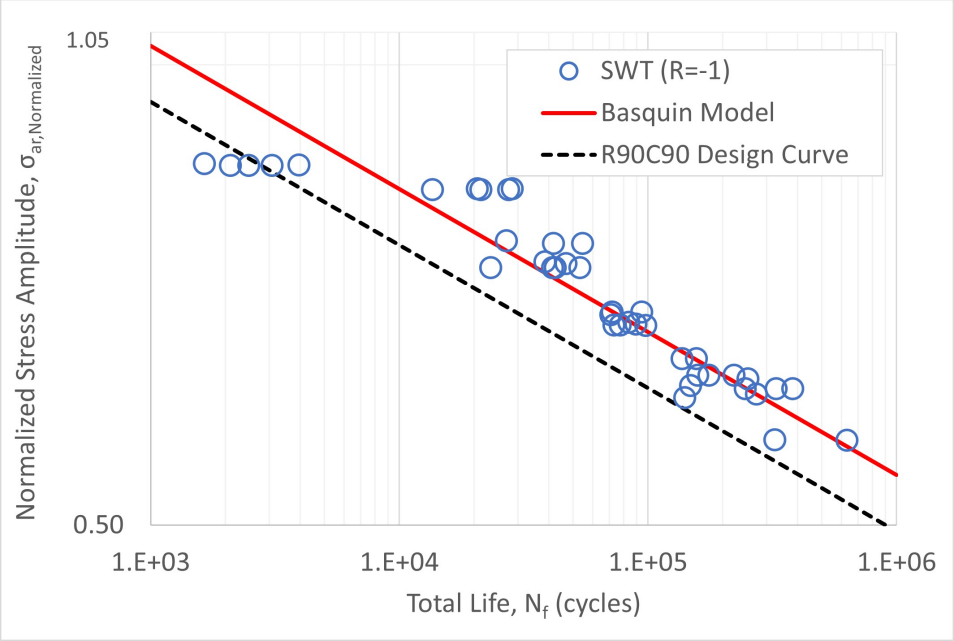

(a)

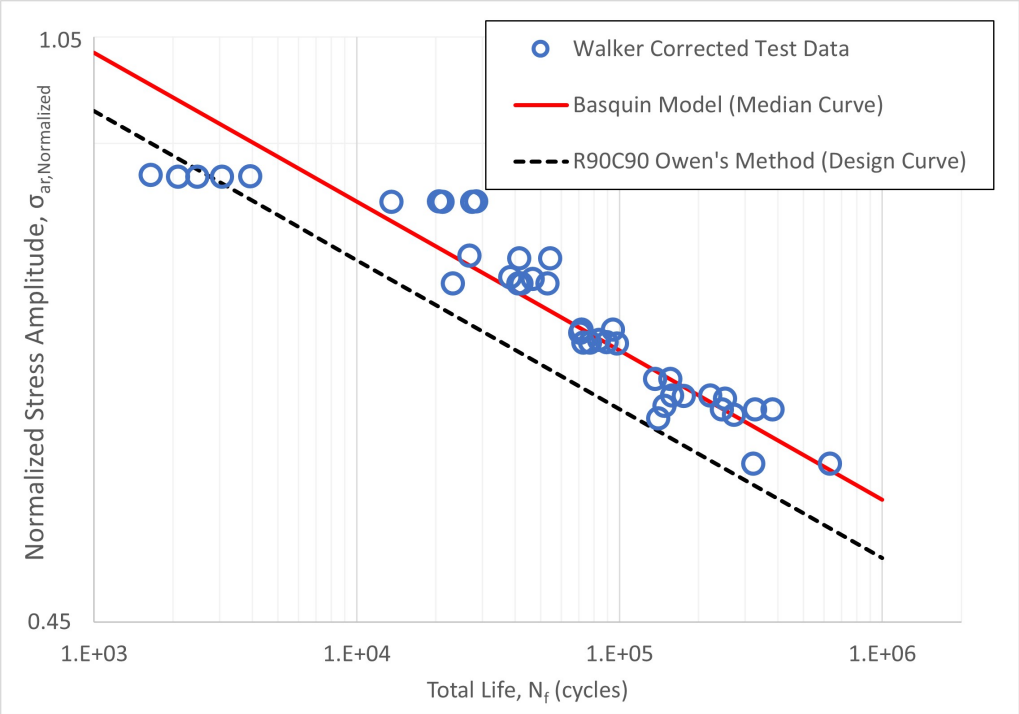

(b)

Figure 9.3: Normalized fully reversed and design S-N curves using the (a) SWT Method (b) Walker method

9.1.2 Discussion

Effect of Mean Stress on the Fatigue Life of Electrical Steel Sheets

From Figure 9.1a, at the same stress amplitudes, the tests with higher mean stresses at R=0.3 ratios, gave lives within the scatter range of the tests at R=0.1. The tests show the beginning of a trend of the effect of mean stress on the fatigue life Although not conclusively, the mean stress seems to have an effect on the fatigue life the nature of which may be the focus of a future study. Also, the tests performed at R=0.3 and R=0.5 gave finite lives

below the stress amplitude for which the tests at R=0.1 went to run-out. Therefore, the mean stress also decreases the stress amplitude at which the specimens will have infinite life.

Effect of Cutting Method on the Fatigue Life of Electrical Steel Sheets

The Figure 9.4 below shows a comparison between of the stress-life curves of the tests run with specimens cut from water-jet and machined with CNC method while Table 9.3 gives a comparison of the fatigue parameters. From a roughness analysis presented by Gill et al. [71] on the same specimens, the water-jet specimens were measured to have significantly rougher edges than the CNC specimens. The effect of this edge roughness can be seen in the figures presented as the CNC specimens, gave significantly improved fatigue lives over the water-jet specimens.

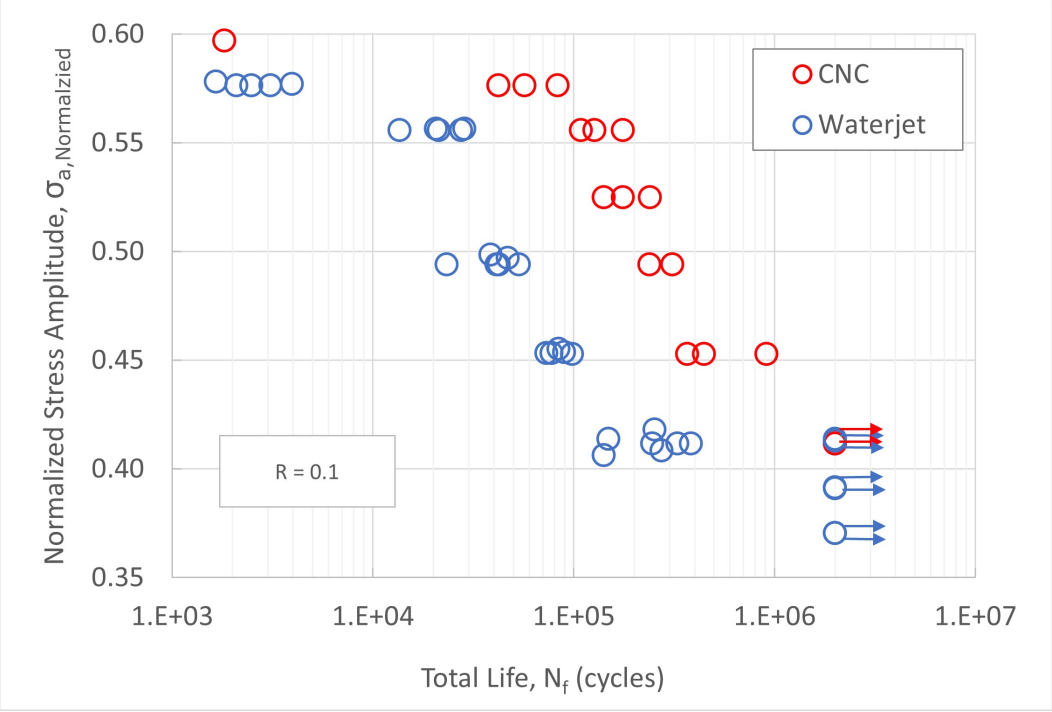

(a)

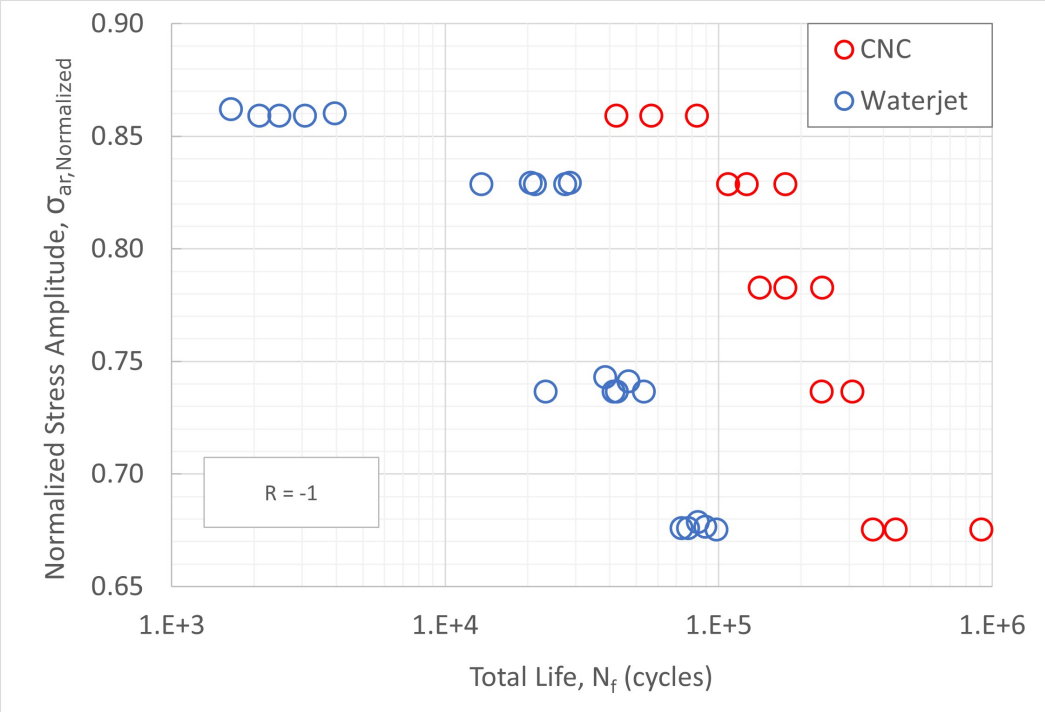

(b)

Figure 9.4: Comparison of the stress-life curves at (a)R=0.1 (b) R=-1

Table 9.3: Comparison of the Normalized Fatigue Parameters from Water-jet cutting and CNC machining method

Fatigue Parameters	Water-jet	CNC
$\sigma'_{f,Normalized}$	2.09	3.62
b	-0.094	-0.120

9.2 Chapter Conclusion

This chapter investigated the effect of mean stress and cutting methods on the fatigue life of non-oriented electrical steel sheets. The following conclusions can be drawn.

- The tests suggest an effect of mean stress on the fatigue life.
- The mean stress decreases the stress amplitude at which infinite life will be obtained.
- Water-jet cutting method produces specimens with significantly rougher edges than CNC machining which significantly reduces the fatigue life of the specimens.

Chapter 10

Conclusions, Contributions and Future Work

10.1 Thesis Conclusion

This thesis investigated three grades of thin non-oriented electrical steel sheets with the aim of characterizing the material and mechanical properties. Chapter 4 investigated the material properties of non-oriented electrical steel sheets while Chapters 5 and 6 investigated the tensile properties of non-oriented electrical steel sheets room temperature and an elevated temperature of 150°C respectively. Parameters to model the tensile behaviour of the sheets as well as the effects of sheet thickness and temperature on the tensile properties were also presented in both chapters. The chapters then ended with an examination of the fractured surfaces of the tensile specimens from which the deformation and fracture mechanisms under tensile loading were ascertained. Chapters 7 and 8 investigated the fatigue properties of non-oriented electrical steel sheets at room temperature and an elevated temperature of

150°C respectively. Parameters to model the fatigue behaviour of the sheets as well as the effects of sheet thickness and temperature on the fatigue properties were also explored in both chapters. The chapters then ended with an examination of the fractured surfaces of the fatigue specimens from which the deformation and fracture mechanisms under cyclic loading were ascertained. Finally, in chapter 9, the effects of mean stress and cutting method on the fatigue life of non-oriented electrical steel sheets were discussed and presented. The conclusions of each investigation were included at the end of the relevant chapters and have been listed below for convenience.

Chapter 4

- The microstructure of these thin sheets are characterized by the distribution of few and relatively large grains on the same order of magnitude as the thickness across the sheet thickness.
- The crystal structure of the sheets is body centered cubic.
- The grains are randomly oriented and do not favour any particular direction in terms of its texture.
- Aluminium nitride precipitates are most likely present in the matrix of these steel sheets.

Chapter 5

- The tensile properties along the rolling and transverse directions were comparable for all three grades of non-oriented electrical steel sheets tested at room temperature.

- The 20SW1200 grade showed the most isotropy out of the three grades of non-oriented electrical steel sheets tested in terms of its tensile properties at room temperature.
- Sheet thickness does not seem to have an effect on the tensile properties of non-oriented electrical steel sheets at room temperature.
- Although the fractured specimens had no visible signs of necking, it was observed locally along the fracture surface.
- The general fracture mode was a mix between intergranular type fracture in the ductile deformation region and transgranular type fracture in the sudden failure region.

Chapter 6

- The three grades of non-oriented electrical steel sheets each had similar tensile properties at an elevated temperature of 150°C along the rolling and transverse directions.
- The 20SW1200 remained the most isotropic in terms of its tensile properties out of all three grades of non-oriented electrical steel sheets tested.
- Sheet thickness does not affect the tensile properties at an elevated temperature of 150°C.
- The fracture surface of the 27PNX1350F specimens were similar to their counterparts at room temperature which displayed significant local necking evidenced by a thinning of the specimens around the fracture region.
- The general effect of temperature on the tensile properties of non-oriented electrical steel sheets was a reduction in the yield strength as well as the deformation capacity

of the sheets.

Chapter 7

- The S-N curves were linear within the range of fatigue lives tested.
- The sheet thickness does not have an effect on the fatigue life of the non-oriented electrical steel sheets.
- The general fracture mode is a mixed mode of cyclic deformation and transgranular cleavage fracture.

Chapter 8

- Increasing the temperature causes a noticeable but slight reduction in the fatigue life at 150°C.
- The fracture surface at 150°C was characterized by a mixture of transgranular crack propagation and final ductile cone-like fracture.

Chapter 9

- The tests suggest an effect of mean stress on the fatigue life.
- The mean stress decreases the stress amplitude at which infinite life will be obtained.
- Water-jet cutting produces specimens with significantly rougher edges than CNC machining which significantly reduces the fatigue life of the specimens.

10.2 Contributions and Recommended Future Work

The research presented in this thesis has contributed the following the the current body of knowledge.

- A verification of the microstructural properties of non-oriented electrical steel sheets.
- A catalog of the tensile and fatigue properties of thin non-oriented electrical steel sheets at room and an elevated temperature of 150°C.
- An in-depth look into the effect of sheet thickness and temperature on the tensile and fatigue properties of non-oriented electrical steel sheets.
- Tensile and fatigue parameters that can be used in computer aided engineering software to model the material behaviour of non-oriented electrical steel sheets at room and elevated temperatures.
- The deformation and fracture mechanisms of non-oriented electrical steel sheets under tensile and cyclic loading at room temperature and an elevated temperature of 150°C.
- An investigation on the effect of mean stress and cutting method on the fatigue properties of non-oriented electrical steel sheets.

Based on the research presented in this thesis, the recommended direction for future work includes:

- A confirmation of the tensile and fatigue model parameters presented using computer aided engineering software and experiments.
- A more detailed look into the effect of mean stress of the fatigue life

- Multi-axial tensile and cyclic testing of thin electrical steel sheets.
- Modeling the tensile and fatigue material behaviour of thin electrical steel sheets under complex stress states.
- An in-depth look into the effect of other precipitates on the mechanical properties of thin non-oriented electrical steel sheets.

Bibliography

[1] P. Research, "Electric vehicle market," Precedence Research, Apt 1408 1785 Riverside Drive Ottawa, ON, K1G 3T7, Canada, Tech. Rep. 1009, 2022.

[2] V. Lakkonavar, S. Kavi, P. Jones, M. Thompson, Y. S. Leong, and P. Crepeau, "Edge-quality effects on mechanical properties," SAE International, Tech. Rep., 2020.

[3] Y. Gao, R. Long, Y. Pang, and M. Lindenmo, "Fatigue properties of an electrical steel and design," *SAE International*, 2010.

[4] D. Petrovic, "Non–oriented electrical steel sheets," *Acta Materialia*, vol. 6, no. 44, pp. 317–325, 2010.

[5] V. Rohal, E. Spisak, P. Mulidran, and J. Majernikova, "Basic classification and processing of electrical steels," *The International Journal of Engineering and Science*, vol. 9, no. 7, pp. 1–2, 2020.

[6] *Electrical Steel: Manufacturing Process*, 2021.

[7] Y. Donghyun and P. Hyunseok, "Developmental trajectories in electrical steel," *Sustainability*, vol. 10, no. 8, 2018.

[8] C. Hongzhi, H. Linpo, Y. Jingwen, Z. Xianglin, L. Zhonghan, C. Shenglin, and L. Rongfengg, "The influence of punching process on residual stress and magnetic domain structure of non-oriented silicon steel," *Journal of Magnetism and Magnetic Materials*, vol. 406, pp. 42–47, 2016.

[9] W. Wei, C. Hongzhi, O. Hao, C. Zhichao, Z. Xianglin, L. Zhonghan, C. Shenlin, and L. Rongfeng, "Effects of punching process on crystal orientations, magnetic and mechanical properties in non-oriented silicon steel," *Journal of Magnetism and Magnetic Materials*, vol. 444, pp. 211–217, 2017.

[10] *How do I classify the temperature limits of an Electric Motor?*, Quantum Controls, 2022.

[11] STMicroelectronics, "Fundamentals of motor control," Geneva, Switzerland, 2020.

[12] E. Moyer, "Basics on electric motors," University of Chicago, April 2010.

[13] A. Honda, K. Senda, and K. Sadahiro, "Electrical steel for motors of electric and hybrid vehicles," Kawasaki Steel, Tech. Rep. 48, March 2003.

[14] S. Mathew, "How does an induction motor work ?"

[15] "Three phase induction motors – construction," 2021.

[16] H. Lamtec, "Electrical steel laminations."

[17] T. Ros-Yañez, Y. Houbaert, O. Fischer, and J. Schneider, "Production of high silicon steel for electrical applications by thermomechanical processing," *Journal of Materials Processing Technology*, vol. 141, no. 1, pp. 132–137, October 2003.

[18] S. K. Sarna, "Electrical steels," https://www.ispatguru.com/electrical-steels/, April 2013.

[19] B.Bode, A.Brueckner-Foit, and FD.Zeismann, "Quasi-static and cyclic behaviour of electrical sheet material," *International Journal of Fatigue*, vol. 82, no. 2, pp. 350–360, 2016.

[20] P.Janssen, T.D.Keijser, and M.Geers, "An experimental assessment of the grain size effects in the uniaxial straining of thin al sheet with few grains across the thickness," *Materials and Science Engineering*, vol. 419, no. 1-2, pp. 238–248, 2006.

[21] N. Hansen, "Hall–petch relation and boundary strengthening," *Scripta Materialia*, vol. 51, no. 8, pp. 801–806, 2004.

[22] J.J.W.Morris, "The influence of grain size on the mechanical properties of steel," *Office of Scientific and Technical Information*, 2001.

[23] T. Massalski, H. Okamoto, P. Subramanian, and L. Kacprzak, *Binary Alloy Phase Diagrams*, 2nd ed. Ohio: ASM International, 1990, vol. 3.

[24] M. Henning and H. Vehoff, "Local mechanical behavior and slip band formation within grains," *Acta Materialia*, vol. 53, pp. 1285–1292, 2005.

[25] T. Saeed, H. Youliang, S. Mehdi, P. Hadi, K. Winfried, R. Fiona, M. Mohsen, and K. Leo, "Mechanical properties and crystallographic texture of non-oriented electrical steel processed by repetitive bending under tensions," *Materials Science & Engineering A*, vol. 835, 2022.

[26] L. Hsin-Yi, H. I-Ching, and T. Ming-Chin, "Texture improvement of 3% si non-oriented electrical steel," *China Steel Technical Report*, vol. 28, 2015.

[27] Y. Wang, X. Zhang, H. Zhen, G. Zu, G. F. Ji, J. Duan, and R. Misra, "Effect of copper precipitates on mechanical and magnetic properties of cu," *Materials Science & Engineering A*, vol. 703, pp. 340–347, 2017.

[28] M. Schulte, S. Steentjes, N. Leuning, W. Bleck, and K. Hameyer, "Effect of manganese in high silicon alloyed non-oriented electrical steel," *Journal of Magnetism and Magnetic Materials*, vol. 477, pp. 372–381, 2019.

[29] N. E. Dowling, *Mechanical Behaviour of Materials*, 4th ed. Pearson Education Limited, 2012.

[30] S. B. Behravesh, H. Jahed, and S. Lambert, "Characterization of magnesium spot welds under tensile and cyclic loadings," *Materials and Design*, vol. 32, pp. 4890–4900, 2011.

[31] "What is tensile testing?" TWI Limited, 2022.

[32] "Tensile testing 101," MTS Systems, April 2021.

[33] *ASTM E8 / E8M-21, Standard Test Methods for Tension Testing of Metallic Materials*, 2021.

[34] A. Pahlevanpour, S. Karparvarfard, S. Shaha, S. Behravesh, S. Adibnazari, and H. Jahed, "Anisotropy in the quasi-static and cyclic behavior of zk60 extrusion: Characterization and fatigue modeling," *Materials and Design*, vol. 160, pp. 936–948, 2018.

[35] A. A.Roostaei and H. Jahed, "A cyclic small-strain plasticity model for wrought mg alloys under multiaxial loading: Numerical implementation and validation," *International Journal of Mechanical Sciences*, vol. 145, pp. 318–329, 2018.

[36] A. Yazdanmehr, A. A. Roostaei, and H. Jahed, "A novel test design for large strain uniaxial reverse loading of az31b sheet out of the rolling plane," *Journal of Engineering Materials and Technology*, vol. 143, no. 4, 2021.

[37] Wizard191, "Tensile specimen nomenclature," September 2010, based on an image from Tensile testing by Joseph R. Davis, p. 50.

[38] ADMET, "Tension testing / tensile testing."

[39] J. R. Davis, *Tensile Testing*, 2nd ed. ASM International, 2004.

[40] Zap-Science, "The engineering stress-strain curve (fully explained)," 2022.

[41] H. Makvana, "What is 0.20% proof stress?" 2017.

[42] P. S. Patwardhan, R. A. Nalavde, and D. Kujawski, "An estimation of ramberg-osgood constants for materials with and without luder's strain using yield and ultimate strengths," in *Procedia Structural Integrity*, ser. ICSI 2019, vol. 17, no. 2019. 1903 W Michigan Av., Kalamazoo, MI, 49008-4353, USA: Elsevier, 2019, pp. 750–757.

[43] A. W. Bowen and P. G. Partridge, "Limitations of the hollomon strain-hardening equation," *Journal of Physics D: Applied Physics*, vol. 7, no. 7, p. 969, March 1973.

[44] Intertek, "Fatigue testing," 2022.

[45] "Mechanical and durability testing of aerospace materials," in *Introduction to Aerospace Materials*, A. P. Mouritz, Ed. Woodhead Publishing, 2012, ch. 5, pp. 91–127.

[46] R. I. Stephens, A. Fatemi, R. R. Stephens, and H. O. Fuchs, *Metal Fatigue in Engineering*, 2nd ed. John Wiley and Sons Inc, 2001.

[47] S. A. McKelvey, Y.-L. Lee, and M. E. Barkey, "Stress-based uniaxial fatigue analysis using methods described in fkm-guideline," *Journal of Failure Analysis and Prevention*, vol. 12, p. 445–484, 2012.

[48] *Stress Life vs. Strain Life*, 67th ed., Materion Brush Inc., July 2014, technical Tidbits.

[49] H. Boyer, "Fatigue testing," ASM International, Tech. Rep., 1986.

[50] C. M. Stewart, "Stress-life approach," 2021.

[51] H. Jahed, A. Varvani-Farahani, M. Noban, and I. Khalaji, "An energy-based fatigue life assessment model for various metallic materials under proportional and non-proportional loading conditions," *International Journal of Fatigue*, vol. 29, no. 4, pp. 647–655, 2021.

[52] A. A. Roostaei, A. Pahlevanpour, S. B. Behravesh, and H. Jahed, "On the definition of elastic strain energy density in fatigue modelling," *International Journal of Fatigue*, vol. 121, pp. 237–242, 2019.

[53] A. Ince and G. Glinka, "A modification of morrow and smith–watson–topper mean stress correction models," *Fatigue & Fracture of Engineering Materials & Structures*, vol. 34, no. 11, pp. 854–867, 2011.

[54] *ASTM E466-15, Standard Practice for Conducting Force Controlled Constant Amplitude Axial Fatigue Tests of Metallic Materials*, 2015.

[55] A. Gryguć, B. Behravesh, S. Shaha, Jahed, M. Wells, B. Williams, and X. Su, "Multiaxial cyclic behaviour of extruded and forged az80 mg alloy," *International Journal of Fatigue*, vol. 127, pp. 324–337, 2019.

[56] H. Jahed and A. A. Roostaei, *Cyclic Plasticity of Metals*, ser. Plasticity of Metals. Elsevier, 2022.

[57] M. Noban, H. Jahed, S. Winkler, and A. Ince, "Fatigue characterization and modeling of 30crnimo8hh under multiaxial loading," *International Journal of Fatigue*, vol. 528, pp. 2484–2494, 2011.

[58] *ASTM E606-04, Standard Practice for Strain-Controlled Fatigue Testing*, 2012.

[59] J. Albinmousa and H. Jahed, "Multiaxial effects on lcf behaviour and fatigue failure of az31b magnesium extrusion," *International Journal of Fatigue*, vol. 67, pp. 103–116, 2014.

[60] J. Albinmousa, H. Jahed, and S. Lambert, "Cyclic axial and cyclic torsional behaviour of extruded az31b magnesium alloy," *International Journal of Fatigue*, vol. 33, pp. 1402–1416, 2011.

[61] ——, "Cyclic behaviour of wrought magnesium alloy under multiaxial load," *International Journal of Fatigue*, vol. 33, pp. 1127–1139, 2011.

[62] H. Jahed and J. Albinmousa, "Multiaxial behaviour of wrought magnesium alloys – a review and suitability of energy-based fatigue life model," *Theoretical and Applied Fracture Mechanics*, vol. 73, pp. 97–108, 2014.

[63] M. Noban, H. Jahed, and A. Varvani-Farahani, "The choice of cyclic plasticity models in fatigue life assessment of 304 and 1045 steel alloys based on the critical plane-energy fatigue damage approach," *International Journal of Fatigue*, vol. 43, pp. 217–225, 2012.

[64] H. Jahed and A. Varvani-Farahani, "Upper and lower fatigue life limits model using energy-based fatigue properties," *International Journal of Fatigue*, vol. 28, pp. 467–473, 2006.

[65] G. Fortese, G. Nicoletto1, and E. Riva, "Fatigue behaviour of thin fe-si steel sheets for electric motor production," ser. IOP Conf. Series: Materials Science and Engineering, vol. 1038, no. 1. IOP Publishing, 2004.

[66] D. Liying, Z. Guifeng, L. Jing, S. Wenmin, B-Yunjie, C. Zhaoyang, and X. Huan, "Fatigue cracking characterization of high grade non-oriented electrical steels," *Journal of Wuhan University of Technology-Mater. Sci. Ed*, vol. 32, no. 6, pp. 1329–1333, 2017.

[67] *ASTM E112-13, Standard Test Methods for Determining Average Grain Size*, 2021.

[68] *Environmental Chambers*, INSTRON, 825 University Ave Norwood, MA, 02062-2643, US.

[69] C. Shen, P. Wirsching, and G. Cashman, "Design curve to characterize fatigue strength," *J Eng Mater Technol ASME*, vol. 118, no. 4, pp. 535–541, October 1996.

[70] L. Zhiqiang, H.-Z. Huang, H.-K. Wang, H. Gao, and F.-J. Zuo, "Determining the walker exponent and developing a modified smith watson topper parameter model," *Journal of Mechanical Science and Technology*, vol. 30, no. 3, pp. 1129–1137, 2016.

[71] G. Gill, B. Behravesh, D. Saha, Y.-H. Chen, M. Mills, W. Zhang, G. Lamonaca, and H. Jahed, "Effect of edge finish on fatigue behaviour of thin non-oriented electrical steel sheets," ser. WCX 2023, Fatigue and Stress Analysis Laboratory (FATSLab) and Stellantis. Society of Automotive Engineers (SAE), 2023.